FRICTIONAL EXCHANGE FLOW THROUGH A WIDE CHANNEL WITH APPLICATION TO THE BURLINGTON SHIP CANAL

by

LI GU

B.Eng.	Hohai University, China	1984
M.Eng.	Hohai University, China	1989
M.A.Sc.	University of British Columbia	1993

A THESIS SUBMITTED IN PARTIAL FULFILLMENT OF

THE REQUIREMENTS FOR THE DEGREE OF

DOCTOR OF PHILOSOPHY

in

THE FACULTY OF GRADUATE STUDIES

DEPARTMENT OF CIVIL ENGINEERING

We accept this thesis as conforming

to the required standard

THE UNIVERSITY OF BRITISH COLUMBIA

MAY, 2001

In presenting this thesis in partial fulfilment of the requirements for an advanced degree at the University of British Columbia, I agree that the Library shall make it freely available for reference and study. I further agree that permission for extensive copying of this thesis for scholarly purposes may be granted by the head of my department or by his or her representatives. It is understood that copying or publication of this thesis for financial gain shall not be allowed without my written permission.

Department of Civil Engineering

The University of British Columbia
Vancouver, Canada

Date April 26, 2001

DE-6 (2/88)

ABSTRACT

The maximal frictional two-layer exchange flows in general and the exchange of water through the Burlington Ship Canal in particular were studied through both theoretical analysis and laboratory experiments. Gravitational two-way exchange flows are often driven by a slight density difference due to temperature, salinity and/or sediment concentration variations across a constriction connecting two water bodies. The exchange of two fluids of differing density through the constriction such as a channel or strait is of importance in a wide range of geophysical, oceanographic, and engineering contexts. One such example, which has largely motivated this study, is the exchange of water through the Burlington Ship Canal connecting the heavily polluted Hamilton Harbour with Lake Ontario.

Previously analytical solutions to exchange flow problems have often ignored frictional and/or non-linear inertial effects. As a result, the applicability of such solutions is fairly limited, especially for the Burlington Ship Canal, where both frictional and inertial effects are important. To this end, the fully non-linear one-dimensional shallow-water equation must be used to describe general frictional exchange flow problems. So far, solutions to such problems have been exclusively obtained through numerical integration.

The maximal, steady, frictional exchange flow through a horizontal channel of constant width was studied analytically in the context of two-layer internal hydraulics. The fully non-linear hydraulic or shallow water equation for a two-layered flow system was solved through direct integration as a Boundary Value Problem (BVP). The resulting analytical exchange flow solutions predict the maximal exchange flow rate and interface profile throughout the channel for given frictional parameters.

A laboratory facility was also designed specifically for the purpose of modelling the two-layer exchange flow. The laboratory experiments aim to validate the theoretical predictions

and provide additional in-depth understanding of the dynamics of exchange flows. The exchange flows established in the laboratory experiments were studied using conductivity profiling, flow visualization, particle image velocimetry, and image processing techniques.

The solution shows that friction significantly increases the overall interface slope and reduces the exchange rate. Despite the pronounced non-linear nature of exchange flow problems, the linear density interface profile has been widely used as the first approximation in the previous theoretical formulations of analytical solutions on frictional exchange flows. The linear density interface profile assumes that the density interface follows a straight line linking two hydraulic controls. The resulting non-linear exchange flow solution indicates that the interface profile is not only non-linear, but also non-symmetric in nature. The theoretical predictions compared well with both laboratory experiments and field measurements in the Burlington Ship Canal as well as several famous sea straits.

TABLE OF CONTENTS

ABSTRACT ii

TABLE OF CONTENTS iv

LIST OF TABLES vii

LIST OF FIGURES viii

LIST OF SYMBOLS xiii

ACKNOWLEDGEMENTS xvii

CHAPTER 1 INTRODUCTION 1

1.1 General 1

1.2 Hamilton Harbour and Burlington Ship Canal 1

1.3 Scope and Objectives 4

1.4 Thesis Outline 6

CHAPTER 2 LITERATURE REVIEW 9

2.1 General 9

2.2 Frictional Two-layer Exchange Flows 12

2.3 Exchange Flow in the Burlington Ship Canal 15

2.4 Interfacial Friction 17

CHAPTER 3 THEORETICAL FORMULATION 22

3.1 Basic Assumptions and Flow Configuration 22

3.2 Governing Equations 23

3.3 Propagation of Information and Hydraulic Control 27

3.4 Analytical Properties of Critical Flow and Maximal Exchange 32

3.5 Analytical Solutions to Maximal Two-layer Exchange Flows 37

3.5.1 Maximal Exchange Flow Through a Wide Channel 39

3.5.2 Maximal Exchange Flow Through a Wide Culvert 45

3.5.3 Presentation of Maximal Exchange Flow Solutions on the $G_o^2 - \eta$ Plane 47

CHAPTER 4 EXPERIMENTAL APPARATUS AND TECHNIQUES 53

4.1 Laboratory Experiment Set-up 53

4.2 Laboratory Measurement Technique 55

4.2.1 Conductivity Probe and Density Profiling 55

4.2.2 Image Analysis and Density Interface Positions 57

4.2.3 Particle Image Velocimetry (PIV) 58

4.2.4 Acoustic Dopller Velocimeter (ADV) 59

4.3 Laboratory Experiment Procedure 59

4.4 Error Analysis 62

4.5 Field Experiment 63

CHAPTER 5 RESULTS AND DISCUSSION 65

5.1 Laboratory Experiment 65

5.1.1 Laboratory Measurements 66

5.1.2 Estimation of Interfacial Friction 70

5.1.3 Comparison with Laboratory Experimental Data 71

5.2 Comparison with Field Data 76

5.3 Discussion 81

5.3.1 The Analytical Solution versus the Numerical Integration 81

5.3.2 Non-linear Effects and the Shape of the Density Interface 82

5.3.3 Effects of Friction on Exchange Rates 83

5.3.4 Relative Importance of Interfacial and Bottom Friction 85

5.3.5 Effects of Moderate Barotropic Forcing 86

CHAPTER 6 CONCLUSIONS AND RECOMMENDATIONS 90

APPENDIX A GENERAL SOLUTIONS FOR MAXIMAL TWO-LAYER EXCHANGE FLOWS 93

A.1 Maximal Exchange Flow Through a Wide Channel 93

A.2 Maximal Exchange Flow Through a Wide Culvert 96

APPENDIX B NUMERICAL PROCEDURES 99

BIBLIOGRAPHY 102

FIGURES 109

LIST OF TABLES

Table		Page
2-1	Values of α for various sea straits.	10
4-1	Conductivity of KCl at 25.0°C (Adapted from Table 2510:I of Standard Method, 1992).	61
5-1	List of densimetric exchange flow experiments.	66
5-2	Comparison with field data in the Burlington Ship Canal.	77
5-3	Comparison with field data in several famous sea straits.	79

LIST OF FIGURES

Figure		Page
1-1	Plan view of Hamilton Harbour, Burlington Ship Canal and Lake Ontario (Adapted from Figure 1 of Hamblin & Lawrence, 1990).	109
1-2	(a) Burlington Ship Canal looking towards Lake Ontario, (b) Hamilton Harbour basin.	110
1-3	Schematic of the two-layer densimetric exchange flow through the Burlington Ship Canal during the summer (Redrawn from Figure 2 of Hamblin & Lawrence, 1990).	111
2-1	Notation sketch for a two-layer exchange flow system.	112
2-2	Depth of the interface as a function of position along the strait. The upper curves are for the largest S values, where S is the salinity ratio of two exchanging water bodies and N is upper layer area fraction of the total cross section area (Adapted from Figure 2 of Assaf & Hecht, 1974).	113
2-3	Measurements in the long strait experiments of Anati, *et al.* (1974). (a) Temperature profiles at 11 stations along the length of the strait. Arrows denote the height of zero velocity. (b) A longitudinal temperature section along the strait. The heavy dashed line, with slope $\beta = 0.615$, is the solution of (2-2). (c) The measured composite Froude number at 11 stations along the length of the strait (Adapted from Figure 10 of Anati, et al., 1977).	114
2-4	Computed Lake Ontario inflow, Q_2 (m^3/s), based on extreme density difference from the data of Spigel (1989), versus observed inflow (Adapted from Figure 3 of Hamblin & Lawrence, 1990).	115
2-5	Temperature contours for the Hamlilton Harbour on August 3, 1988, indicating overturning event at station *AM*1 (Adapted from Spigel, 1988).	116
3-1	Plan (a) and side (b) views of the flow configuration for the maximum two-layer exchange flows. U_i, y_i and ρ_i are the average velocity, depth, and density of each layer respectively. L, H and b are channel length, depth and width respectively. Subscripts $i = 1, 2$ denote upper and lower layers respectively.	117

Figure		Page
3-2	Definition sketch of the shear stresses acting on a control volume of a two-layer flow system, where τ_s, τ_w, τ_b and τ_I are surface, wall, bottom, and interfacial shear stresses respectively.	118
3-3	Definition diagram for velocity and density structures of a two-layer flow system separated by a vortex sheet at $y=0$.	119
3-4	Characteristic curves on the $x-t$ plane, where u_c and c are convective velocity and phase speed of two-layer flows respectively, C_+ and C_- are positive and negative characteristics respectively.	119
3-5	(a) $E-y_2$ curves for given exchange flow rate q. (b) $q-y_2$ curves for given internal energy E. Points a and b represent locations at left and right ends of the channel for maximal exchange flows.	120
3-6	Analytical solutions for densimetric two-layer exchange flows through a wide channel. (a) Presentation of solutions on the $G_o^2-\eta$ plane, where thinner lines are solution curves of varying frictional parameter α ($f_r=1$), and thicker line represents the critical boundary condition at each end of the channel. (b) Variation of density interface along the channel, where points a and b correspond to locations shown in (a). (c) Variations of the composite Froude number G^2 and the internal Froude number F_I along the channel. (d) Variations of the friction slope S_f and the internal energy E along the channel.	122
3-7	Schematic showing the iteration procedure used to solve the maximal two-layer exchange flows as a boundary value problem, where $G_o^{2(i)}$ and $\eta_1^{(i)}$ are intermediate iteration values of G_o^2 and η_1 at the ith iteration respectively.	123
3-8	Maximal two-layer exchange flow solutions represented on the $E-\eta$ plane (a) and on the Froude-number plane (b). Points a and b correspond to locations shown in Figure 3-6b. Point c represents the solution for $\alpha=0$.	124
4-1	Overview of laboratory experiment set-up. All dimensions shown are in millimetres.	125
4-2	Laser optical set-up showing the laser generator as well as scanner and reflecting mirrors.	126

Figure		Page
4-3	The relationship between density as $\sigma_t = \rho - 1000$ and conductivity for NaCl salt solutions used in the experiment at four different sampling temperatures. The symbols are direct calibration points and the solid lines are linear regression curves.	127
4-4	Automated traversing mechanism and conductivity probe.	128
4-5	Schematic diagram of particle image velocimetry technique. Two images are captured at Δt apart. The velocity is calculated at each node by search a widow with maximum cross correlation (Adopted from Figure 1 of Stevens & Coates, 1994).	129
4-6	Laser induced florescence image showing two-way maximal exchange flow	129
4-7	Location and set-up of moored instrumentation for summer 1996 field experiment. (a) Side view of the ship canal. (b) Plan view of the Hamilton Harbour, the Burlington Ship Canal, and Lake Ontario (Adopted from Figure 3.1 of Tedford, 1999).	130
5-1	Measured velocity and density profiles for E5 at $x = 0.5L$. (a) Velocity profile measured by PIV technique and ADV probe. (b) Density profile measured by a traversing conductivity probe.	131
5-2	Definition diagram for three different interfaces of exchange flows, where δ and ς are the shear layer thickness and the density interface thickness respectively.	132
5-3	Comparison of the theoretical predictions with laboratory experiment E5. (a) Density interface profile along the channel. (b) The variation of composite Froude number, G^2, along the channel. (c) The variation of internal energy, E/H, along the channel. Solid lines are theoretical predictions based on analytical exchange flow solutions. The symbols with error bars represent laboratory measurements.	134
5-4	Comparison on exchange flow rates between laboratory measurements (q_m) and theoretical predictions (q_p) for eight experimental runs (E1 – E8). The solid triangles and the circles are the predictions of frictional analytical solution and inviscid exchange flow theory respectively. The two dotted lines represent $\pm 5\%$ error from the perfect match. The bottom friction factor f_b ranges from	135

Figure		Page
	0.007 to 0.013, and the interfacial friction factor f_i ranges from 0.0031 to 0.0041.	
5-5	Comparisons of field measurements of exchange flow rates through the Burlington Ship Canal (q_m) with theoretical predictions (q_p). The solid triangles, the circles, and diamonds represent predictions based on the analytical exchange flow solution, the linear exchange flow theory and the inviscid exchange flow theory respectively. The bottom friction factor $f_b = 0.0026$ and the interfacial friction factor $f_i = 0.001$.	136
5-6	Comparison of field measurements of exchange flow rates through several famous sea straits (q_m) with theoretical predictions (q_p). The solid triangles and the circles are predictions of the frictional analytical solution and the linear exchange flow theory respectively. The bottom friction factor $f_b = 0.012$, except for the Bosphorus Strait where $f_b = 0.0046$. The interfacial friction factor $f_i = 0.0024$ for all the straits.	137
5-7	Comparison of computational schemes used for calculation of longitudinal density interface profiles. (a) Numerical integration or step method. (b) Direct integration method. Points *1*, *2*, *3*, and *4* represent order of computational procedure.	138
5-8	Normalized interface shapes for two-layer exchange flows with varying frictional ratio f_r. The frictional parameter α is constant at unity.	139
5-9	Effects of friction on the exchange flow rates. The solid lines represent the analytical frictional exchange flow solutions developed in this study. The doted line represents the linear exchange flow solutions of Anati, *et al.* (1977). The friction ratio of f_r ranges from 0.7 to 1.0 for laboratory experiments and from 0.2 to 0.4 for field data respectively.	140
5-10	The measured velocity and density profiles for E9 at $x = 0.5L$. (a) Velocity profile measured using PIV technique, and (b) density profile measured by a traversing conductivity probe.	141

Figure		Page
5-11	Schematics of internal flow structure of a two-layer exchange flow with a barotropic flow component.	141

LIST OF SYMBOLS

Roman

a_o	constant of integration
$A = bH$	channel cross section area
$A_i = by_i$	cross section area of layer i
b	width of the channel
C_1, C_2	constants
C_+, C_-	positive and negative characteristics
c	phase speed of interfacial long wave of two-layer flows
c_I	phase speed of interfacial long wave of shear-free two-layer flows
$d = y_{21} - y_{20}$	total interface displacement
E	internal energy head
$E^* = E/H$	non-dimensional internal energy head
E_i	unit mechanical energy of layer i
$F_r^2 = U^2/gH$	non-densimetric Froude number
$F_i^2 = U_i^2/g'y_i$	densimetric Froude number of layer i
$F_I^2 = u_c^2/c_I^2$	internal Froude number
$F_\Delta^2 = \Delta U^2/g'H$	stability Froude number
f_0, f_1	solution curves at $x/L = 0,\ 1$ respectively
f_b	bottom friction coefficient
f_{b_e}	effective bottom friction coefficient
f_I	interfacial friction coefficient
f_{I_e}	effective interfacial friction coefficient
$f_r = f_I/f_b$	frictional coefficient ratio
f_s	surface friction coefficient
f_w	sidewall friction coefficient
$G^2 = F_1^2 + F_2^2$	composite internal Froude number
$G_o^2 = 16q^2/(g'H^3)$	composite Froude number in the absence of friction
g	gravitational acceleration
$g' = g(\rho_2 - \rho_1)/\rho_2$	reduced gravitational acceleration

$H = y_1 + y_2$	total depth of the channel
$K = \mathrm{Re}\, F_\Delta^2 = \Delta U^3 / \nu g'$	Keulegan number
k	wave number
L	length of the channel
P	pressure
$q = Q/b$	unit flow rate
$q_i = Q_i/b$	unit flow rate for layer i
$q_m = Q_m/b$	measured unit flow rate
$q_p = Q_p/b$	predicted unit flow rate
$q_b = Q_b/b$	unit barotropic flow rate
$q_b^* = q_b/\sqrt{g'H^3}$	non-dimensional unit barotropic flow rate
Q	volumetric flow rate
Q_b	volumetric barotropic flow rate
Q_i	volumetric flow rate of layer i
$r = \rho_1/\rho_2$	density ratio
R	exchange flow strength parameter
R_h	hydraulic radius
$\mathrm{Re} = \Delta U H/\nu$	channel Reynolds number
$\mathrm{Re}_\delta = \Delta U \delta/\nu$	shear Reynolds number
$S_f = S_{fI} + S_{fb}$	frictional slope
S_{fb}	bottom frictional slope
S_{fI}	interfacial frictional slope
S_0	topographic slope
$S_r = S_{fI}/S_{fb}$	frictional slope ratio
t	time
T	forcing period
u	horizontal velocity
u_c	internal convective velocity
$\overline{U}$	mean velocity
$U_i = q_i/y_i$	horizontal mean velocity for layer i
$U_i^* = U_i/\sqrt{g'H}$	non-dimensional horizontal mean velocity for layer i
$\Delta U = \lvert U_1 - U_2 \rvert$	horizontal mean velocity difference between the two layers

v	vertical velocity
x	horizontal coordination
y	vertical coordination
y_i	thickness or depth of layer i
$y_i^* = y_i/H$	non-dimensional thickness or depth of layer i
y_{ij}	thickness or depth of layer i at $x = j$

Subscripts and Superscripts

b	subscript denoting bottom frictional parameter
i ($i = 1,2$)	subscript denoting parameter for layer i; the upper and lower layers are denoted by $i = 1$, $i = 2$, respectively
I	subscript denoting interfacial frictional parameter
j ($j = 0,1$)	subscript denoting parameter at either end of the channel; the left and right ends of the channel are denoted by $j = 0$, $j = 1$, respectively
w	subscript denoting wall frictional parameter
s	subscript denoting surface frictional parameter
$'$	superscript denoting differentiation, except for g'
$*$	superscript denoting non-dimensional parameter

Greek

$\alpha = f_b L/H$	frictional parameter
$\beta = d/H$	non-dimensional total interface displacement
$\chi = x/L$	non-dimensional horizontal coordination
$\varepsilon = \Delta\rho/\rho_2$	relative density difference
$\delta = \Delta U/(\partial u/\partial y)_{\max}$	shear layer thickness
$\eta = y_2^* - \frac{1}{2} = \frac{1}{2} - y_1^*$	non-dimensional interfacial deflection from the mid-depth
$\gamma = T\sqrt{g'H}/L$	time parameter
κ_e	eddy diffusivity
λ	characteristic speed of internal wave

ν	viscosity
ν_e	eddy viscosity
σ	conductivity
$\sigma_t = \rho - 1000$	density unit in kg/m^3
$\varsigma = \Delta\rho/(\partial\rho/\partial y)_{\max}$	density interface thickness
θ	error tolerance of iteration process
ρ	density
$\overline{\rho} = (\rho_1 + \rho_2)/2$	mean density of two layers
ρ_i	density of layer *i*
$\Delta\rho = \rho_2 - \rho_1$	density difference
Θ	temperature
$\Theta_{\exp}$	temperature of experimental fluid
Θ_{ref}	reference temperature
Θ_{sample}	sample temperature
τ	shear stress
τ_b	bottom shear stress
τ_I	interfacial shear stress
τ_s	free surface shear stress
τ_w	wall shear stress

ACKNOWLEDGEMENTS

I would like to thank my supervisor Professor Greg Lawrence for his motivation and guidance throughout this thesis. Also I would like to thank the other members of my supervisory committee for their helpful suggestions in the preparation of this documentation.

I had fruitful discussions with Dr. Craig Stevens and Dr. Noboru Yonemitsu during the early stage of this research. Dr. Roger Pieters provided generous help throughout the course of the research. Dr. Zhu Zhiwei made valuable suggestions on laboratory technique and provided the image processing programs. Their invaluable support is deeply appreciated. Many thanks go to other members of the Environmental Fluid Mechanics group for their help in many ways. My appreciation also goes to Scott Jackson for his help in setting-up the laboratory apparatus, instrumentation, and data acquisition system.

Last, but not the least, a special thanks go to my wife Yiqing for her understanding and patience.

Financial support from the Natural Science and Engineering Research Council (NSERC) in the form of a Research Assistantship, which supported me throughout the majority of this work, is gratefully acknowledged.

CHAPTER 1
INTRODUCTION

1.1 GENERAL

A slight density difference due to temperature, salinity and/or sediment concentration variations across a constriction connecting two water bodies often drives a gravitational exchange flow. The exchange of two fluids of differing density through a constriction is of importance in a wide range of geophysical, oceanographic, and engineering contexts. A good understanding of exchange flow problems is crucial to understanding the water quality of many semi-enclosed water bodies such as harbours, bays, fjords and inlets, where the exchange with more open waters is restricted.

An exchange flow which has attracted considerable interest is the exchange through the Strait of Gibraltar, where less saline North Atlantic water flows in the surface and more saline Mediterranean water flows out at depth (Defant, 1961; Armi & Farmer, 1988). Some other examples of exchange flows include, for example, the exchange through the Bosphorus (Gregg & Ö zsoy, 2000), the exchange flow through the Great Belt connecting the Baltic with North Sea (Ottesen-Hansen & Moeller, 1990), the flushing of coastal marinas (Schwartz & Imberger, 1988), and the water exchange through the Great Salt Lake culvert (Holley & Waddell, 1976).

1.2 HAMILTON HARBOUR AND BURLINGTON SHIP CANAL

This study is motivated by exchange flow through the Burlington Ship Canal connecting the heavily polluted Hamilton Harbour with Lake Ontario (Hamblin & Lawrence, 1990). Hamilton harbour basin is an enclosed water body located at the western end of Lake Ontario.

It is roughly triangular in shape with a maximum east-west dimension of about 8 km and north-south dimension of about 4 km, as shown in Figure 1-1. The harbour has a surface area of about 21.5 km^2, a maximum depth of 22 m, and a mean depth of 13 m (Klapwijk & Snodgrass, 1985). The Burlington Ship canal is a 836 m long straight open channel connecting the Hamilton Harbour with Lake Ontario, as shown in Figure 1-2a. It has a simple rectangular geometry with a width of 89 m and an average depth of 9.6 m (Spigel, 1989).

The harbour catchment basin of about 500 km^2 contains the City of Hamilton and a large portion of the City of Burlington with a total population close to half a million. The watershed is composed of a complex combination of urban, industrial, and agricultural areas. The shores of Hamilton Harbour itself have one of Canada's major concentrations of heavy manufacturing industry, including two large steel mills as well as docking facilities (see Figure 1-2b). Heavy industries re-circulate their processing and cooling water from the harbour. The cities of Hamilton and Burlington draw water supplies from Lake Ontario and release all of their treated sewage into the harbour.

Due to heavy loading from sewerage treatment plants, industry, combined sewer overflows during storm events, and urban storm runoff, Hamilton Harbour suffers severe water quality problems (e.g. Polak & Haffner, 1978; Harries *et al*, 1980; and Gorrie, 1987). The International Joint Commission has designated the harbour basin as one of the 42 areas of environmental concern in the Great Lakes. A Remedial Action Plan for Hamilton Harbour finished in 1992 addresses some major environmental concerns, such as toxic and bacterial contamination, water quality, stresses in fish and wildlife, urbanization and land management, and access and aesthetics.

The physical process of particular importance to the harbour ecology is the flushing action due to the two-way exchange with Lake Ontario through the ship canal and the land-based

inflows. Unlike most lakes with in-flowing rivers whose discharges only depend on rainfall and subsequent runoff from the surrounding watershed, Hamilton Harbour receives its major inflow through the ship canal from Lake Ontario. The ship canal also serves as Hamilton Harbour's only natural outflow channel. Because Lake Ontario generally contains fewer pollutants than Hamilton Harbour, two-way exchange flow provides enhanced flushing of the harbour water. The flushing action is most significant during the summer season when stratification is the strongest (Klapwijk & Snodgrass, 1985).

The two-way exchange flow through the ship canal depends on water density/temperature and water level differences at either ends of the canal. The temperature differences are partly of natural origin and partly due to thermal discharges from local sewerage treatment plants and heavy industries. A significant portion of the Hamilton Harbour is less than 6 m deep as compared to the depth of over 30 m in the adjacent part of Lake Ontario. In any event, the water becomes much warmer in the harbour than in the lake, and temperature differences greater than $15^{o}C$ have been observed (Greco, 1998). The contrast in density between the two water bodies over the depth of the ship canal drives the densimetric exchange flow. The inflowing dense lake water sinks until its density matches that of the ambient water and then intrudes into the deep harbour water, and the surface waters of the harbour flow out through the ship canal and then spread as a thin surface jet of buoyant fluid into Lake Ontario, as shown schematically in Figure 1-3. The densimetric or mean exchange flow is often complicated by the fluctuation of barotropic forcing or differences of water level between Lake Ontario and Hamilton Harbour (Spigel, 1989; Tedford, 1999).

On average, there is always a weak net outflow from Hamilton Harbour to Lake Ontario because the harbour receives surface runoff from urban stormwater runoff and there are also abundant effluents from industry and municipalities, which draw their water supplies from the lake. The magnitudes of these land-based flows have been estimated on an annual average basis by some previous studies (e.g. Klapwijk & Snodgrass, 1985; Harris *et al.*,

1980). Klapwijk & Snodgrass (1985), for example, estimated an annual average flow from all land-based sources of 1.0×10^6 m^3/day. The total annual average flow out of the harbour, on the other hand, was estimated as 3.8×10^6 m^3/day. Therefore, the harbour-lake two-way exchange represents a significant portion of the total flushing volume in the harbour.

1.3 SCOPE AND OBJECTIVES

Essentially there are two distinct questions to be answered with regard to the role of the lake-harbour exchange in improving the water quality of the harbour. The first question concerns ways to quantify the exchange flow rate through the ship canal itself, and the second question concerns the fate of lake water after it enters the harbour. This study aims to further the understanding of the dynamics of the water exchange through the Burlington Ship Canal in particular and the densimetric exchange flow in general through both theoretical analysis and laboratory experiments. The answer to the second question would rely on the better understanding of mixing and circulation mechanisms within the harbour basin, which is beyond the scope of this study.

Many important features of exchange flows have been successfully accommodated by the hydraulic theory of two-layer frictionless or invicid flows (e.g. Armi and Farmer, 1986; Farmer & Armi, 1986). Frictional effects, however, can not be always ignored, except in those dynamically short channels where inertial forces are dominant comparing with frictional forces. Furthermore, much of the current knowledge on exchange processes in lakes stems from theories with an oceanographic context despite some special characteristics in lake exchange flows. One of the significant characters of lake exchange flows is their high non-linearity. This is mainly due to the confined geometry of connecting passage, where flow intensity tends to be much higher than other regions of lakes, as pointed out by Hamblin (1996). The concentration of flows results in intensified non-linear inertial effects. This

implies that simple linear frictional exchange flow theories, where the non-linear inertial terms are ignored, would be seldom applicable in lake exchange flows.

Anati *et al.* (1977) classified the length of the channel according to the ratio of bottom friction to inertial forces. The relative importance of frictional effects to inertial effects is indicated by a frictional parameter $\alpha = f_b L/H$, where f_b is the bottom frictional coefficient, H and L are the total fluid depth and length of the channel respectively. A channel is considered to be short if $\alpha << 1$, long if $\alpha >> 1$, and marginal if $\alpha \approx 1$. For the Burlington Ship Canal, frictional effects are equally important in comparison with inertial effects, and exchange flows must be described by the fully non-linear hydraulic equations with frictional effects included. Indeed, both bottom and interfacial frictional effects can not be ignored in the dynamics of exchange flows within the ship canal, as demonstrated by Hamblin & Lawrence (1990) who compared the predicted exchange rate to the field measurements of Spigel (1989).

Another special feature of lake exchange flows is its episodic nature or unsteadiness in barotropic forcing. Unlike ocean exchange flows which are usually dominated by the regular astronomical tides, lake exchange flows are also subject to intermittent water level fluctuations driven by lake seiches and meteorological front activities with time scale ranging from infragravity waves to meteorological disturbances up to several days (Freeman *et al*, 1974; Hamblin, 1996; and Tedford, 1999). The complexity of unsteady barotropic flows are usually studied by field experiments and numerical simulations on a site-specific basis.

This study is concerned with steady or quasi-steady two-layer frictional exchange flows. The exchange channel is assumed to be horizontal and of constant width with sudden expansions at both ends. In essence, this flow configuration isolates the most important features of frictional exchange flows and also closely resembles exchange flow conditions in the Burlington Ship Canal. The effect of Coriolis force is also ignored, therefore, the application

of the analysis is confined to channels that are much narrower than the internal Rossby radius of deformation.

The specific objectives of this study are to:

- Develop a more general analytical solution to two-layer densimetric exchange flow problems. To represent the fully non-linear nature of exchange flows, both frictional and inertial terms should be included in the theoretical formulation. The theoretical analysis aims to determine the gross behaviour or overall hydraulics of the two-layer exchange flow, rather than look into details and secondary effects.

- Conduct laboratory experiments on two-layer exchange flows. The laboratory experiments aim to validate the analytical exchange flow solutions and provide more in-depth understanding of the dynamics of exchange flows under manageable and repeatable flow conditions.

- Compare the developed analytical exchange flow solutions with both the laboratory measurements and existing field data. The field data includes those recently obtained from a comprehensive field investigation during the summer of 1996 as well as previous field flow measurements in the Burlington Ship Canal. Field flow data in several famous sea straits will also be compared with the theoretical predictions.

1.4 THESIS OUTLINE

Chapter 2 reviews some major relevant studies on exchange flows. Much of the previous work on exchange flows falls into two categories. First, description of exchange flows in terms of two-layer internal hydraulics, and secondly, the study of the interfacial friction due to interfacial entrainment and mixing processes. Although these two categories of studies are

inter-linked, the division will be retained in the literature review to a large extent simply for the reason of clarity. The nature of the lake exchange flows usually does not warrant the utilization of inviscid and/or linear assumptions used widely in oceanographic contexts. Consequently, the literature review will focus on frictional exchange flows in general and exchange flows in the Burlington Ship Canal in particular. A comprehensive review of interfacial friction indicates that there is still no commonly accepted theoretical basis, and as a result, discrepancies between predictions and data are large.

Chapter 3 sets out the framework and important assumptions for the theoretical analysis carried out in this study. The conventional two-layer hydraulic theory is extended to include frictional terms. This results in a fully non-linear one-dimensional shallow water equation, subject to hydraulic controls at both ends of the channel. The concepts of hydraulic control and maximal exchange are discussed in the context of propagation of infinitesimal long internal waves in two-layer shear flows. The fully non-linear one-dimensional shallow water equations formulated are then solved analytically as a boundary value problem. Given frictional parameters, the resulting analytical solutions predict the exchange flow rate as well as interface profile throughout the channel for maximal densimetric exchange flows.

Chapter 4 describes the laboratory apparatus and experimental set-up used in this study. It also describes the experimental techniques and procedures applied. During the laboratory experiments, information on velocity fields and interface positions were obtained using various flow visualization, particle tracking, and image processing techniques. The density profiles were measured using a conductivity probe. The field investigation during the summer of 1996 in the Burlington Ship Canal is also briefly described in this chapter.

Chapter 5 presents and discusses the results of theoretical and experimental work on two-layer densimetric frictional exchange flows. The analytical two-layer densimetric exchange flow solutions are compared with the laboratory measurements as well as field data in the Burlington Ship Canal and several famous sea straits. The theoretical solutions are also discussed in the context of other previous exchange flow theories.

Finally, Chapter 6 summarises various sections of this thesis, and draws some key conclusions from this study. Recommendations for future work are also made. The Appendixes A and B contain more detailed theoretical derivations and numerical procedures for the analytical exchange flow solutions presented in Chapter 3.

CHAPTER 2
LITERATURE REVIEW

2.1 GENERAL

Many stratified flows of geophysical, oceanographic, meteorological, and engineering importance can be modelled as two homogeneous layers of fluid with uniform horizontal velocities and negligible vertical velocities. As a consequence, the pressure distribution can be considered hydrostatic. The resulting equations of motion are refereed to as hydraulic or shallow water equations, which form the basis of internal hydraulic theory. The application hydraulic equations to two-layer flows was first applied by Stommel & Farmer (1953) and Schijf & Schonfeld (1953) in studying the exchange flow and salt water intrusion into estuaries and rivers.

The seminal study by Stommel & Farmer (1953) dealt with a two-layer exchange flow for estuaries with a narrow and short opening to the sea. The basic idea is that the exchange is internally controlled such that the velocity would not increase beyond the point at which long interfacial waves become stationary.

A comprehensive analysis of exchange flow has been presented by Armi & Farmer (1986) and Farmer & Armi (1986), in which various topographies as well as the effects of a barotropic net flow were considered. One of the key results of the analysis was that a maximal exchange always occurs when subcritical flow in the strait is bounded at both ends by supercritical flows. Some other studies concerning general formulation of two-layer hydraulics include, for example, two-layer exchange flows through a channel with a contraction (Wood, 1970), two-layer flows over a broad-crested weir (Wood & Lai, 1972), two-layer flows over a sill (Long, 1954, 1974; Baines, 1984; Lawrence, 1993; Zhu &

Lawrence, 1996), and two-layer exchange flow through the combination of a sill and contraction (Armi, 1986; Dalziel, 1988, 1991).

With a few exceptions, previous studies on exchange flows have been mainly concerned with inviscid flows. The frictional effects, however, can not always be ignored, except for those dynamically short channels where inertial forces are dominant over frictional forces. Anati *et al.* (1977) classified the length of the channel according to the relative magnitude between the bottom friction and the inertial force. The channel is short such that the bottom frictional term $f_b U^2/H$ is negligible compared with the acceleration term U^2/L. Thus the relative importance of friction can be indicated by a single frictional parameter:

$$\alpha = \frac{f_b U^2/H}{U^2/L} = f_b L/H \quad , \qquad (2\text{-}1)$$

where f_b is the bottom frictional coefficient, H and L are the total depth and length of the channel respectively. A channel is considered to be short if α « 1, long if α » 1, and marginal if $\alpha \approx 1$. Many well-known straits can not be considered short even based on conservative values of bottom friction factors, as shown in Table 2-1.

Table 2-1 Values of α for various sea straits

Sea Strait	Length L (km)	Depth H (m)	f_b	α
Strait of Gibraltar (Defant, 1961)	60	300	0.012	2.4
Bosphorus (Assaf & Hecht, 1974)	30	60	0.005	2.3
Dardanelles (Assaf & Hecht, 1974)	60	70	0.012	10.3
Bab-el-Mandeb (Assaf & Hecht, 1974)	160	180	0.012	11.2
Vema Channel (Pratt, 1986)	200	300	0.005	3.5
Bornholm Strait (Pratt, 1986)	250	30	0.005	41.7
Denmark Strait (Pratt, 1986)	500	500	0.005	5.0
Ecuador Trench (Pratt, 1986)	300	300	0.005	5.0
Iceland-Foroe Ridge (Pratt, 1986)	400	400	0.005	5.0
Bering Strait (Pratt, 1986)	100	50	0.005	10.0

For the Burlington Ship Canal, the frictional parameter α is estimated to be about 0.23, based on $H = 9.5\,\text{m}$, $L = 836\,\text{m}$, and $f_b = 0.0026$. This indicates that the ship canal could be considered fairly short on the basis of α alone.

Friction was found to reduce the exchange rates significantly through several well-known sea straits (e.g. Assaf & Hecht, 1974). Friction was also found to reduce the exchange rate considerably through the Burlington Ship Canal (Hamblin & Lawrence, 1990), even through a channel with $\alpha = 0.23$ might otherwise be considered short enough to ignore frictional effects. Friction also causes a shift in the critical location of flow or hydraulic control (Pratt, 1986).

Some of the nomenclature used in this thesis is introduced here. The fluid motion of a two-layer system may be driven either by free surface slope or by internal density variation. The motions driven by deviations in the free surface elevation are referred to as being barotropic; whereas those driven by horizontal deviations in the internal density structure are baroclinic or densimentric. For two-way exchange flow process, the convention adopted is that the more dense water moves from right to left and the less dense water moves from left to right. For single layer flows, information is propagated by long, infinitesimal gravity waves. For two-layer flows, these waves are on the density interface. If the information is able to propagate in both directions and then flow is said to be subcritical. In contrast, if the information is able to propagate in only one direction and the flow is said to be supercritical. The location where a flow changes from subcritical to supercritical is referred to as a hydraulic control. Definitions of other nomenclature are illustrated in Figure 2-1, where ρ_i, y_i and U_i are density, layer thickness and horizontal velocity for layer i respectively. Subscript $i = 1$ always represents the upper layer, while $i = 2$ always represents the lower layer. $\tau_I = \frac{1}{2} f_I \overline{\rho} (\Delta U)^2$ and $\tau_b = \frac{1}{2} f_b \rho_2 U_2^2$ denote interfacial and bottom friction respectively, where $\overline{\rho}$ is the mean density of two layers, f_I is the interfacial frictional coefficient, and the velocity shear $\Delta U = |U_1 - U_2|$.

The following sections seek to review the major theoretical, laboratory and field studies on frictional two-layer exchange flows in general and water exchange through the Burlington Ship Canal in particular. The literature review is divided into three sub-sections: first, the description of frictional exchange flows by two-layer internal hydraulics in general, secondly, the previous studies on exchange flows in the Burlington Ship Canal, and finally, the attempts to predict the interfacial friction factors.

2.2 FRICTIONAL TWO-LAYER EXCHANGE FLOWS

The frictional effects on the motion of two-layer flows were first introduced by Schijf & Schonfeld (1953) by considering the dynamic balance and continuity of each layer in their theoretical formulation of salt-water intrusion problems. Frictional effects were later considered by other authors in their studies on exchange flow problems.

Assaf & Hecht (1974) developed a steady two-layer hydraulic numerical model to study frictional exchange flows through sea straits. Both interfacial and bottom friction forces were included and maximal exchange was assumed with the critical flow condition imposed at each end of the strait. Given frictional factors and exchange flow rates, the model predicts the interface slopes and salinity ratios of several well-known sea straits including the straits of Gibraltar, the Bosphorus, the Bab-el-Mandeb and the Dardanelles straits. It was found that friction has a significant effect on the interface slope along the strait, and reduces the flow rate significantly. Their model also indicates that the interface is almost linear throughout most of the strait and strongly curved at the outlet of the lower layer, as shown in Figure 2-2. This is due to the facts that a trapezoidal shape has been used to represent the natural channel cross-sections and the surface friction is assumed to be absent in their model. It is noted, however, that their numerical integration procedure stopped slightly short to reach the critical condition at the right end of the channel ($x = L$) to avoid the integral divergency at critical

condition. Moreover, the opposite problem of computing the exchange flow rate from given salinity ratio and frictional factors was not attempted in their studies. Other numerical models concerning steady frictional exchange problems include, for example, Holley & Waddell (1976) investigating water exchange through Great Lake culvert and Oguz *et al.* (1990) studying exchange flows in the Bosphorus strait.

In seeking to develop a simple analytical solution to frictional exchange flow problems, Anati *et al.* (1977) suggested a criterion for identifying the dynamic length of sea straits using a single frictional parameter α, as defined in (2-1). For short strait, i.e. $\alpha << 1$, the frictional forces are negligible, and the exchange flow would be dominated by the non-linear process of hydraulic control. The resulting exchange flow is such that the composite Froude number is unity within the strait, as suggested by Stommel & Farmer (1953). If the strait is long, i.e. $\alpha >> 1$, the composite Froude number would be much less than unity within the strait but increases to unity at each end. A simple theoretical model was developed to solve the exchange flows through long straits, where non-linear inertial forces can be neglected compared with bottom friction. Assuming a linear interface profile throughout the channel, the interface deflection was expressed implicitly as a function of the frictional parameter α only:

$$2\beta\left(1+3\beta^2\right)=\alpha\left(1-\beta^2\right)^2, \qquad (2\text{-}2)$$

where $\beta = d/H$ is the non-dimensional interface deflection, d is the change in the depth of the interface from one end of the strait to the other, and H is the total depth. Given the interface deflection through the channel, the exchange rate is then determined by the hydraulic control conditions at either end of the channel.

Laboratory experiments were also carried out by Anati *et al.* (1977) to verify their theoretical predictions. Their long channel experiment, as depicted in Figure 2-3, indicates that a nearly

linear density interface within the channel with fairly strong curvature at both ends. This is much like the solutions of Assaf & Hecht (1974). Other attempts to develop simple analytical solutions to exchange flows through long channels include Maderich & Efroimson (1990) and Maderich & Oleksiuk (1994). It is also noted that the exchange flow laboratory experiments conducted by Anati *et al.* (1977) and Maderich & Oleksiuk (1994) were carried out on fairly small physical scales.

The linear frictional exchange flow models proposed by Anati *et al.* (1977), Maderich & Efroimson (1990) and Maderich & Oleksiuk (1994) are only applicable to exchange flows through very long channels. Those models, however, have no immediate application to the Burlington Ship Canal, where both inertial and frictional forces are equally important and should be included in the theoretical formulation. Secondly, all analyses ignored the interfacial friction forces, which could be in the same order as friction on the bottom or sidewalls of the channel (Dermissis & Partheniades, 1984). Finally, no precise interface profile was calculated so far, instead linear interface profiles were assumed as the first approximation to the actual density interface position throughout the channel.

The effects of steady or quasi-steady barotropic flow on the dynamics of exchange flows have also attracted some research interests. Bormans & Garrett (1989b) examined the effects of barotropic flows on the mean flow and fluctuating two-layer exchange in the Strait of Gibraltar. It was found that low-frequency barotropic flows significantly alter the volume flux and interface depth along the strait. The barotropic flows also allow comparison of the model predictions with the observed sea level data. There have been relatively few laboratory experiments conducted so far on two-layer exchange flows with barotropic flow

components, except that of Stigebrandt (1977) and Helfrich (1995) both concerning time-dependent inviscid exchange flow problems.

In addition to friction and barotropic flow, some other effects have also been considered in the dynamics of strait and sill exchange flows by many authors. These efforts include Stigebrandt (1977) discussing the effect of barotropic current fluctuations on two-layer exchange through a constriction, Helfrich (1995) considering the effect unsteady barotropic flow on two-layer exchange through a pure contraction as well as the combination of a sill and contraction, Bormans & Garrett (1989a) and (1989b) investigating the effects of rotation of the earth and cross channel geometry on exchange flows through the Strait of Gibraltar, and Zhu & Lawrence (1998) studying the non-hydrostatic or curvature effect on exchange flow through a channel with an underwater sill.

2.3 EXCHANGE FLOWS IN THE BURLINGTON SHIP CANAL

The exchange flow through the Burlington Ship Canal was first noted by Dick & Marsalek (1972, 1973b), who observed two distinct flow regimes. They are the unidirectional open channel flow caused by a difference in water levels between the Hamilton Harbour and Lake Ontario, and the densimetric exchange flow with lighter, warm harbour water flowing out in the upper layer and denser, cool lake water flowing into harbour in the bottom layer. The densimetric exchange flows can be observed during summer months while the unidirectional open channel flows occur during the remainder of the year. The velocity and temperature profiles measured during the summer of 1971 were used to compare with the predicted interface slope for a range of friction factors. However, the more difficult and yet important

task of computing the exchange flow rate from given temperature profiles and water levels at either end of the canal was not attempted in their studies.

Other attempts to quantify the exchange flows in the Burlington Ship Canal include those of Kohli (1979) and Palmer & Poulton (1976). However, the estimates of exchange flows from their current measurements in the ship canal were considered erroneous, due to inadequate number and improper positioning of the current meters (Klapwijk & Snodgrass, 1985). Given difficulties associated with measuring long-term exchanges directly using current meters, Klapwijk & Snodgrass (1985) suggested that, alternatively, the flushing rate of Hamilton Harbour could be determined using mass balance of conservative substances, as measured by conductivity. The monthly pattern of exchange flows obtained from their study shows a distinct peak in the late summer and early autumn (i.e. from July to October) when the stratification is strong.

A more extensive field measurement program was carried out from May to September, 1988 (Spigel, 1989). Unlike some previous studies, the program was designed to provide a broad overview of the physical processes occurring in the harbour-canal system, rather than concentrate on a single process or location. It is indicated that the density driven two-way densimetric exchange flow within the ship canal is frequently modified by barotropic forcing so that either flow in one direction is greater than the other, or the two-way exchange flow is even overwhelmed to yield a unidirectional flow.

The highly episodic nature of exchange flow is largely due to the seiching activities or Helmholtz resonances in Lake Ontario (Freeman *et al.*, 1974; Tedford, 1999). The situation is further complicated by the relatively small volume of the Hamilton Harbour. The volume of barotropic flows between Lake Ontario and the harbour depend on the surface area of the

harbour. Dick & Marsalek (1973b) indicated that landfilling from 1926 to 1972 resulted in an approximate 25% decrease in harbour surface area. The decreasing harbour surface area reduces the duration and magnitude of barotropic flows, and hence makes them less effective in water exchange between the harbour and the lake. This is because relatively small surface area of the harbour requires less flow to overcome a given water level difference between the lake and the harbour.

The effectiveness of barotropic fluctuations on two-way exchange flows depends on the ratio of the excursion to the length of the connecting channel. If the inflows from the lake are "short-circuited" to the outflows without effectively mixing with the main body of the harbour water, the inflows will have little benefit in flushing the harbour. The frequent flow reversals or oscillations of exchange flows in the Burlington Ship Canal were identified as one of lake water's "short-circuiting" mechanisms by Kholi (1984). It was found that, for barotropic driven one-way exchange flows, inflow excursions of about twice the channel length are required to significantly mix the two water bodies (Hamblin, 1996).

The field data of Spigel (1989) were used by Hamblin & Lawrence (1990) to demonstrate the importance of frictional effects on exchange flows in the ship canal. It was shown that friction has a significant effect on the mean two-way exchange flow rate and brings the model predictions closer to the flow measurements, as shown in Figure 2-4. The work of Hamblin & Lawrence (1990) marked the first attempt to solve the two-way exchange flow rate through the ship canal by internal hydraulic theory.

2.4 INTERFACIAL FRICTION

An accurate estimate of interfacial friction coefficient has not been established so far. Despite numerous efforts to develop empirical or semi-empirical equations for interfacial friction factor as a function of pertinent flow parameters, such as Reynolds, Froude, and Keulegan numbers, there is no commonly accepted theoretical basis and the discrepancy between prediction and data is large. This is especially the case in the important high Reynolds number range (Dermissis & Partheniades, 1984; Arita & Jirka, 1987). Those efforts include pure data correlation (e.g. Harleman & Stolzenbach, 1972; Dermissis & Partheniades, 1984), analogy to wall friction using Moody diagram (e.g. Abraham & Eysink, 1971; Dick & Marsalek, 1973a; Pederson, 1980), internal wave stability theories (e.g. Tamai, 1976), turbulent similarity theory (e.g. Hino, 1980), and direct turbulent measurements (e.g. Partheniades & Dermissis, 1993; Georgiev, 1972).

Ippen & Harleman (1952) derived the expression for the average frictional coefficient at the laminar interface of density currents, i.e. $f_I = 5.6/\mathrm{Re}_2$, where $\mathrm{Re}_2 = U_2 y_2/\nu$. The dependency of interfacial friction on Reynolds number is also suggested by many other authors such as Bata (1959), Georgiev (1972), Harleman & Stolzenbach (1972), and Abraham *et al.* (1979). Harleman & Stolzenbach (1972) plotted the interfacial frictional coefficients for density currents from a number of authors against the Reynolds number ranging from 10^2 to 10^7. The scatter in the high Reynolds number range, however, exceeds one order of magnitude. Abraham *et al.* (1979) suggested that subcritical stratified flows may be treated as two-layer flows without mixing, due to the stabilizing effects of an intermediate layer as it eliminates the instability of internal waves, hence reduces turbulence.

Indeed instability and internal wave breaking, although they may be intermittent and may take many different forms, are ubiquitous features in geophysical and engineering stratified flows. The early experiments of Keulegan (1949) on salt wedge flows indicated that when

the relative velocity between the two layers is small, the flow is laminar, however, when this velocity is increased up to the formation of ridges and waves, the flow becomes turbulent. Indeed the turbulent contribution to the total interfacial friction can be important as some field data of Spigel (1989) indicate the presence of large scale interfacial instabilities, as shown in Figure 2-5. Dermissis & Partheniades (1984) pointed out that such equations as that of Ippen & Harleman (1952) could underestimate the interfacial shear by two orders of magnitude as applied to the arrested salt wedge in South Pass of the Mississippi River. Even under laboratory experimental conditions, turbulent interfacial shear stress can be dominant (Zhu & Lawrence, 2000). The turbulent stress is not only a function of mean flow parameters, but also influenced by the nature of interfacial instabilities, as suggested by Lawrence *et al.* (1998).

Lofquist's (1960) experimental study was concerned with turbulent density currents with Reynolds number ranging from 1,000 to 10,000 and densimetric Froude number ranging from 0.02 to 0.4. The study suggested that the interfacial shear stress depend on both the Reynolds and densimetric Froude numbers. Although no specific relations were derived, it was shown that the ratio of the total shear to the viscous shear is increased with increases in both Reynolds and densimetric Froude numbers. A similar trend was also found by Macagno and Rouse (1962) who showed that the ratio of the total shear to the viscous shear is increased from 1 to about 8 with increases in both Reynolds and densimetric Froude numbers. The shear Reynolds number $\mathrm{Re}_\delta = \Delta U \delta / \nu$ in their experiments was up to 4,000 and densimetric Froude number ranged from 0.5 to 3.5, where δ is shear layer thickness. The laboratory experiments of Sargent & Jirka (1987) on salt wedges indicate that turbulent and viscous shear stresses are about equal in magnitude at the density interface, which was marginally stable with respect to intermittent wave breaking. The channel Reynolds number in their experiments ranges from 4,000 to 10,000 and densimetric Froude number ranges from 0.39 to 0.49. The authors, however, were surprised by the large viscous contribution to the

interfacial shear, and suggested that it may be of importance even in larger Reynolds number environments, including field conditions.

Considering the energy dissipation of stable infinitesimal interfacial waves, Tamai (1976) suggested that the interfacial friction coefficient f_I of salt wedge flows is proportional to $K^{-1/2}$, where $K = F_1^2 \,\mathrm{Re}_1$ is the Keulegan number, $\mathrm{Re}_1 = U_1 y_1 / \nu$, and $F_1 = U_1 / \sqrt{g' y}_1$ is the densimetric Froude number. The proportionality constant was determined by best fitting some previous data, including some high Reynolds number field data for arrested salt wedges. The spread of data points at high Reynolds numbers, however, was quite large, possibly due to the presence of interfacial instabilities. Some high Reynolds number field data from several Japanese estuaries were also compiled by Tamai (1976).

The interfacial friction for arrested salt wedges has been examined extensively by many Japanese authors, e.g. Iwasaki (1964) and Shi-Igai (1965), who usually correlated the interfacial friction coefficient f_I to the Keulegan number K. Arita & Jirka (1987) suggested that the interfacial friction on a salt wedge is governed by the local Reynolds number Re_1 as well as the local Richardson number Ri or densimetric Froude number F_1, rather than by a single parameter of Keulegan number $K = F_1^2 \,\mathrm{Re}_1$. Dermissis & Partheniades (1984), on the other hand, found that the interfacial friction coefficient could not be uniquely correlated with either the Reynolds number or the densimetric Froude number or the Keulegan number. It is demonstrated that the average interfacial friction coefficient for arrested salt wedges is best correlated with the number $\mathrm{Re}_1 Fr^2$, with the relative density difference being an independent parameter, here $Fr = U_1 / \sqrt{gH}$ is the regular non-densimetric Froude number.

Most papers published to date on interfacial friction were concerned with arrested salt wedge and density current type of flows. The determination of the interfacial friction coefficient mainly relies on the integration of differential equations of interface slope. The friction coefficient obtained, however, is an average or effective one. Moreover, the friction from

sidewalls of laboratory flumes have not been accounted for by some studies. The effects of unsteadiness of some field data also affect the estimate of the interfacial friction. The problem is further complicated by different velocity and length scales used in paramterization schemes. On the other hand, however, direct measurements of interfacial shear stress are rare, except for Dermissis & Partheniades (1985) and Partheniades & Dermissis (1993) for arrested salt wedges, and Georgiev (1972) for density currents.

Georgiev (1972) measured interfacial friction by a particle tracing technique in density currents. His data seem to indicate a dependence of interfacial friction on Reynolds number only. The Reynolds numbers in his experiments range from 1,000 to 10,000 and the densimetric Froude number range, however, is not given. In a more recent paper, however, Georgiev (1990) suggested that interfacial friction should depend on the type of the flow, and the combined effects of viscous forces expressed by Reynolds number and interfacial instability expressed by the densimetric Froude number or Richardson number. Partheniades & Dermissis (1993) measured the velocity distribution and interfacial shear stresses in arrested salt wedges using a hot film anemometer. Their experiments indicate severe damping of the turbulent velocity fluctuations and the Reynolds shear stresses near the density interface. As a result, the Reynolds interfacial friction only represents a very small amount (in the order of 3%) of the total interfacial friction. The Reynolds number and the densimetric Froude number ranges, however, were not given.

CHAPTER 3

THEORETICAL FORMULATION

3.1 BASIC ASSUMPTIONS AND FLOW CONFIGURATION

Many flows of geophysical, oceanographic, meteorological, and engineering importance can be modelled as two-layer flows. Some assumptions, well known as the hydraulic assumptions, are used in the study of two-layer flows. These assumptions include: (1) negligible streamline curvature, i.e. the pressure is hydrostatic, (2) the flow within each layer is assumed to be of constant velocity varying only in the flow direction, and (3) no entrainment or mixing across the density interface; therefore the density is constant within each layer. The momentum exchange as a result of interfacial mixing, however, is indirectly included in the interfacial friction factors.

Consider two large reservoirs connected by either an open channel or culvert. The reservoirs may consist of a semi-enclosed basin on one side and a more open water body, such as an ocean or a lake, on the other. The basins may have a source of positive or negative buoyancy, such as fresh water run-off, surface heating, thermal loading and evaporation. As a result, two reservoirs may contain fluids of slightly different densities. The small density difference drives an exchange flow through the channel.

An important simplification, which essentially isolates the most important features of frictional exchange flows, is that the channel or culvert is horizontal and of constant width with sudden expansions at both ends, as sketched in Figure 3-1. It is also assumed that the channel or culvert is relatively wide, i.e. its width is much larger than its depth. This flow configuration also closely resembles the flow conditions in the Burlington Ship Canal.

The exchange flow is considered to be steady or quasi-steady, when $\gamma = 0$ or $\gamma \to \infty$ (Helfrich, 1995). The time parameter $\gamma = T\sqrt{g'H}/L$ is the inverse measure of the channel length relative to the internal wave travelling distance in a forcing period, where g', L, H, and T are the reduced gravity, length and depth scales of the channel, and the forcing period respectively. For $\gamma = 0$, the time-dependent terms are absent, and unforced steady exchange flow is achieved. While for $\gamma \to \infty$, the temporal variations tend to be zero, and the quasi-steady limit is reached.

The effect of Coriolis force is also ignored. Therefore, the application of the analysis is confined to channels that are much narrower than the internal Rossby radius of deformation. The friction is parameterised using the quadratic law in the theoretical analysis. Furthermore, the frictional factors will be assumed to be constant throughout the channel. Hence, frictional factors used are considered average or effective ones.

For the two-layer exchange flow through an open channel, the relative density difference between the two fluid layers is much less than that at the free surface, so that the free surface may be assumed horizontal. This is often referred to as the rigid-lid approximation. Thus the analysis presented in this study is equally applicable to exchange flows beneath frictionless rigid lids. For culvert exchange flow considered, the culvert is always assumed to flow full.

3.2 GOVERNING EQUATIONS

The non-linear nature of exchange flows, such as the asymmetry of interface along the axis of the flow in many straits and channels, cannot be explained by the linear exchange flow theory, which ignores the non-linear inertial terms in the theoretical formulation. Thus one-dimensional hydraulic or shallow water equations must be used to describe the fully non-linear problems of exchange flows.

Consider the mechanical energy per unit volume or Bernoulli constant for each layer:

$$E_i = P_i + \rho_i g y + \tfrac{1}{2}\rho_i U_i^2, \tag{3-1}$$

where P_i, ρ_i and U_i are the pressure, the density and the horizontal velocity for layer i respectively. Subscript $i=1$ represents the upper, and subscript $i=2$ represents the lower layer. g is the gravitational acceleration, and y is the vertical co-ordinate. The pressure term P_i for each layer is expressed as:

$$P_1 = \rho_1 g(H - y), \tag{3-2a}$$

and

$$P_2 = \rho_1 g y_1 + \rho_2 g(y_2 - y), \tag{3-2b}$$

where $H = y_1 + y_2$ is the total fluid depth, and y_i is the thickness of layer i.

Defining the internal energy head, E, of a two-layer flow system as:

$$E = \frac{E_2 - E_1}{(\rho_2 - \rho_1)g}. \tag{3-3}$$

It is noted that unlike its counter-part in one-layer open channel flows, the internal energy for a two-layer flow system can be negative.

Substituting (3-1) and (3-2) into (3-3) leads to:

$$E = y_2 + \frac{1}{2g'}\left(U_2^2 - rU_1^2\right), \tag{3-4}$$

where $g' = \varepsilon g$ is the reduced gravity, $\varepsilon = (\rho_2 - \rho_1)/\rho_2$ is the relative density difference, and $r = \rho_1/\rho_2 = 1 - \varepsilon$ is the density ratio.

Schijf & Schonfeld (1953) first included bottom and interfacial shear stresses in studying the salt-water intrusion into estuaries and rivers. The exchange flow through a channel or culvert is subject to frictional forces from the sidewall, the bottom, the surface and the density

interface, as shown in Figure 3-2. The energy loss due to shear stress for layer i can be expressed as (Cheung & Lawrence, 1991):

$$\frac{dE_i}{dx} = \frac{\sum_i \tau_i \cdot dS_i}{A_i \cdot dx}, \tag{3-5}$$

where $\sum$ is the summation of the shear stress, τ_i, acting on the layer i, S_j is the area over which the shear stress acts on the layer, and $A_i = by_i$ is the layer cross section area, with b being the channel width and y_i the layer thickness. Subscripts $i = 1, 2$ refer to the upper and the lower layer respectively.

The shear stresses acting on the four surfaces are expressed by the following equations:

sidewall $$\tau_w = \tfrac{1}{2} f_w \rho_i U_i^2, \tag{3-6a}$$

surface $$\tau_s = \tfrac{1}{2} f_s \rho_1 U_1^2, \tag{3-6b}$$

bottom $$\tau_b = \tfrac{1}{2} f_b \rho_2 U_2^2, \tag{3-6c}$$

density interface $$\tau_I = \tfrac{1}{2} f_I \overline{\rho} (\Delta U)^2, \tag{3-6d}$$

where f_w, f_s, f_b and f_I are wall, surface, bottom and interfacial friction factors respectively, $\overline{\rho} = (\rho_1 + \rho_2)/2$ is the mean density of two layers, and $\Delta U = |U_1 - U_2|$ is the velocity shear between two layers.

The right side of (3-5) for each layer is evaluated by:

$$\frac{\sum \tau_1 dS_1}{A_1 dx} = -f_w \rho_1 U_1^2 \frac{1}{b} - \tfrac{1}{2} f_I \overline{\rho} (\Delta U)^2 \frac{1}{y_1} - \tfrac{1}{2} f_s \rho_1 U_1^2 \frac{1}{y_1}, \tag{3-7a}$$

$$\frac{\sum \tau_2 dS_2}{A_2 dx} = f_w \rho_2 U_2^2 \frac{1}{b} + \tfrac{1}{2} f_I \overline{\rho} (\Delta U)^2 \frac{1}{y_2} + \tfrac{1}{2} f_b \rho_2 U_2^2 \frac{1}{y_2}. \tag{3-7b}$$

Substituting Equation (3-5) into (3-3) and rearranging terms yields:

$$\frac{dE}{dx} = S_f , \tag{3-8}$$

where S_f is the internal energy slope or friction slope, defined analogous to that in single layer hydraulics (e.g. Henderson, 1966), with

$$S_f = \frac{f_w}{b}\left[F_1^2 y_1 + F_2^2 y_2\right] + \frac{1}{2} f_I F_\Delta^2 \frac{H^2}{y_1 y_2} + \frac{1}{2} f_b F_2^2 + \frac{1}{2} f_s F_1^2 , \tag{3-9}$$

where $F_i^2 = U_i^2 / g' y_i$ is the densimetric Froude number of layer i, and $F_\Delta^2 = \Delta U^2 / g' H$ is the stability Froude number (Lawrence, 1990).

If the flow is steady, flow rates Q_1 and Q_2 do not vary along the channel. Substituting Equation (3-4) and $U_i y_i b = Q_i$ = constant into Equation (3-8) yields equation of motion for the depth of lower layer, y_2, of two-layer flows:

$$\frac{dy_2}{dx} = \frac{S_f - S_o}{1 - G^2} , \tag{3-10}$$

where $G^2 = F_1^2 + F_2^2 - \varepsilon F_1^2 F_2^2$ is the composite Froude number. $S_o = (rF_1^2 y_1 - F_2^2 y_2)\frac{1}{b}\frac{db}{dx} + rF_1^2 \frac{dH}{dx}$ is the topographical slope due to the sudden expansion at both ends of the channel, where $dH/dx = 0$, due to horizontal channel bottom and negligible free surface slope.

Instead of using the principal of energy conservation, the equation of motion in the form of (3-10) can also be derived by re-arranging the continuity and momentum equations for the two layers originally given by Schijf & Schonfeld (1953), as shown by Dick & Marsalek (1973). The equation of motion is equally applicable to both densimetric exchange flows and exchange flows with a barotropic flow component.

It is noted that G^2 rather than G is used, since it is the form that appears in the solutions of the hydraulic equations. For small densimetric Froude number and density difference, the composite Froude number can be simply written as:

$$G^2 = F_1^2 + F_2^2 . \tag{3-11}$$

In single layer flows, the flow is said to be supercritical, critical, or subcritical depending on the Froude number Fr is greater than, equal to, or less than unity. $Fr = U/\sqrt{gH}$ is defined as the ratio of the convective velocity, U, to the phase speed of the infinitesimal long gravity wave, $\sqrt{gH}$. Comparison of (3-10) with its single layer counterpart, $\frac{dy}{dx} = \frac{S_o - S_f}{1 - F_r^2}$, suggests that the composite Froude number G^2 may determine the criticality of the two-layer flow just as the non-densimetric Froude number Fr determines the criticality of the single-layer flow. It is, however, not immediately clear how the parameter G^2 can be used to determine the criticality of two-layer flow, since the definition of a single convective velocity for two-layer flows is not as straight forward as in single-layer flows. Furthermore, the phase speed of internal (interfacial) long waves is subject to the influence of velocity shear in two-layer flows, as suggested, for example, by Watson (1994). The concepts of hydraulic control as well as maximal exchange for two-layer flows will be discussed in the context of internal long wave propagating in a two-layer shear flow.

3.3 PROPAGATION OF INFORMATION AND HYDRAULIC CONTROL

For single layer flow, information is propagated by infinitesimal long gravity waves. As with its single-layer counterpart, information is propagated by infinitesimal long interfacial waves on the density interface of a two-layer flow system. The propagation of such an internal wave is subject to vertical variations of density $\rho(y)$ and mean horizontal velocity $U(y)$.

The behaviour of the internal wave, with characteristic velocity (celerity) λ and wave number k, is governed by the Taylor-Goldstein equation (Taylor, 1931; Goldstein, 1931):

$$[\rho(U-\lambda)v']' - (\rho U'v)' - \left[\frac{\rho' g}{(U-\lambda)} + \rho k^2 (U-\lambda)\right] v = 0, \qquad (3\text{-}12)$$

where the prime denotes differentiation with respect to y, and $v(y)$ is the vertical velocity. The characteristic velocity λ of an internal long wave is the sum of a convective velocity u_c and a phase speed c.

The two-layer flow system analyzed represents two layers of fluid with different uniform velocities and densities separated by a so-called vortex sheet (Leblond, 1978) at the level $y=0$, as shown in Figure 3-3. The term of vortex sheet is used, since all the vorticity of the defined two-layer flow system is concentrated at the interface. The flow is bounded by a solid boundary at the bottom and by a free surface at the top.

Since both density and horizontal velocity structures are discontinuous at the interface of a two-layer flow system, the Taylor-Goldstein equation must be solved in each layer separately and then two boundary or matching conditions, namely the kinematic and dynamic boundary conditions, are imposed across the interface. No free surface or external wave modes are considered here, as the free surface is assumed as a rigid-lid in this study.

The requirement for the continuity of interfacial displacement leads to the kinematic boundary condition:

$$v|_{0+} = v|_{0-}, \qquad \text{at } y=0, \qquad (3\text{-}13)$$

while the requirement for the continuity of total pressure leads to the dynamic boundary condition:

$$\rho\left[(U-\lambda)v' - vU' - \frac{gv}{(U-\lambda)}\right]_{0+} = \rho\left[(U-\lambda)v' - vU' - \frac{gv}{(U-\lambda)}\right]_{0-}, \quad \text{at } y=0. \qquad (3\text{-}14)$$

Given $U''=0$ and $\rho'=0$ within each layer for the two-layer flow system considered, Equation (3-12) then reduces to:

$$v''-k^2v=0. \tag{3-15}$$

The solutions to Equation (3-15) in each layer are:

$$v=\begin{cases} C_1\sinh k(y_1-y), & 0<y\le y_1 \\ C_2\sinh k(y_2+y), & -y_2\le y<0 \end{cases} \tag{3-16}$$

where y_1 and y_2 are upper and lower layer depths respectively, C_1 and C_2 are constants of integration.

Application of two boundary conditions of (3-13) and (3-14) leads to two homogeneous equations for coefficients C_1 and C_2:

$$\sinh(ky_1)C_1-\sinh(ky_2)C_2=0, \tag{3-17a}$$

$$\left[r(U_1-\lambda)^2k\cosh(ky_1)+rg\sinh(ky_1)\right]C_1+\left[(U_2-\lambda)^2k\cosh(ky_2)-g\sinh(ky_2)\right]C_2=0, \tag{3-17b}$$

where $r=\rho_1/\rho_2$ is the density ratio, and for long internal waves (i.e. $ky_1, ky_2\to 0$), $\sinh(ky_1)\approx ky_1$, $\sinh(ky_2)\approx ky_2$, and $\cosh(ky_1)=\cosh(ky_2)\approx 1$.

For a nontrivial solution of (3-17), requirement of the determinant of the coefficients to be zero leads to the following eigenvalue equation of λ for infinitesimal long interfacial waves:

$$(y_1+ry_2)\lambda^2-2(ry_2U_1+y_1U_2)\lambda+\left(ry_2U_1^2+y_1U_2^2\right)-g'y_1y_2=0. \tag{3-18}$$

Applying the Boussinesq approximation (i.e. ignoring the variation of density except in the buoyancy term) and solving (3-18) yield the expression of the characteristic velocity λ of internal long waves, expressed as the sum of a convective velocity u_c and a phase speed c:

$$\lambda_\pm=u_c\pm c=\frac{U_1y_2+U_2y_1}{H}\pm\left[\frac{g'y_1y_2}{H}(1-F_\Delta^2)\right]^{1/2}. \tag{3-19}$$

The obtained characteristic velocity λ of an internal long wave is consistent with the Boussinesq results of Schijf & Schonfeld (1953) and Lawrence (1990) derived through different methods. In the absence of mean flow, i.e. $U_1 = U_2 = 0$, the characteristic velocity λ reduces to the interfacial wave phase speed $c_I = \sqrt{(g' y_1 y_2)/H}$ of a two-layer flow system (Turner, 1973). With $U_1 \neq 0$ and/or $U_2 \neq 0$, however, the information propagates relative to a weighted mean flow $u_c = \overline{U} = (U_1 y_2 + U_2 y_1)/H$ with a phase speed $c = \pm\sqrt{c_I^2 (1 - F_\Delta^2)}$ provided, of course, the stability Froude number $F_\Delta^2 < 1$. On the other hand, if $F_\Delta^2 > 1$, the flow is unstable, and the flow is marginally or neutrally stable when $F_\Delta^2 = 1$. $F_\Delta^2 \leq 1$ is referred to as Long's stability criterion for long internal waves (Long, 1956).

The propagation of information by infinitesimal long interfacial waves on the density interface of a two-layer flow can be demonstrated by characteristic curves or simply characteristics on the $x-t$ plane, where x is the distance along the channel and t is time. Considering a steady two-layer flow system, which is then slightly disturbed in some way, giving rise to an unsteady flow condition as the small disturbance is propagated into the initially steady region. The paths of the disturbance can be traced on the $x-t$ plane as two families of characteristics, C_+ and C_-, with inverse slopes of $\lambda_+ = (u_c + c)$ and $\lambda_- = (u_c - c)$ respectively, as shown in Figure 3-4. If λ_+ and λ_- are of opposite signs, i.e. $|u_c| < c$, the disturbance is able to propagate in both directions and flow is subcritical. On the other hand, if λ_+ and λ_- are of the same signs, i.e. $|u_c| > c$, the disturbance is only able to propagate in one direction and flow is supercritical. Finally, if λ_+ or λ_- is equal to zero, $|u_c| = c$, the flow is critical.

Similar to single-layer flows, an internal Froude number F_I^2 can be defined as the ratio of the internal convective velocity to the internal phase speed (Lawrence, 1990):

$$F_I^2 = \frac{u_c^2}{c^2} = \frac{(U_1 y_2 + U_2 y_1)^2}{g' y_1 y_2 H (1 - F_\Delta^2)}. \qquad (3\text{-}20)$$

The internal Froude number determines the criticality of two-layer flows just as the non-densimetric Froude number, Fr, determines the criticality of single-layer flows. If $F_I^2 < 1$, i.e. the convective velocity u_c is smaller than the phase speed of internal waves c, the flow is subcritical. On the other hand, if $F_I^2 > 1$, i.e. u_c is larger than c, the flow is supercritical. Finally, if $F_I^2 = 1$, i.e. u_c is equal to c, flow is critical.

In two-layer flows, however, the composite Froude number, G^2, has been widely used to determine the criticality of the flows, as it conveniently defines the singularity condition of the two-layer flow system, as shown in (3-10). Rearranging the composite Froude number, $G^2 = F_1^2 + F_2^2$, in terms of velocity ratio leads to:

$$G^2 = F_1^2 + F_2^2 = \frac{U_1^2 y_2 + U_2^2 y_1}{g' y_1 y_2} = \frac{u_c^2}{c_I^2}, \qquad (3\text{-}21)$$

where $c_I = \sqrt{(g' y_1 y_2)/H}$ is the phase speed of internal long wave of two-layer flows in the absence of velocity shear, and $u_c = \sqrt{(U_1^2 y_2 + U_2^2 y_1)/H}$ is the convective velocity defined as some kind of weighted mean flow.

It is, however, not immediately obvious how the criticality of two-layer flows can be determined by the composite Froude number G^2. Much of the confusion comes from the fact that c_I, rather then $c = \sqrt{c_I\left(1 - F_\Delta^2\right)}$, is used as the phase speed of infinitesimal long interfacial waves, since the propagation of such a wave is influenced the vortex sheet located at the level of the density interface. The definition of the convective velocity u_c in (3-21) is also in odds with that defined in (3-19).

In the absence of the velocity shear, i.e. $\Delta U = |U_1 - U_2| = 0$, the phase speed c reduces to c_I and both convective velocities u_c used in (3-21) and (3-20) would also be same. Consequently, the internal Froude number, F_I, is identical with the composite Froude number, G, under this special circumstance.

The more general relationship between the two Froude numbers for two-layer flows are presented by Lawrence (1990):

$$\left(1-G^2\right)=\left(1-F_\Delta^2\right)\left(1-F_I^2\right). \tag{3-22}$$

Under stable flow conditions (i.e. $F_\Delta^2<1$), $\left(1-G^2\right)$ and $\left(1-F_I^2\right)$ are of same signs. Hence G^2 determines the criticality of two-layer flows just as Fr^2 determines the criticality of single-layer flows. The two-layer flow is said to be supercritical, critical, or subcritical depending on composite Froude number G^2 is greater than, equal to, or less than unity.

Alternatively, the composite Froude number, $G^2 = F_1^2 + F_2^2$, can be rewritten as:

$$G^2=1+\frac{\lambda_+\lambda_-}{c_I^2}. \tag{3-23}$$

The composite Froude number is the parameter that characterizes the essential nonlinearity of the flow. Armi (1986) indicates that a necessary condition for an asymmetrical interface under steady conditions is that the flow passes through one or more critical points in the channel.

3.4 ANALYTICAL PROPERTIES OF CRITICAL FLOW AND MAXIMAL EXCHANGE

Consider the frictional exchange flow through a flat rectangular channel of width b, as shown in Figure 3-1. Rewriting the internal energy equation (3-4) yields:

$$E=y_2+\frac{1}{2g'}\left(U_2^2-rU_1^2\right)=y_2+\frac{1}{2g'}\left(\frac{q_2^2}{y_2^2}-\frac{rq_r^2q_2^2}{\left(H-y_2\right)^2}\right), \tag{3-4}$$

where $q_r = q_1/-q_2$ is the flow rate ratio between the two layers. In the absence of a barotropic flow component, $q_r = 1$. $r = \rho_1/\rho_2$ is the density ratio between the two layers. For Boussinesq flows, the density difference is small and hence $r \approx 1$.

Consider how the internal energy E will vary with lower layer depth y_2 for a given value of flow rate q_2. Rearranging (3-4) and applying the Boussinesq approximation lead to:

$$\frac{(E - y_2)y_2^2(H - y_2)^2}{(H - y_2 + q_r y_2)(H - y_2 - q_r y_2)} = \frac{q_2^2}{2g'} \qquad (3\text{-}24)$$

If the flow is steady, q_1 and q_2 (q_r and q_2) do not vary along the channel. Therefore, for a given choice of q_r, if q_2 can be determined at some point along the channel, solutions to (3-24) with constant q_2 would completely define the flow at any point within the channel. This leads to the construction of curves with constant q_2 on the $E - y_2$ plane, as shown in Figure 3-5a for densimetric exchange flows (i.e. $q_r = 1$ and $q_1 = -q_2 = q$).

The curves with constant q^2 shown have asymptotes $y_2 = 0$, $y_2 = H$ and $y_2 = E$ on the $E - y_2$ plane. Curves with higher values of q^2 occur inside of those with lower values of q^2, since for given value of y_2, E increases with q^2 when $y_2 < H/2$ and decreases with q^2 when $y_2 > H/2$, as shown in (3-24). The $E - y_2$ plane is sub-divided into four distinct regions by the asymptote $y_2 = E$ and the $G^2 = 1$ curve representing the critical conditions. The two regions bounded by $y_2 = E$ and $G^2 = 1$ represent the subcritical flow regimes (i.e. $G^2 < 1$), while the two regions beyond represent the supercritical flow regimes (i.e. $G^2 > 1$). Since the $G^2 = 1$ curve always intersects the crests of $E - y_2$ curves, the critical flow can be alternatively defined as the flow condition at which the internal energy E is at its extremum for any given flow rate q^2. This can be verified by determining the necessary condition at which the internal energy E is at its extremun. Applying differentiation to (3-4) with respect of y_2:

$$\frac{dE}{dy_2} = 1 - \left(\frac{q_2^2}{g' y_2^3} + \frac{q_r^2 q_1^2}{g'(H - y_2)^3} \right) = 1 - \left(\frac{q_1^2}{g' y_1^3} + \frac{q_2^2}{g' y_2^3} \right),$$

The extremum of E (i.e. $dE/dy_2 = 0$) is achieved when $\frac{q_1^2}{g' y_1^3} + \frac{q_2^2}{g' y_2^3} = 1$, i.e. $G^2 = 1$. Thus the flow is indeed critical when the internal energy E is at its extremum.

For given values of E, q_r^2 and q_2^2, there could be three real solutions of y_2 to the cubic equation of (3-4). Two of the solutions represent supercritical flows, and the third solution represents the subcritical flow. When more than one depth of flow is possible for a given E, q_r^2 and q_2^2, they are referred to as alternate depths (Henderson, 1966). The immediate question arises as to which of the three solutions is more likely to occur in the flow configuration, as shown in Figure 3-1. The internal energy equation of (3-4) in itself provides little clue to this question.

The flow regime for frictional exchange flows through a channel, thus, is determined by the equation of motion, i.e. $\frac{dy_2}{dx} = \frac{S_f - S_o}{1 - G^2}$. Note the frictional slope S_f, as defined by (3-9), is always positive through the channel. At both ends of the channel, the topographical slope S_o jumps from zero to ∞ due to sudden expansion of the channel width. This leads to $S_f - S_o = 0$ at both ends. Therefore the singularity conditions, $G^2 = 1$, must be imposed these locations, and hence flow is critical at both ends of the channel. It should be noted that, in anticipation of sudden channel expansions at both ends, the density interface tends to be increasingly curved as flow approaches the channel exits. As a result, the non-hydrostatic effects become more important at the very close vicinity of both channel ends. Zhu & Lawrence (1998) showed that, when non-hydrostatic effects are included in analysis, the locations of hydraulic controls are slightly shifted inside the channel at which location $S_f - S_c = 0$, where S_c is the slope due to flow curvature. At present study, however, the non-hydrostatic effect associated with streamline curvature is ignored and the exchange flow is assumed to be critical at the exact ends of the channel. Within the channel, $S_o = 0$ and

dy_2/dx is always positive as the more dense water moves from right to left and the less dense water moves from left to right by convention. Therefore, $1-G^2>0$, and thus flow is subcritical within the channel. Therefore, for certain given value of q^2, the points a and b in Figure 3-5a represent the critical flows at the right and left ends of the channel respectively. Hence the subcritical exchange flow within the channel is represented by the curve between these two points. $E_a - E_b$ is the overall internal energy loss due to friction and d is the total deflection of density interface.

The flow regime, characterized by internal hydraulic controls at both ends of the channel, resembles the maximal exchange flow (Armi & Farmer, 1987). This can be demonstrated by studying how the exchange flow rate varies with interface depth for a given internal energy at either end of the channel. Given internal energy $E = E_o$ and $E = H - E_o$ at left and right ends of the channel respectively, Figure 3-5b shows the general form of exchange rate – depth $(q - y_2)$ curves for $q_r = 1$. For $q - y_2$ curve at the left end of the channel (i.e the lower curve), $q \to 0$ when either $y_2 \to 0$ or $y_2 \to E_o$. Similarly, for $q - y_2$ curve at the right end of the channel (i.e. the upper curve), $q \to 0$ when either $y_2 \to H$ or $y_2 \to H - E_o$. There is clearly a maximum value of q for some values of y_2 between 0 and E_o as well as between $H - E_o$ and H.

For any given internal energy E at either end of the channel, the maximum exchange flow rate q_2 for any flow ratio q_r, is obtained by recasting (3-4) into the form:

$$\frac{q_2^2}{2g'}\left(\frac{1}{y_2^2}-\frac{q_r^2}{y_1^2}\right) = E - y_2,$$

and differentiating with respect to y_2:

$$\frac{1}{2}\frac{dq_2^2}{dy_2}\left(\frac{1}{y_2^2}-\frac{q_r^2}{y_1^2}\right)-\left(\frac{q_2^2}{g'y_2^3}+\frac{q_r^2 q_2^2}{g'\left(H-y_2\right)^3}\right)=\frac{dE}{dy_2}-1.$$

Since $dE/dy_2 = 0$ for any given internal energy, the maximum exchange flow rate (i.e. $dq_2^2/dy_2 = 0$) is achieved when

$$\frac{q_r^2 q_2^2}{g'(H-y_1)^3} + \frac{q_2^2}{g'y_2^3} = \frac{q_1^2}{g'y_1^3} + \frac{q_2^2}{g'y_2^3} = G^2 = 1,$$

i.e., the exchange flow is critical.

Hence, the critical flow connotes not only the extremum internal energy for a given exchange flow rate, but also maximal exchange rate for a given internal energy. Since the maximal exchange is achieved without giving specific values for internal energy E, the fundamental requirement for maximal exchange is quite general and equally applicable to both inviscid and frictional exchange flows. The frictional effects certainly reduce the exchange flow rate. However, provided the flow is bounded by hydraulic controls at both ends of the channel, the maximal possible exchange flow rate is still achieved for given frictional conditions.

For maximal two-way exchange flows, the frictional terms act to modify the slope of the interface between the two control locations, while the hydraulic control sections impose boundary conditions to the subcritical flow within the channel. Outside of the control region the flow is supercritical, thus isolating the maximal two-way exchange in the subcritical region from the influence of reservoirs. The maximal exchange flow, in one example, represents the flow between two infinite reservoirs with uniform but different densities. If one or both of the reservoirs is not homogeneous, but has two layers, the maximal exchange requires a hydraulic adjustment or hydraulic jump to separate the subcritical reservoirs from the supercritical flows just outside the controls. If one or both of the reservoir interface heights is such that the hydraulic jump can move back and flood the control, the exchange flow is submaximal or uncontrolled and the flow is subject to reservoir control (Armi & Farmer, 1986).

3.5 ANALYTICAL SOLUTIONS TO TWO-LAYER EXCHANGE FLOWS

The objectives of solving frictional exchange flow problems include the determination of the longitudinal density profile and the exchange flow rate. No matter what the objective might be, the problem always involves the integration of the equation of motion for two-layer flows, as defined by (3-10). Like its single layer counterpart, this equation is not generally solvable by elementary methods. If the channel geometry and forms of resistance equations are both particularly simple, the equation may be solved explicitly (e.g. Bresse function for wide rectangular open channel flows, Henderson, 1966). Otherwise, numerical integration must be used in the analysis. One of the few special cases, in which Equation (3-10) is directly integrable, is frictional exchange flow through a wide rectangular channel or culvert.

Some important non-dimensional parameters are defined here. The internal energy, E, the layer depths, y_1 and y_2, as well as the horizontal distance x are non-dimensionalized with respect to the total fluid depth H and the length of the channel L respectively:

$$E^* = \frac{E}{H},\ y_1^* = \frac{y_1}{H},\ y_2^* = \frac{y_2}{H},\ \chi = \frac{x}{L}. \tag{3-25}$$

The assumption of horizontal free surface or the rigid-lid approximation leads to:

$$y_1^* + y_2^* = 1. \tag{3-26}$$

The non-dimensional interfacial deflection from mid-depth ($y_2^* = y_1^* = \frac{1}{2}$), η, is defined as:

$$\eta = y_2^* - \tfrac{1}{2} = \tfrac{1}{2} - y_1^*. \tag{3-27}$$

In the absence of friction $\eta = 0$ along the entire length of the channel.

By convention, the flow of the less dense water in the upper layer moving from left to right is always positive, and thus the flow of the more dense water in the lower layer moving from

right to left in the lower layer is negative. Hence, the ratio of unit flow rate $q_i = U_i y_i$ ($i = 1, 2$) in each layer is defied as:

$$q_r = \frac{q_1}{-q_2}. \tag{3-28}$$

In steady exchange flows, q_1 and q_2 do not vary along the channel. This constitutes the continuity condition for each layer. For exchange flow without any barotropic component, $q_1 = -q_2 = q$, i.e. $q_r = 1$.

It is convenient to express the velocity of each layer, U_1 and U_2, in the non-dimensional form using $\sqrt{g'H}$ as velocity scale:

$$U_1^* = \frac{U_1}{\sqrt{g'H}},\ U_2^* = \frac{U_2}{\sqrt{g'H}}, \tag{3-29}$$

and the unit flow rate q is non-dimensionalized in the following form:

$$G_o^2 = \frac{16q^2}{g'H^3}, \tag{3-30}$$

where $0 \le G_o^2 \le 1$. G_o^2 is the composite Froude number throughout the channel in the absence of friction (Lawrence, 1993). G_o essentially represents the ratio of exchange flow rate between the frictional and the inviscid exchange flows.

The non-dimensional frictional parameter α is defined as the ratio of bottom friction to inertial force, as proposed by Anati *et al* (1977):

$$\alpha = f_b L/H. \tag{3-31}$$

α is a measure of the relative importance of frictional effects to inertial effects. If $\alpha \ll 1$, the inertial force or hydraulic control is dominant over bottom friction, and the channel is considered to be short. If $\alpha \gg 1$, on the other hand, the bottom frictional effect is dominant,

and the channel is considered to be long. Finally, if $\alpha \approx 1$, both frictional and inertial forces are important, and the channel is considered to be marginal.

The interfacial friction is incorporated by the non-dimensional frictional ratio, f_r, defined as the ratio of the interfacial to the bottom frictional coefficients:

$$f_r = \frac{f_I}{f_b}. \tag{3-32}$$

3.5.1 Maximal Exchange Flow Through a Wide Channel

3.5.1.1 Direct Integration of the Equation of Motion

The sudden expansion of channel leads to discontinuities of channel width, which changes from a finite value of b to ∞ at both ends, as shown schematically in the flow configuration sketch of Figure 3-1. As a result, Equation (3-10) must be integrated within the channel, and then the boundary conditions will be imposed at both ends of the channel. The imposed boundary conditions represent hydraulic controls at both ends and are essential conditions for the existence of maximal exchange flows, as discussed early.

Since the channel width remains constant within the channel, the topographical slope $S_o = 0$ for $0 < x < L$. Equation (3-10) then reduces to the following simplified form:

$$\frac{dy_2}{dx} = \frac{S_f}{1 - G^2}, \qquad 0 < x < L \tag{3-33}$$

where the friction slope $S_f = \frac{f_w}{b}\left[F_1^2 y_1 + F_2^2 y_2\right] + \frac{1}{2} f_I F_\Delta^2 \frac{H^2}{y_1 y_2} + \frac{1}{2} f_b F_2^2 + \frac{1}{2} f_s F_1^2$, as defined in Equation (3-9). Assuming a wide channel (i.e. $H/b << 0$) and zero free surface friction (i.e. $f_s = 0$) leads to $S_f = \frac{1}{2} f_I F_\Delta^2 \frac{H^2}{y_1 y_2} + \frac{1}{2} f_b F_2^2$.

Substituting non-dimensional variables defined in Equations (3-25) to (3-32) and dropping the superscript, *, hereafter lead to the following non-dimensional equation of motion for two-layer open channel exchange flows:

$$\frac{dy_2}{d\chi} = \frac{\alpha G_o^2 (y_1^3 + f_r)}{32 y_1^3 y_2^3 - 2G_o^2 (y_1^3 + y_2^3)}. \tag{3-34}$$

Re-arranging terms in (3-34) and applying integration to both sides of the equation yield:

$$\int \alpha G_o^2 d\chi = \int \frac{32 y_1^3 y_2^3 - 2G_o^2 (y_1^3 + y_2^3)}{(y_1^3 + f_r)} dy_2 . \tag{3-35}$$

It is noted that using y_1 as the independent variable in (3-35) would lead to a much simpler form in the denominator, and hence easier integration procedure. For the reason of simplicity, it will also be assumed, in the following derivation, that the interfacial friction coefficient f_I is the same as the bottom friction coefficient f_b, i.e. $f_r = 1$. Refer to section A.1 of Appendix A for more general solutions to the open channel exchange problem.

Substitute the rigid lid condition (i.e. $y_2 = 1 - y_1$) and $f_r = 1$ into (3-35), which after some manipulation yields:

$$\int \alpha G_o^2 d\chi = \sum_{i=1}^{7} \phi_i , \tag{3-36}$$

where $\phi_1 = -64 \int dy_1$,

$\phi_2 = 96 \int y_1 dy_1$,

$\phi_3 = -96 \int y_1^2 dy_1$,

$\phi_4 = 32 \int y_1^3 dy_1$,

$\phi_5 = \frac{2}{3}\left(7G_o^2 + 8\right) \int \frac{1}{(y_1 + 1)} dy_1$,

$$\phi_6 = -\tfrac{4}{3}\left(2G_o^2 + 1\right)\int \frac{1}{\left(y_1^2 - y_1 + 1\right)} dy_1,$$

$$\phi_7 = \tfrac{2}{3}\left(2G_o^2 + 1\right)\int \frac{y_1}{\left(y_1^2 - y_1 + 1\right)} dy_1.$$

Integrating (3-36) and substituting $y_1 = \frac{1}{2} - \eta$ into the resulting equation then lead to the direct integration of the equation of motion for two-layer open channel exchange flows. The solution expressed as the density interface profile equation is:

$$\alpha G_o^2 \chi = a_1\eta + a_2\eta^2 + a_3\eta^3 + a_4\eta^4 + a_5 \ln\left(\tfrac{3}{2} - \eta\right) + a_6 \ln\left[\eta^2 + \tfrac{3}{4}\right] + a_7 \tan^{-1}\left[\frac{-2\eta}{\sqrt{3}}\right] + a_o, \qquad (3\text{-}37)$$

where $a_1 = 36$,

$a_2 = 12$,

$a_3 = 16$,

$a_4 = 8$,

$a_5 = \tfrac{2}{3}\left(7G_o^2 + 128\right)$,

$a_6 = \tfrac{2}{3}\left(G_o^2 + 8\right)$,

$a_7 = -\tfrac{4}{\sqrt{3}}\left(G_o^2 + 8\right)$,

a_o is the constant of integration.

It should be noted that, without properly defined boundary conditions, the mathematical formulation of the two-layer exchange flow through a wide channel, as expressed by the equation of motion (3-34) for example, is not considered to be well-posed or well-formulated. This is because the obtained analytical solution, as expressed in the form of density interface equation in (3-37), essentially represents infinite number of exchange flow

solutions for unspecified exchange flow rate G_o^2. Furthermore, the analytical solutions obtained may or may not be physically possible at this point.

Generally speaking, a given set of circumstances leads to just one real outcome in nature. In other words, the mathematical solution to the physical problem should be unique under given boundary conditions. For maximal exchange flow problems, this uniqueness of the solution is achieved by imposing two hydraulic control conditions at both ends of the channel, since this flow regime represents the maximal possible two-way exchange flow under the given frictional parameters, as discussed in the previous sections.

Like any hydraulic controls, the imposed critical condition essentially specify a unique G_o^2 (exchange rate) - η (interface depth) relationship at locations where flow regime changes from subcritical to supercritical. The critical conditions at either end of the channel for the maximal exchange flow can be expressed in the following non-dimensional form:

$$G^2 = \frac{G_o^2}{16y_{1j}^3} + \frac{G_o^2}{16y_{2j}^3} = \frac{G_o^2}{16(\frac{1}{2} - \eta_j)^3} + \frac{G_o^2}{16\left(\frac{1}{2} + \eta_j\right)^3} = 1, \quad \text{at } \chi = 0, 1, \qquad (3\text{-}38)$$

where y_{1j}, y_{2j} and η_j ($j = 0, 1$) are upper and lower layer depths and interface deflection at either end of the channel respectively. The left end ($\chi = 0$) and right end ($\chi = 1$) of the channel are identified by $j = 0$ and $j = 1$ respectively. In the absence of friction, the interface is horizontal (i.e. $\eta = 0$, for $0 \le \chi \le 1$), and hence $G_o^2 = G^2 = 1$ throughout the channel.

Equations (3-34) (or its direct integration of 3-37 and 3-38) hence define a typical boundary value problem. The correct solution to the problem essentially represents the flow condition, which matches the resulting internal energy losses under given frictional conditions, and at the same time also satisfies the critical conditions at both ends of the channel.

3.5.1.2 Maximal Exchange Flow as a Boundary Value Problem

The maximal exchange flow solution represents the maximum possible exchange rate for any given frictional parameters α and f_r. This maximal exchange flow condition requires the coexistence of internal hydraulic controls at both ends of the channel (i.e. $\chi = 0$ and $\chi = 1$). In order to define all of the flow properties for maximal exchange as a boundary value problem, it is sufficient to solve the equations describing the flow at the two hydraulic control points, as specified by equations (3-37) and (3-38).

The imposed hydraulic control conditions at each end of the channel correspond to the intersections of direct integration solutions with $G^2 = 1$ at either end of the channel. This leads to the introduction of two sets of solution curves, namely, f_o and f_1 curves. For any given frictional parameters α and f_r, these two solution curves essentially represent the additional $G_o^2 - \eta$ relationship at both ends of the channel, as specified by the direct integration of the equation of motion.

Before deriving for the two solution curves, the following relationship between the interface positions at both ends of the channel needs to be defined. The symmetrical nature of equation (3-38) leads to the following relationship between the lower layer depths at both ends of the channel for maximal two-layer exchange flows:

$$y_{20} + y_{21} = 1 \text{ or } \eta_o = -\eta_1 . \qquad (3\text{-}39)$$

The necessary condition for (3-39) to be valid is that q_1 and q_2 do not vary along the channel, i.e. $q_1 = -q_2 = q$. Therefore, this equation essentially represents the continuity condition of each layer for densimentric exchange flows.

To obtain the two solution curves, substituting $\eta = \eta_o$ at $\chi = 0$ and $\eta = \eta_1$ at $\chi = 1$ into the interface equation of (3-37) respectively, and subtracting the two resulting equations to

eliminate the integration constant a_o. Finally, applying (3-39) (i.e. $\eta_o = -\eta_1$) and rearranging terms lead to the solution curve at $\chi = 0$, i.e. $f_o\left(G_o^2, \eta_o, \alpha, f_r\right)$:

$$G_o^2 = \frac{-72\eta_o - 32\eta_o^3 + \frac{256}{3}\ln\left[\frac{\eta_o + \frac{3}{2}}{-\eta_o + \frac{3}{2}}\right] - \frac{32}{\sqrt{3}}\tan^{-1}\left[\frac{4\sqrt{3}\eta_o}{-4\eta_o^2 + 3}\right]}{\alpha - \frac{14}{3}\ln\left[\frac{\eta_o + \frac{3}{2}}{-\eta_o + \frac{3}{2}}\right] + \frac{4}{\sqrt{3}}\tan^{-1}\left[\frac{4\sqrt{3}\eta_o}{-4\eta_o^2 + 3}\right]}, \qquad \text{(3-40a)}$$

and the solution curve at $\chi = 1$, i.e. $f_1\left(G_o^2, \eta_1, \alpha, f_r\right)$:

$$G_o^2 = \frac{72\eta_1 + 32\eta_1^3 + \frac{256}{3}\ln\left[\frac{-\eta_1 + \frac{3}{2}}{\eta_1 + \frac{3}{2}}\right] - \frac{32}{\sqrt{3}}\tan^{-1}\left[\frac{-4\sqrt{3}\eta_1}{-4\eta_1^2 + 3}\right]}{\alpha - \frac{14}{3}\ln\left[\frac{-\eta_1 + \frac{3}{2}}{\eta_1 + \frac{3}{2}}\right] + \frac{4}{\sqrt{3}}\tan^{-1}\left[\frac{-4\sqrt{3}\eta_1}{-4\eta_1^2 + 3}\right]}, \qquad \text{(3-40b)}$$

where $f_r = 1$ in both (3-40a) and (3-40b) for the reason of simplicity here.

The above two solution curves (i.e. f_o or f_1) and the hydraulic control condition of (3-38) (i.e. $G^2 = 1$) can be solved for each of the three unknowns (G_o^2, η_o and η_1) for given frictional parameters of α and f_r ($f_r = 1$ for the reason of simplicity here). On the $G_o^2 - \eta$ plane, the maximal exchange rate G_o^2 and corresponding interface locations at both ends η_o and η_1 correspond to the intersections of either solution curve with the hydraulic control condition. This leads to the presentation of maximal exchange flow solutions on the $G_o^2 - \eta$ plane, which will be discussed in detail in the separate section later in this chapter.

Solve for the constant of integration a_o by substituting the obtained maximal exchange rate G_o^2 and either η_o or η_1 into the interface profile equation of (3-37). This will lead to a uniquely defined interface position and hence some other important flow parameter (e.g. G^2 and E) variations throughout the whole length of the channel.

3.5.2 Maximal Exchange Flow Through A Wide Culvert

Given the assumption of horizontal free surface or rigid lid approximation, the analysis of the two-layer exchange through a wide channel presented in the previous section applies equally to exchange flows beneath a frictionless rigid lid. In reality, however, such a rigid lid is usually frictional, except for the case of a very short channel, where the frictional effects are negligible. The two-layer exchange flow under a frictional rigid-lid constitutes the exchange flow through a culvert, which always flows full or is under surcharged condition.

Assuming that the culvert is wide (i.e. $H \ll b$) and the surface and bottom frictional factors are the same (i.e. $f_s = f_b$) the frictional slope, as defined by (3-9), then reduces to $S_f = \frac{1}{2} f_I F_\Delta^2 \frac{H^2}{y_1 y_2} + \frac{1}{2} f_b \left(F_2^2 + F_1^2\right)$ in dimensional form. Substituting non-dimensional variables defined in Equations (3-25) to (3-32) and dropping the superscript, *, lead to the following non-dimensional equation of motion for two-layer culvert exchange flows:

$$\frac{dy_2}{d\chi} = \frac{\alpha G_o^2 (f_r + y_1^3 + y_2^3)}{32 y_1^3 y_2^3 - 2G_o^2 (y_1^3 + y_2^3)}. \tag{3-41}$$

Again, For the reason of simplicity, it will be assumed, in the following derivation, that the interfacial frictional coefficient f_I is the same as the bottom frictional coefficient f_b, i.e. $f_r = 1$. Please refer to section A.2 of Appendix A for more general solutions to the culvert exchange problem.

Re-arranging terms in (3-41) and applying integration to both sides of equation lead to:

$$\int \alpha G_o^2 d\chi = \int \frac{32 y_1^2 y_2^3 - 2G_o^2 \left(y_1^3 + y_2^3\right)}{\left(y_1^3 + y_2^3 + 1\right)} dy_2 = \sum_{i=1}^{4} \phi_i, \tag{3-42}$$

where $\phi_1 = -2\left[G_o^2 + \frac{64}{27}\right] \int dy_2$

$$\phi_2 = -\frac{64}{9}\int (y_1 y_2) dy_2 = -\frac{64}{9}\int (1-y_2) y_2 dy_2 ,$$

$$\phi_3 = -\frac{32}{3}\int (y_1 y_2)^2 dy_2 = -\frac{32}{3}\int (1-y_2)^2 y_2^2 dy_2 ,$$

$$\phi_4 = 2\left[G_o^2 + \frac{128}{27}\right]\int \frac{1}{-3y_1 y_2 + 2} dy_2 = 2\left[G_o^2 + \frac{128}{27}\right]\int \frac{1}{-3(1-y_2)y_2 + 2} dy_2 .$$

Integrating (3-42) and substituting $y_2 = \frac{1}{2} + \eta$ into the resulting equation then lead to the direct integration of the equation of motion for two-layer culvert exchange flows. The solution can be re-arranged in the form of density interface profile equation as following:

$$\alpha G_o^2 \chi = a_1 \eta + a_2 \eta^3 + a_3 \eta^5 + a_4 \tan^{-1}\left[\frac{6\eta}{\sqrt{15}}\right] + a_o, \qquad (3\text{-}43)$$

where $a_1 = -\frac{2}{27}[27 G_o^2 + 97]$,

$a_2 = \frac{112}{27}$,

$a_3 = -\frac{32}{15}$,

$a_4 = \frac{4[G_o^2 + 128/27]}{\sqrt{15}}$,

a_o is the constant of integration.

The constant of integration a_o can be readily solved using the symmetric nature of the culvert exchange flow (i.e. $\eta_\chi = -\eta_{1-\chi}$ or $\eta_{\chi=0.5} = 0$). Substituting $\eta = 0$ at $\chi = 0.5$ into the interface profile equation of (3-43) and solving for the constant of integration a_o yields:

$$a_o = \tfrac{1}{2}\alpha G_o^2 . \qquad (3\text{-}44)$$

Similar to open channel exchange flow problems, two solution curves can be defined from the direct integration of (3-43). Substituting $\chi = 0$ and $\eta = \eta_o$ into the interface profile

equation of (3-43) and rearranging terms lead to the solution curve at $\chi = 0$, i.e. $f_o\left(G_o^2, \eta_o, \alpha, f_r\right)$:

$$G_o^2 = \frac{\frac{194}{27}\eta_o - \frac{112}{27}\eta_o^3 + \frac{32}{15}\eta_o^5 - \frac{512}{27\sqrt{15}}\tan^{-1}\left[\frac{6\eta_o}{\sqrt{15}}\right]}{\frac{\alpha}{2} - 2\eta_o + \frac{4}{\sqrt{15}}\tan^{-1}\left[\frac{6\eta_o}{\sqrt{15}}\right]}. \qquad (3\text{-}45a)$$

Similarly, substituting $\chi = 1$ and $\eta = \eta_1$ into the interface profile equation of (3-43) and rearranging terms lead to the solution curve at $\chi = 1$, i.e. $f_1\left(G_o^2, \eta_1, \alpha, f_r\right)$:

$$G_o^2 = \frac{-\frac{194}{27}\eta_1 + \frac{112}{27}\eta_1^3 - \frac{32}{15}\eta_1^5 + \frac{512}{27\sqrt{15}}\tan^{-1}\left[\frac{6\eta_1}{\sqrt{15}}\right]}{\frac{\alpha}{2} + 2\eta_1 - \frac{4}{\sqrt{15}}\tan^{-1}\left[\frac{6\eta_1}{\sqrt{15}}\right]}, \qquad (3\text{-}45b)$$

where $f_r = 1$ is assumed in both solution curves for the reason of simplicity here.

3.5.3 Presentation of Maximal Exchange Flow Solutions on the $G_o^2 - \eta$ Plane

The $G_o^2 - \eta$ plane was used in this study to define the unique discharge (G_o^2) – depth (η) relationship for maximal two-layer exchange flows at both ends of the channel. It not only serves to present the maximal two-layer exchange flow solutions, but, most importantly, also provides a graphical way to solve for problem. In addition, the variables G_o^2 and η are used extensively in the theoretical formulation and derivation of maximal exchange flow solution. Other ways of graphically presenting the two-layer flows have also been used by other authors. For example, Lawrence (1993) presented the two-layer flow over a fixed obstacle in the $E - \eta$ plane, and Armi (1986) presented the two-layer maximal exchange flow on the Froude number (F_1^2 and F_1^2) plane.

The presentation of solutions to the maximal two-layer exchange flow problems in the $G_o^2 - \eta$ plane is shown in Figure 3-6a. In the $G_o^2 - \eta$ plane, the hydraulic critical flow

condition (i.e. $G^2 = 1$) is shown as a symmetrical bell-shaped curve separating the supercritical and subcritical flow regimes. The area within the curve represents subcritical flow regime (i.e. $G^2 < 1$), while the area outside the curve characterises supercritical flow regime (i.e. $G^2 > 1$). The two solution curves, f_o and f_1, are shown as upper and lower splitting limbs respectively in the $G_o^2 - \eta$ plane. The solutions to maximal exchange flows are characterised by the intersections or solutions points of the critical condition curve and two solution curves on the $G_o^2 - \eta$ plane.

For steady densimetric exchange flows, the flow rate does not vary along the channel, i.e. $q_1 = q_2 = q$. Therefore, under any given frictional parameters α and f_r, there is only one possible maximal exchange rate solution. This is expressed, in the non-dimensional form in the $G_o^2 - \eta$ plane as the horizontal coordination of the solution points. The vertical coordinations of the two solution points on the η axis are interface deflections at both ends of the channel, η_o and η_1, respectively. By definition $\eta_o \le \eta_1$, as the more dense lower layer fluid flows from right to left while the less dense upper layer fluid flows from left to right. Obviously, the horizontal distance between the two solution points is the total non-dimensional interface deflection, $\beta = d/H = \eta_1 - \eta_0$, through the channel, where d is the dimensional interface deflection and H is the total fluid depth.

Some solutions to the maximal densimetric two-layer exchange flows are demonstrated by a series of solution curves with different frictional parameters. The frictional ratio f_r is fixed at unity, while the frictional parameter α is varied from between 0.01 and 10 to represent different relative dynamic channel length. Obviously, increasing friction (i.e. larger α value) would increase the overall interface slope (i.e. larger interface deflection β) and reduce the exchange flow rate (i.e. smaller G_o^2 value). The presentation of solutions in the $G_o^2 - \eta$ plane also confirms the fundamental requirement for maximal two-layer exchange that hydraulic controls must occur at both ends of the channel, as the solution points always coincide with

the maximum points (i.e. where $\partial G_o^2/\partial \eta_0 = 0$ and $\partial G_o^2/\partial \eta_1 = 0$) on both solution curves for given frictional parameter α.

For maximal exchange flow with $f_r = 1$, variations of some important parameters along the channel are shown in Figures 3-6b, c and d. The variation of the density interface along the channel is roughly linear for most part of the channel and curved near each end, as shown is in Figure 3-6b. Points *a* and *b* correspond to locations shown in Figure 3-6a. The exchange through the channel is bounded by two hydraulic controls at each end, as indicated by the variations of the composite and internal Froude numbers, G^2 and F_I shown in Figure 3-6c. It is worth of noting that the internal Froude number F_I has opposite signs at each end due to the directional change of the convective velocity u_c. The convective velocity is negative ($u_c = -c$) at the left end ($\chi = 0$) and positive ($u_c = c$) at the right end ($\chi = 1$), where c is the phase speed of infinitesimal long internal wave. Hence the influence of both reservoirs in the form of propagating internal waves is isolated by the presence of hydraulic controls at each end of the channel. The internal energy E varies more or less linearly along the channel, as shown in Figure 3-6d.

In the absence of friction (i.e. $\alpha = 0$ and $f_r = 0$), two solution points would coalesce at $G_o^2 = 1$ and $\eta = 0$ on the $G_o^2 - \eta$ plane, i.e.:

$$\eta = 0, \qquad \text{for } 0 \le \chi \le 1, \quad \text{(3-46a)}$$

$$G^2 = \frac{G_o^2}{16(\frac{1}{2} - \eta)^3} + \frac{G_o^2}{16(\frac{1}{2} + \eta)^3} = G_o^2 = 1, \quad \text{for } 0 \le \chi \le 1, \quad \text{(3-46b)}$$

and

$$E = \frac{1}{2} + \eta + \frac{G_o^2}{32}\left(\frac{1}{(\frac{1}{2} + \eta)^2} - \frac{1}{(\frac{1}{2} - \eta)^2}\right) = \frac{1}{2}, \qquad \text{for } 0 \le \chi \le 1. \quad \text{(3-46c)}$$

The upper and lower layers are of equal thickness and the flow is critical throughout the channel, which essentially acts as a contraction between two reservoirs. In the absence of

friction, the internal energy E also remains constant. This flow condition essentially represents the solution of lock-exchange problem of Wood (1970).

For exchange flows through extremely long channels (i.e. $\alpha \to \infty$), the two solution curves are increasingly flattened on the $G_o^2 - \eta$ plane. This leads to:

$$\eta \to -0.5 \text{ at } \chi = 0 \text{ and } \eta \to 0.5 \text{ at } \chi = 1, \tag{3-47a}$$

$$G_o^2 \to 0, \tag{3-47b}$$

and

$$E \to 0 \text{ at } \chi = 0 \text{ and } E \to 1 \text{ at } \chi = 1. \tag{3-47c}$$

Under this condition, the two-layer exchange flow rate becomes vanishingly small and the upper and lower layer thickness becomes infinitely thin at right and left ends of the channel respectively.

Within the subcritical flow region on the $G_o^2 - \eta$ plane, i.e. within the $G^2 = 1$ curve, the points on solution curves f_o and f_1 represent the uncontrolled and thus submaximal exchange flow conditions. The submaximal flow conditions resemble the exchange between reservoirs with two-layer density structures. The interface heights in the reservoirs are such that the hydraulic controls are lost, and exchange flows are hence subject to the influence of both reservoirs. Due to the symmetrical nature of the two solution curves, these submaximal exchange solutions are only valid for the very special case of $-\eta_0 = \eta_1$, i.e. the lower layer depth in the left reservoir is equal to the upper layer depth in the right reservoir. Finally, within the supercritical flow region on the $G_o^2 - \eta$ plane, i.e. outside the $G^2 = 1$ curve, the points on solution curves representing supercritical flow conditions at channel ends. This would imply an increasing internal energy and negative interface slope, and hence is not physically possible.

The presentation of maximal exchange flow solutions on the $G_o^2 - \eta$ plane is very informative for boundary value problems. It also provides a simple intuitive approach to solve the exchange flow problems graphically. Alternatively, the maximal exchange flow problems can be solved in an iterative manner. The numerical procedure used to solve for the maximal exchange flow solutions is described in detail in Appendix B. The iteration procedure is shown schematically on the $G_o^2 - \eta$ plane in Figure 3-7.

After solving G_o^2 for given values of α and f_r, the maximal exchange flow solutions can also be graphically represented on the $E - \eta$ plane as well as on the Froude number plane. Rewriting the internal energy equation (3-4) in non-dimensional form for $q_r = 1$ yields:

$$E = \frac{1}{2} + \eta + \frac{G_o^2}{32}\left(\frac{1}{(\frac{1}{2}+\eta)^2} - \frac{1}{(\frac{1}{2}-\eta)^2}\right). \tag{3-4}$$

Contours of constant G_o^2 are plotted on the $E - \eta$ plane in Figure 3-8a.

Alternatively, the maximal exchange flow solutions could be represented on the Froude-number ($F_1^2 - F_2^2$) plane as proposed by Armi (1986). Expressing the non-dimensional layer thickness for $q_r = 1$ as:

$$y_1 = \left(\frac{G_o^2}{16F_1^2}\right)^{\frac{1}{3}} \text{ and } y_2 = \left(\frac{G_o^2}{16F_2^2}\right)^{\frac{1}{3}}. \tag{3-48}$$

Combining (3-48) with the rigid-lid approximation ($y_1 + y_2 = 1$) leads to:

$$F_1^{-\frac{2}{3}} + F_2^{-\frac{2}{3}} = \left(\frac{G_o^2}{16}\right)^{-\frac{1}{3}}. \tag{3-49}$$

Contours of constant G_o^2 are plotted on the Froude-number plane in Figure 3-8b, where the critical condition, as represented by $G^2 = F_1^2 + F_2^2 = 1$, falls to a straight line separating supercritical and subcritical flows.

On both $E-\eta$ and $F_1^2-F_2^2$ planes, each contour of constant G_o^2 typically has two intersections with $G^2=1$. These two intersections depict the critical flow conditions at either end of the channel. The variation of subcritical exchange flow conditions within the channel is represented by contours of constant G_o^2 between the two intersections. Given $\alpha=0.1$ and $f_r=1$, for example, intersections a and b represent critical conditions of two control locations at each end of the channel, as shown in Figure 3-6b. In the absence of friction (i.e. $\alpha=0$), the two intersections coalesce to a single point c, which resembles the flow conditions as defined by (3-46). With increasing frictional effects, the contours of constant G_o^2 approach the asymptote, $\eta=E$, on the $E-\eta$ plane and on the Froude number plane F_1^2 and F_2^2 approach unity at right and left ends of the channel respectively. For exchange flows through very long channels (i.e. $\alpha\to\infty$), the flow conditions as defined by (3-47) are achieved.

CHAPTER 4

EXPERIMENTAL APPARATUS AND TECHNIQUES

The laboratory experiments were conducted at the hydraulics laboratory of the University of British Columbia. The experimental tank was previously used to study exchange flows through a straight channel with an underwater sill (Zhu & Lawrence, 2000). Some modifications, however, were made to make it better suit the purpose of this study. This chapter describes the laboratory apparatus, instrumentation, data acquisition and processing used in this study. Finally, the field investigation during the summer of 1996 in the Burlington Ship Canal is also briefly described.

4.1 LABORATORY EXPERIMENT SET-UP

An overall view of the experimental set-up is shown in Figure 4-1. The primary components of the laboratory apparatus include the experimental tank, a laser generator as well as scanning and reflecting mirrors for flow visualisation purpose, video capturing devices for imagine recording, an automated traversing device for instrument mounting, and a pump for generating the desired barotropic flow.

Experiments were conducted in a 370 cm long and 106 cm wide tank designed as a general exchange flow experimental facility. The tank is divided into two reservoirs connected by a straight channel 200 cm long, 15.2 cm wide and 30 cm deep with zero bottom slope. The front panel of the channel is made of plexi-glass enabling observation of the flow. The desired densimentric driving force for exchange flow is obtained by dissolving salt in the

reservoirs. The water in the right reservoir is made slightly heavier, so that the upper layer flows from left to right, while the lower layer flows from right to left. To maximise the maximal exchange flow period, the tank is designed in such a way that the right reservoir is larger and shallower, while the left reservoir is smaller and deeper. The volumes of two reservoirs, however, are approximately the same.

A light sheet is used to illuminate in a vertical plane along the longitudinal centreline of the straight channel. This is accommodated by a 4-W argon-ion laser generator (model Stabilite 2017 by Spectra-Physics). The laser beam from the laser generator is split into a light sheet by a scanning mirror and then reflected by a large reflecting mirror into the channel, as shown in Figure 4-2. The oscillating frequency of the scanning mirror is set at about 300 Hz. This frequency is sufficiently higher than the typical video camera shutter frequency of 30 Hz.

Two video cameras were used simultaneously during the experiment. The first camera, a high signal to noise ratio CCD camera with a 1:2.5/18-108 mm zoom lens (model Cohu by Fuji), was used to capture the particle image used for mean velocity measurements. This particle image was recorded in Hi 8 mm format. While the second camera, a Super VHS video camera, was used to capture and record the density interface position along the channel.

An instrument mounting device was installed on an automated traversing mechanism to make vertical density profile measurements. The traversing mechanism was driven by a stepping motor and controlled by a personal computer. A limiting switch was installed to prevent the costly event of driving the probe into the bottom of the channel.

The pump used is a Masterflex I/P with two Masterflex 7529 pump heads. It gives a maximum pumping capacity of 430 cm^3/s with the Masterflex #2 hoses. During the experiment, heavier water was selectively withdrawn from the bottom of the right reservoir

to the deep basin in the left reservoir through a diffuser. This provides a net barotropic flow in the channel flowing in the upper layer from left to right.

4.2 LABORATORY MEASUREMENT TECHNIQUES

Simultaneous laboratory measurements include photographic observation of density interface positions by video and still cameras, density profiling by a conductivity probe, and mean velocity measurements using Particle Image Velocimetry (PIV) technique. An Acoustic Dopller Velocimeter (ADV) was also used to make point turbulent measurements in separate experiments.

4.2.1 Conductivity Probe and Density Profiling

Density profiles at certain desired locations were obtained using a conductivity probe. The conductivity probe used was a PME (Precision Measurement Engineering) model 125 micro-scale four wire glass conductivity and temperature probe. The conductivity probe is designed for use in salt stratified flows where high spatial resolution, fast response time and minimal flow disturbances are desired (Head, 1983).

The conductivity probe will not measure the density directly, it rather measures the conductivity of the salt solution provided the calibration is done properly. Sodium chloride (NaCl) was used in the experiments to generate the desired density difference between two layers of fluid. The density calculation of the NaCl solution requires a relationship between the conductivity and the density as a function of the temperature. Although this kind of relationship is well-known for seawater (see, for example, "Standard Methods for Examination of Water and Wastewater", 18th Edition, 1992), unfortunately such a relationship is less well established for NaCl solutions.

For NaCl solutions used, the relationship between the density and the conductivity as a function of the temperature, i.e. $\rho = f(\sigma, \Theta)$, was established by the direct calibration method (Head, 1983), where ρ, σ and Θ are the density, the conductivity and the temperature respectively. The direct calibration was carried out by exposing the conductivity probe to many salt solution samples of known density ρ_{sample} and sample bath temperature Θ_{sample}. The conductivity probe itself was calibrated using the standard Potassium Chloride (KCl) solution at a reference temperature Θ_{ref} of $25.0^{o}C$. KCl is considered the standard salt used in the calibration of conductivity cells, due to its high purity and well established relationship between the conductivity and the solution concentration. Once the probe is properly calibrated, the conductivity for each sample solution σ_{sample} was measured. This establishes a set of $\rho_{sample} = f(\sigma_{sample}, \Theta_{sample})$ curves, as shown in Figure 4-3. It is noted that, within the calibration range, the conductivity is more or less linear with the density.

Knowledge of the temperature of the fluid in the experimental flow allowed the density to be calculated from the conductivity. For temperatures of the fluid in the experiment Θ_{exp} other than Θ_{sample}, the conductivity σ_{exp} was obtained by linear interpolation of nearest two curves. The fluids used were allowed to sit at room temperature for several hours before each experiment. Therefore, the experimental fluids were sufficiently homogeneous so that temperature profiling was not necessary. Only the bulk temperature measurement of fluid was used.

The entire profiling and sampling process was automated by a personal computer. The conductivity probe was mounted on a vertically traversing mechanism driven by a step motor, as shown in Figure 4-4. During a typical experiment, the conductivity was sampled at a frequency of about 10 Hz and the probe was traversed at a typical speed of 0.5 cm/s. This represents a spatial resolution of 0.5 mm in vertical direction. The output signal from the conductivity probe ranges from –5.0 to +5.0 volts. This was then digitised into 12 bits by an A/D board (DAS 8), implying a minimum resolution of 2.4×10^{-3} volts. The probe tends to

entrain a thin, viscous layer of denser fluid along the small probe tip when it is pulled up, signified by its delayed response in the probe output. Therefore the signals from the probe were only recorded on downward traverses. To avoid the interference with the laser sheet, the probe was placed slightly off the longitudinal centreline.

4.2.2 Image Analysis and Density Interface Positions

Laser Induced Florescence was used to visualize the flow, namely the interface positions along the channel and the interface deformation caused by instabilities. The density interface of two layer exchange flow was visualised by dissolving dye in the lower layer and illuminating it in a vertical plane along the longitudinal centreline of the channel by a laser beam. The interface images were captured and recorded using a Super-VHS video camera. The recorded video images were then grabbed at certain time intervals using the IMAGE 1.50 (National Institute of Health) via a video frame grabber board (QuickCapture model DT 2255 by Data Translation). The grabbed images were processed to determine the position of the density interface, defined as the location of maximum vertical gradient of light intensity.

Selecting the appropriate dye and using the right dye concentration are crucial to the success of the technique. Either sodium fluorocein (green in color) or Rhodamine WT dye (orange in color) were used. Although sodium fluorocein is generally more fluorescent than Rhodamine WT, its similarity in colour with laser light makes particle image in the lower layer hardly visible. The particles served as tracers in the Particle Image Velocimetry technique discussed in the next section. Therefore Rhodamine WT dye was used in the majority of experiments in which both interface positions and velocity profiles were measured simultaneously. While the use of the fluorocein dye was limited to those experiments where only the density interface was visualized. The optimal concentration of the dye was determined through a trial and error process. The quality of video images was further improved using appropriate optical filters.

4.2.3 Particle Image Velocimetry (PIV)

The average velocity profiles and exchange flow rates were obtained using high density PIV technique. The essence of the technique is the spatial cross-correlation between successive images of known intervals. A sampling window in which there are many particles is chosen in the first image. In the second image, region around the sampling window is searched and a target widow with the maximum cross-correlation function is the presumed displaced location of the original window. The principle of the technique is demonstrated schematically in Figure 4-5. The particle images at certain channel sections were captured using a CCD video camera and recorded in Hi 8 mm format. Video images pairs were then grabbed at the required time intervals and processed using the algorithm by Stevens & Coates (1994).

Particle seeding is crucial to the success of the technique. The Pliolite VT-L particle (by Goodyear Chemical Co.) was chosen as the tracing material because of its near neutral buoyancy and high reflectivity. The particles are insoluble in water and can be easily ground to the desired size. Appropriate particle sizing is also important. The scattered light of the particle image was viewed perpendicular to the laser sheet. The scattering intensity for scattering angles of 90^{o} is small. This requires larger particles for stronger video signal. On the other hand, larger particle size means smaller drag to inertial ratio (i.e. slower response) and larger settling velocity. Based on above considerations, particles with size ranging from 100 μ m to 225 μ m were chosen by trial and error process. Using a similar range of particle sizes, the technique has been successful in previous exchange flow studies (e.g. Zhu, 1996).

The particle image velocimetry technique used has certain limitations. The technique follows the movement of sampling windows rather than individual particles. Stevens & Coates (1994) suggested that the window dimension needs to be smaller than 1/5 of the smallest length scale in order to resolve that scale. This implies that it will not resolve

turbulent velocities to any significant scales. Moreover, the technique assumes no fluid deformation within the sampling window. This may not be true in interfacial shear region where significant rotation and strain may occur.

4.2.4 Acoustic Doppler Velocimeter (ADV)

An ADV probe by Sontek was used to make point velocity measurements (Kraus *et al*, 1994). The probe consists of three receivers and one transmitter. The transmitter is circled by three receivers positioned in 120° increments. The receivers are slanted at 30° from the axis of the transmitter and focused on a common sampling volume located about 5 cm below the probe. The system operates by transmitting short acoustic pulses by the transmitter. As the pulses propagate through the water, a fraction of the acoustic energy is scattered back by small particles suspended in the water and detected by the three receivers. The Doppler shift of the echoes observed at each receiver is proportional to the component of the flow velocity along the bisector of receiver and transmitter beams. The 3-dimensional velocity can be measured at a frequency of 25 Hz in a sampling volume of less than 1 cm^3.

Particle seeding is essential, as ADV does not measure the fluid velocity directly. The seeding material used are hollow glass spheres that are very close to neutrally buoyant and have a typical diameter of 8-10 μm. A concentration of 10-50 mg/L of the seeding material will provide sufficient echo strength to electronic noise ratio.

4.3 LABORATORY EXPERIMENTAL PROCEDURES

The experiments were prepared and performed in three stages: preparation of the tank and desired stratification, adjustment and calibration of instruments, and finally carrying out experiment itself.

First the experiment tank is filled with water to a specified depth through a hot/cold water mixer. During the filling process, the water temperature is carefully adjusted to approximately room temperature and is closely monitored. The tank then is allowed to sit for some time so that water in the tank reaches room temperature. The removable barrier is installed in the channel to separate the tank into two reservoirs. Specific amounts of NaCl are added into both reservoirs to generate the driving buoyant force. To ensure that the conductivity is within the linear range of the conductivity probe (5,000 to 800,000 $\mu S/cm$), a minimum salt concentration of about 3.2% is always required in the left reservoir.

Selected dye was dissolved into the right reservoir. Pliolite particles were added and mixed into both reservoirs. The water was then stirred thoroughly to ensure it was well mixed. The concentration of both dye and tracer particles were determined by trial and error during the preliminary experiments.

Secondly the conductivity probe was calibrated. The calibration of the probe was performed in two steps: set-up for proper conductivity gain and calibration of data acquisition. To ensure the instrument does not go beyond range of +5.0 volts, the conductivity gain was adjusted by exposing the probe to fluid in the right reservoir where the highest conductivity is expected. The probe was then calibrated against the standard KCl solution of known conductivity. The KCl solution or reagent was prepared using a class A volumetric flask and a Sartorius analytic balance, accurate to ± 0.001 grams. The KCl salt was dried by baking at $400^{o}C$ for at least 4 hours before use. The conductivity for several concentrations of KCl at $25.0^{o}C$ are listed in Table 4-1. Within parameter range of experiments, KCl solutions with concentration of either 0.05 or 0.1 M were prepared.

Table 4-1. Conductivity of KCl at $25.0^{o}C$ (Adapted from Table 2510:I of "Standard Methods for Examination of Water and Wastewater", 18th Edition, 1992)

KCl Concentration (M)	Conductivity ($\mu S/cm$)
0.05	6,667
0.1	12,890
0.2	24,800
0.5	58,670
1	111,900

At temperature other than $25.0^{o}C$, the following formula,

$$\sigma_{\Theta_{sample}} = \left[1 + 0.019\left(\Theta_{sample} - 25\right)\right]\sigma_{\Theta_{ref}}, \qquad (4\text{-}1)$$

was used for conversion of conductivity. Where in (4-1) $\sigma_{\Theta_{ref}}$ is the conductivity at the reference temperature of $25.0^{o}C$ and $\sigma_{\Theta_{sample}}$ is the conductivity measured at the sample temperature Θ_{sample}. Strictly speaking, conductivity does not vary linearly with temperature. Therefore, a temperature range of 23 to 27°C is recommended when apply (4-1) (see Standard Methods for Examination of Water and Wastewater", 18th Edition, 1992).

After the calibration, the power to the probe was kept on and the probe was kept submerged in the water to minimize drift. The probe has a 8-hour calibration stability rating of better than 1% of the conductivity reading. The laser optical set up and video recording equipment were carefully adjusted. The physical scales were then recorded, the temperature was measured, and the protective cap of conductivity probe was carefully removed. Finally, after the water became quiescent, the experiment was started by removing the barrier and allowing fluids from two reservoirs to exchange. The repetitive density profiling routine, the video recording, and the pump operation (if required) were all started simultaneously.

Upon removal of the gate, the uncontrolled exchange flow developed during the initial start-up period, and gradually the hydraulic controls were established at each end of the channel (Figure 4-6). The initial start-up period was marked by substantial mixing between two layers of fluid. The mixed fluid was progressively swept or advected into two reservoirs. The duration of initial stage is in the order of $L/\sqrt{g'H}$ with g' being the reduced gravity, L and H being the length and total depth of the fluid respectively. The term $\sqrt{g'H}$ is the speed by which internal disturbances propagate in the form of infinitesimal internal long waves. Within parameter range of laboratory experiments in this study, this period was estimated between 30 ~ 100 seconds. Refer to Zhu & Lawrence (2000) for more detailed description on flow evolution during the initial start-up period.

Each experiment typically lasted about 10 minutes, with only a few minutes of video and conductivity data being processed to study the steady maximum two-layer exchange flows.

4.4 ERROR ANALYSIS

Both velocity profile and interface position measurements are subject to measurement errors mainly due to the resolution of the video images. The particle images used for calculating velocity profiles have the resolution of 640 by 480 pixels. The time interval between the two successive particle images was chosen such that particles had an average displacement of about 20 pixels. Considering a measurement error of ± 0.5 pixel in determining the particle displacement, an average relative error of about 3% in velocity calculation is possible. Other minor sources of error may include possibly slight unsteadiness, the three-dimensionality, and the fluctuation of interface position. These minor errors were reduced by averaging several velocity profiles obtained from different pairs of images. Since the exchange flow rates were calculated by integrating the velocity profiles at the center of the channel, hence the exchange flow rate measurements were subject to the same sources of error as the

velocity profile calculations. An additional source of error is the development boundary layers on the sidewalls of the channel. This could introduce another 1~2% error into the flow rate calculations. Hence, an overall error in the order of 5% is likely in the exchange flow rate measurements.

The density interface positions throughout the channel were determined from video images covering an area of 200 cm in horizontal and 150 cm in vertical. Given the video image size of 640 by 480 pixels, the overall image resolution would be about 0.3 cm per pixel in both vertical and horizontal directions. Considering a measurement error of 1~2 pixels in determining the interface positions, a relative error of 2% is possible for a total fluid depth of 28 cm. Additional sources of error include optical distortion of video images and interface fluctuations due to wave activities. The errors due to interface fluctuations were reduced through temporal averaging of many images. Assuming the additional measurement error of about 1%, the overall error in determining the interface positions could be in the order of 3%.

4.5 FIELD EXPERIMENTS

The field experiments were conducted at the Burlington Ship Canal in July and August of 1996. A large array of instrumentation was deployed in and around the ship canal, as shown in schematically Figure 4-7. These instruments include temperature, conductivity, and pressure sensors, gas purging water level meters, current meters, as well as several meteorological stations.

77 temperature and 9 conductivity loggers were arranged in 8 thermistor chains at locations designated as TChains in Figure 4-7a. 4 thermistor chains were installed within the ship canal, at locations shown in Figure 4-7b. The temperature and conductivity data was acquired at a frequency of 20 Hz, and stored by an in-situ data logger. From the temperature

and conductivity data the vertical temperature (density) structure of exchange flows could be evaluated.

Two bottom mounted Acoustic Doppler Current Profiles (ADCP's) were installed near each end of the ship canal, designated as ADCP in Figure 4-7b. The ADCP took vertical velocity profiles at a frequency of 0.08 Hz with a bin depth of 0.25 m. The signal from the ADCP near the Hamilton Harbour end was monitored by a computer located in an on shore trailer. The velocity profiles were integrated over the depth to estimate the exchange flow rates through the ship canal.

Additional data was also collected by instrumentation mounted on a small boat. The boat was equipped with a Differential Global Positioning System (DGPS), a 1200 kHz broadband ADCP, a conductivity-temperature-depth fine scale probe (OS200 CTD) and a temperature-dissolved oxygen-depth probe (Hydrolab). The ADCP was mounted on the side of the boat, while OS200 or Hydrolab was yo-yoed from the boat during each experiment. The boat instrumentation and survey methodology are described in detail in Greco (1998).

CHAPTER 5

RESULTS AND DISCUSSION

5.1 COMPARIONS WITH LABORATORY EXPERIMENTS

A total of eight laboratory experiments on densimentric exchange flows were conducted. These are listed in Table 5-1, in which g' is the reduced gravity; q is the measured exchange flow rate per unit channel width, and $G_o^2 = 16q^2/g'H^3$ is the composite Froude number throughout the channel in the absence of friction. Throughout the laboratory experiments, the channel dimensions (i.e. channel length L and channel width b) and total fluid depth H were kept constant ($L = 200.0$ cm, $b = 15.2$ cm, and $H = 28.0$ cm), while the reduced gravity g' was varied between $0.27 \sim 1.83$ cm/s^2 to provide the desired range of flow parameters. Some experiment runs were repeated several times, as indicated in the most right column of Table 5-1. These repeating experiments served to accommodate flow visualization and/or point velocity measurements using an ADV probe.

Governing parameters are listed as the stability Froude number $F_\Delta^2 = \Delta U^2/g'H$, the channel Reynolds number $\mathrm{Re} = \Delta UH/\nu$, and the Keulegan number $K = \mathrm{Re}\,F_\Delta^2 = \Delta U^3/\nu g'$, where ΔU is the velocity shear measured at the center of the channel (i.e. at $x/L = 0.5$). Since the velocity shear changes throughout the channel, the governing parameters listed do vary slightly throughout the channel from their values at the center of the channel. $\alpha = \bar{f}_b L/H$ is the frictional parameter defining the dynamic strait length, $\bar{f}_b$ and $\bar{f}_i$ are the mean bottom and interfacial friction coefficients averaged over the whole length of the channel.

Table 5-1. List of laboratory experiments.

Experiment Runs	g' (cm/s^2)	q (cm^2/s)	G_o^2	F_Δ^2 ($x = 0.5L$)	Re ($x = 0.5L$)	K ($x = 0.5L$)	α	$\bar{f}_I$	Number of Replications
E1	0.27	14.28	0.55	0.55	5,684	1,721	0.094	0.0037	-
E2	0.49	20.20	0.61	0.61	7,961	2,993	0.091	0.0031	5
E3	0.72	23.96	0.58	0.58	9,538	3,221	0.083	0.0032	-
E4	0.95	28.53	0.62	0.62	11,333	4,420	0.077	0.0038	2
E5	1.14	30.90	0.61	0.61	12,242	4,562	0.074	0.0039	16
E6	1.33	32.40	0.57	0.58	12,836	4,248	0.068	0.0041	2
E7	1.61	36.45	0.60	0.60	14,326	5,181	0.059	0.0036	-
E8	1.83	39.37	0.62	0.62	15,395	5,869	0.051	0.0037	-

The channel Reynolds number *Re*, given in Table 5-1, indicates that the flow should well be in the turbulent range given the critical Reynold numbers for open channel flows, which are in the range of 500 to 2500 (Chow, 1959). Similarly, the Keulegan number K is significantly higher than its critical values, which is in the range from 180 (Turner, 1973) to 350 (Browand & Winant, 1973), hence indicating an unstable density interface.

5.1.1 Laboratory Measurements

During the laboratory experiments, information on velocity fields and interface positions was obtained using various flow visualization, particle tracking, and image processing techniques, while the density profiles were measured using a conductivity probe.

Typical mean velocity and density profiles measured at the centre of the channel ($x = 0.5L$) are shown in Figures 5-1a and 5-1b respectively for E5. Both profiles were obtained through some post-processing procedures. These post-processing procedures are essential, as individual measurement was always influenced by three-dimensional turbulent fluctuations as well as internal wave activities. The mean velocity profile obtained by the PIV technique

was post-processed to remove spurious velocity vectors. The post-process involves eliminating the erroneous vectors and averaging velocities over a pre-specified averaging grid (Stevens & Coates, 1994). Also shown in Figure 5-1a are point velocity measurements by an ADV probe. The density profile was obtained by traversing a conductivity probe. The individual density profiles all exhibit very sharp interfaces with occasional wave breaking events shown as profile instabilities. The density profile shown in Figure 5-1b was obtained by averaging 10 descending profile measurements.

The point velocity measurements by the ADV were used to validate the PIV technique. The ADV operates by sending a series of acoustic pulses and listening to the reflections of these pulses from the water. If the ADV is operating close to the boundary, it is possible that the reflection from the boundary of an early pulse could interfere with the measurement of a later pulse, as indicated in the ADV users manual by SonTek. The boundary interference is quite possible due to the relatively small scale of the channel. Each time when the ADV is re-started or initialized, it automatically searches for boundaries and checks if there is a possibility of interference. If so, the system adjusts operating parameters to avoid such interference. Once the probe is initialized, it should not be moved during the experiment. Therefore, each ADV measurement point in Figure 5-1a essentially represents a separate experimental run, which was repeated 14 times for E5. The velocity profile obtained by the PIV technique matches very well with the ADV measurements, as shown in Figure 5-1a. Such detailed ADV measurements were only carried out in E5. For other experiments, the velocity profile measurements were solely based on the PIV technique described in detail in Chapter 4.

The measured velocity and density profiles are reasonably uniform except in the interfacial region where large gradients exist. The interface position can be specified from either the velocity profiles or the density profiles in the following three ways (also shown schematically in Figure 5-2):

• from the position of maximal velocity shear, i.e. where the velocity gradient, (du/dy), is at its maximum value from the velocity profile,

• from the zero velocity line, determined by the reversal point in the velocity profile, and

• from the position of maximal density gradient, i.e. where $(d\rho/dy)$ is at its maximum value from the density profile.

In perfect two-layer flows, as defined in the two-layer internal hydraulic theory, the interface divides the lighter, rightward moving upper layer and denser, leftward moving lower layer. Hence, the above three interfaces should be completely identical, as show in Figure 3-3.

The velocity interface thickness or shear layer thickness, δ, defines the region where the horizontal velocity varies rapidly between the nearly uniform layer velocities, U_1 and U_2. The shear layer thickness is defined as:

$$\delta = \Delta U / (\partial u/\partial y)_{\max}, \tag{5-1}$$

where $\Delta U = |U_1 - U_2|$ is the horizontal velocity difference between the two layers, and $(\partial u/\partial y)_{\max}$ is the maximum slope of the velocity profile.

The density interface thickness, ς, is defined, similar to the shear layer thickness δ, as,

$$\varsigma = \Delta\rho / (d\rho/dy)_{\max}, \tag{5-2}$$

where $\Delta\rho = \rho_2 - \rho_1$ is the density difference between the two layers, and $(\partial\rho/\partial y)_{\max}$ is the maximum slope of the density profile.

The measured velocity profile for E5, as shown in Figure 5-1a, is fairly symmetrical. The maximum velocity gradient interface and zero velocity line coincide at the depth of $y = 0.48H$ approximately at $x = 0.5L$. The measured velocity difference between the two layers $\Delta U = |U_1 - U_2| \approx 4.8$ cm/s, and the estimated shear layer thickness $\delta = \Delta U / (\partial u/\partial y)_{\max} \approx 3.4$ cm

for E5. The estimated shear layer thickness δ ranges from 3.2 to 3.7 cm for the remaining experiments.

In contrast with the shear layer, the density interface is fairly sharp for E5, as shown in Figure 5-1b. The estimated density interface thickness $\varsigma = \Delta\rho/(\partial\rho/\partial y)_{\max} \approx 1.1$ cm, which is about 32% of the shear layer thickness. The large ratio of the shear layer thickness to the density interface thickness is very common in salinity stratified flows (e.g. Koop & Browand, 1979; Zhu & Lawrence, 2000). This is due to the fact that the ratio of eddy diffusivity to eddy viscosity κ_e/ν_e (eddy Prandtl number) decreases with increasing Richardson number Ri. The data of Webster (1964) indicates κ_e/ν_e will be significantly less than one for high Ri.

The position of the density interface at $x = 0.5L$ is approximately located at mid-depth (i.e. $y = 0.50H$), which is slightly shifted upwards from both the maximum velocity gradient interface and the zero velocity line. The shift between the density and the velocity interfaces is found insignificant for all densimetric exchange flow experiments listed in Table 5-1, and is largely due to the effect of the bottom boundary layer. It is also noted that the density interface location obtained by the conductivity probe agrees well with the visual interface formed by the dye mixed in the lower layer. The interface image created by mixing dye in the lower layer was processed to determine the density interface position throughout the channel.

The exchange rate was obtained by integrating horizontal velocity profiles $u(y)$ with respect to depth y. Specifically, integrating from the channel bottom, $y = 0$, to the interface, $y = y_2$, yields the lower layer flow rate q_2,

$$q_2 = \int_{y=0}^{y=y_2} u(y)dy = \frac{Q_2}{b}, \tag{5-3}$$

where Q_2 is the volumetric flow rate for the lower layer, b is the channel width.

Similarly, integrating from the interface, $y = y_2$, to the free surface, $y = y_1 + y_2 = H$, yields the upper layer flow rate q_1,

$$q_1 = \int_{y=y_2}^{y=H} u(y)dy = \frac{Q_1}{b}, \tag{5-4}$$

where Q_1 is the volumetric flow rate for the upper layer. Obviously, for densimetric exchange flows, $Q = -Q_1 = Q_2$, i.e. the total or net flow rate is zero.

5.1.2 Estimation of Interfacial Friction

An accurate estimate of the interfacial frictional coefficient has not been established so far, as concluded after a comprehensive literature review on interfacial friction in Chapter 2. Therefore, the interfacial friction factor, f_I, was determined experimentally based on the principle of conservation of energy.

Using the measured exchange flow rate and density interface position along the channel, the interfacial friction factors were evaluated by integrating the equation of motion, $dE/dx = S_f$, in the dimensional form. Integrating the equation of motion in the horizontal direction over the whole length of the channel leads to:

$$E_{x=L} - E_{x=0} = \int_{x=0}^{x=L} S_f dx = \frac{q^2}{g'b}\int_{x=0}^{x=L} f_w\left(\frac{1}{y_1^2} + \frac{1}{y_2^2}\right)dx + \frac{q^2}{2g'}\int_{x=0}^{x=L} f_b \frac{1}{y_2^3}dx + \frac{q^2}{2g'}\int_{x=0}^{x=L} f_I\left(\frac{1}{y_1} + \frac{1}{y_2}\right)^3 dx, \tag{5-5}$$

which, upon rearrangement, yields the following expression for the interfacial friction factor $\bar{f}_I$ averaged over the whole length of the channel:

$$\bar{f}_l = \frac{1}{L}\int_{x=0}^{x=L} f_l\,dx = \frac{E_{x=L} - E_{x=0} - \dfrac{q^2 \bar{f}_w}{g'b}\displaystyle\int_{x=0}^{x=L}\left(\frac{1}{y_1^2}+\frac{1}{y_2^2}\right)dx - \dfrac{q^2 \bar{f}_b}{2g'}\displaystyle\int_{x=0}^{x=L}\frac{1}{y_2^3}dx}{\dfrac{q^2}{2g'}\displaystyle\int_{x=0}^{x=L}\left(\frac{1}{y_1}+\frac{1}{y_2}\right)^3 dx}, \quad (5\text{-}6)$$

where $E_{x=0}$ and $E_{x=L}$ are measured internal energy heads at each end of the channel, q is the measured unit exchange flow rate, y_1 and y_2 are measured upper and lower layer depths respectively, b and L are channel width and length respectively, and g' is the measured reduced gravity. $\bar{f}_w = 1/L\int_{x=0}^{x=L} f_w dx$ and $\bar{f}_b = 1/L\int_{x=0}^{x=L} f_b dx$ are averaged wall and bottom frictional factors respectively, which are estimated using the boundary layer theory discussed below.

The integral momentum method, the Thwaites method (White, 1991), was used to determine the average wall and bottom frictional factors for exchange flow through a straight channel. Unlike other boundary layer theories (e.g. the Blasius theory), which usually assume a uniform velocity field over the whole length of the boundary layer, the Thwaites method analyses the boundary layer development over a flat plate with a horizontal velocity gradient. The computer algorithm used by Zhu & Lawrence (2000) in studying the exchange flow through a channel with an underwater sill was modified and utilized in this study. Refer to White (1991) and Zhu (1996) for detailed theoretical formulation and assumptions in applying the Thwaites method to exchange flow problems.

5.1.3 Comparison with Laboratory Experimental Data

In this section, quantitative comparisons between experimental measurements (as listed in Table 5-1) and the theoretical predictions from the analytical solutions to open channel exchange flows are made.

The analytical solutions developed in this study assume a wide channel or culvert. Although such an assumption is generally sound in practice, it is not always the case for laboratory experiments, where the modelled channels can be fairly narrow. As a result, some kind of the equivalent or effective interfacial and bottom frictional factors, f_{I_e} and f_{b_e}, are needed to accommodate comparisons between theoretical predictions and laboratory experiments described earlier in this section.

The effective frictional factors are formulated such that total shear forces acting on a control volume of width b, length dx, and depth y_1 or y_2, as shown in Figure 3-2, are balanced. For the upper layer of a two-layer flow system, the balance of total shear forces acting on unit channel width between a narrow channel of width b (RHS) and an equivalent wide channel (LHS) yields:

$$\frac{1}{2} f_{I_e} \overline{\rho} \Delta U^2 dx = \frac{\left(f_w \rho_1 U_1^2 y_1 + \frac{1}{2} f_I \overline{\rho} \Delta U^2 b \right)}{b} dx , \qquad (5\text{-}7)$$

where f_{I_e} is the effective interfacial frictional factor of an equivalent wide channel, f_I and f_w are the interfacial and sidewall frictional factors of a narrow channel respectively, $\Delta U = |U_1 - U_2|$ is the horizontal velocity shear between the two layers, $\overline{\rho} = (\rho_1 + \rho_2)/2$ is the mean density of two layers.

Re-arranging terms in (5-7) leads to:

$$f_{I_e} = f_I + \frac{4 r U_1^2 y_1}{\Delta U^2 (1+r) b} f_w , \qquad (5\text{-}8)$$

where $r = \rho_1 / \rho_2$ is the density ratio. For Boussinesq flows, $r \approx 1$.

Assuming a linear symmetrical density interface along the channel and integrating (5-8) in the horizontal direction over the whole length of the channel yield:

$$\bar{f}_{I_e} = \bar{f}_I + \frac{H}{4b}\bar{f}_w, \tag{5-9}$$

where $\bar{f}_{I_e}$ is the average effective interfacial friction factor of an equivalent wide channel, $\bar{f}_I$ and $\bar{f}_w$ are estimated average interfacial and wall friction factors of a narrow channel respectively, and H is the total depth of the channel.

Obviously, for narrow channels (i.e. $H/b >> 1$), $\bar{f}_{I_e} >> \bar{f}_I$, hence the effect of the sidewall friction is more significant. For wide channels (i.e. $H/b << 1$), on the other hand, $\bar{f}_{I_e} \to \bar{f}_I$, hence the effect of the sidewall friction is negligible. Take the Burlington Ship Canal, for example. $\bar{f}_{I_e}/\bar{f}_I$ is estimated to be about 1.07 based on $H = 9.5\,\text{m}$, $b = 89\,\text{m}$, and $f_r = \bar{f}_{I_e}/\bar{f}_{w_e} = 0.39$. This indicates that the Burlington Ship Canal could be considered wide in the hydraulic sense, although it might otherwise be considered relatively narrow based on its physical scales only.

Similarly, for the lower layer of a two-layer flow system, the balance of total shear forces acting on unit channel width between a narrow channel of width b (RHS) and an equivalent wide channel (LHS) yields:

$$\left(\frac{1}{2}f_{I_e}\overline{\rho}\Delta U^2 + \frac{1}{2}f_{b_e}\rho_2 U_2^2\right)dx = \frac{\left(\frac{1}{2}f_b\rho_2 U_2^2 b + f_w\rho_2 U_2^2 y_2 + \frac{1}{2}f_I\overline{\rho}\Delta U^2 b\right)}{b}dx, \tag{5-10}$$

where f_{b_e} is the effective bottom friction factor of an equivalent wide channel, f_I, f_b and f_w are the interfacial, bottom and sidewall friction factors of a narrow channel respectively.

Substituting (5-8) into (5-10) and re-arranging terms lead to:

$$f_{b_e} = f_b + \frac{2\left(U_2^2 y_2 - U_1^2 y_1\right)}{U_2^2 b}f_w. \tag{5-11}$$

Again, assuming a linear symmetrical density interface along the channel and integrating (5-11) in the horizontal direction over the whole length of the channel yield:

$$\bar{f}_{b_e} = \bar{f}_b, \tag{5-12}$$

where $\bar{f}_{b_e}$ is the average effective bottom friction factor of an equivalent wide channel, and $\bar{f}_b$ is the estimated average bottom friction factor of a narrow channel. $\bar{f}_{b_e}$ is equal to $\bar{f}_b$, since the influence from sidewalls of a narrow channel has already been incorporated into the effective interfacial friction factor $\bar{f}_{I_e}$ in (5-9).

Once the average effective frictional factors are determined by Equations (5-9) and (5-12), the analytical exchange flow solutions (e.g. the exchange flow rate and interface profile) can be solved, and the obtained theoretical predictions are then compared to the experimental measurements. The predictions are obtained using the iteration procedures described in Appendix B based on the given frictional parameters of α and f_r. More detailed comparison will be made for E5 first. This is followed by comparisons of the exchange flow rates for the remaining experiments.

Figure 5-3 shows the comparison between the laboratory measurements of E5 and the theoretical predictions for density interface position, the composite Froude number G^2, and the internal energy variations throughout the channel. Both predicted and measured density interface profiles exhibit a roughly linear interface profile for most part of the channel yet are increasingly curved towards either end, as shown in Figure 5-3a. This interface profile characteristic is also very consistent with previous experimental and numerical modelling findings (e.g. Anati *et al*, 1977; Dick & Marsalek, 1972; Assaf & Hecht, 1974). The theoretical formulation of two-layer maximal exchange flows assumes the co-existence of hydraulic controls at both ends of the channel and subcritical flow regime within the channel. This assumption is verified by the laboratory measurements, as shown in Figure 5-3b. The composite Froude number is below unity in the interior and gradually increases to unity at each end of the channel. The comparison of internal energy variation along the channel is shown in Figure 5-3c.

The frictional effects increase the interface slope and hence reduce the exchange flow rate. The inviscid two-layer hydraulic theory, on the other hand, would predict a horizontal interface and a composite Froude number $G^2 = G_o^2 = 1$ throughout the channel. For the experimental run of E5, the inviscid exchange flow solution would give a unit exchange flow rate of 39.6 cm^2/s, which is about 28% higher than the actual laboratory measurement of 30.9 cm^2/s. It should be noted that this 28% reduction in exchange flow rate is experienced in a fairly short experimental channel, which has a frictional parameter $\alpha = 0.074$ for E5. For natural channels and sea straits, more substantial exchange rate reduction would be expected since they are subject to much larger frictional parameters α, as shown in Table 2-1. Thus inviscid exchange flow solutions have very limited applicability.

For all eight experimental runs listed in Table 5-1, exchange flow rates were predicted using both frictional and inviscid exchange flow theories. The comparisons between the theoretical predictions and the laboratory measurements are shown in Figure 5-4. Again, there is very good agreement between the measured flow rates and analytical solutions developed in this study in each of the eight experimental runs, with all the data points falling within the $\pm 5\%$ error lines. The inviscid exchange flow theory, however, overestimates the exchange flow rates for all laboratory experiments, with the maximum error of about +35% for E1. Therefore, frictional effects can not be ignored even for the laboratory experimental channels with the frictional parameter α ranging from 0.05 to 0.09. It is noted that such a small range of α values indicates a fairly short channel and the frictional effects might otherwise be ignored.

In summary, comparisons between the theoretical predictions and the laboratory measurements are excellent in general. However, laboratory measurements are always influenced by interfacial wave activities within the channel especially near both ends of the channel, as indicated by the vertical error bars in Figure 5-3a. The measurements within the channel may also be tempered by the interface fluctuations in the reservoirs, since the

hydraulic controls at the channel ends are in the sense of long internal waves, and hence are not able to completely isolate the short waves, which may propagate into the channel. Mixing between two fluid layers may also take place. In these cases, some of the basic two-layer hydraulic assumptions are violated to some degree and, as a result, some discrepancies between the theoretical predictions and laboratory measurements are expected.

5.2 COMPARISONS WITH FIELD DATA

This section seeks to compare the theoretical predictions on two-layer maximal densimetric exchange flows with field flow measurement data in the Burlington Ship Canal as well as several famous sea straits.

The field data for the Burlington Ship Canal were compiled from the early field measurements of Dick & Marsalek (1973) and Spigel (1988) as well as the latest comprehensive field experiments conducted in July and August of 1996 (Greco, 1998). Unlike the laboratory densimetric exchange flow experiments, the naturally occurring exchange flows are more or less subject to the influence of barotropic flow components. Therefore, the field data was pre-screened such that only exchange flows with relatively strong densimetric flow components were used for the comparison purpose. The relative strength of the densimetric exchange flow component is measured quantitatively by an exchange flow strength parameter (Greco, 1998), R, which is defined as:

$$R = \left| \frac{q_1 - q_2}{q_1 + q_2} \right|. \tag{5-13}$$

Exchange flow is more prominent if $R > 1$, since q_1 and q_2 are of opposite sign. On the other hand, if $R < 1$ the barotropic flow component is more dominant and the flow is

unidirectional since q_1 and q_2 are of opposite signs. Obviously, $R = \infty$ for pure exchange flows ($q_1 = -q_2$), and $R = 0$ for plug flows.

The selected measurement data from above three sources are summarized in Table 5-2, where g' is the reduced gravity, q_1 is the unit outflow from the Hamilton Harbour to Lake Ontario in the upper layer, q_2 is the unit inflow from Lake Ontario to the Hamilton Harbour in the bottom layer, q_m is the measured unit densimetric exchange flow component, and q_p is theoretical prediction using the analytical solutions detailed in Chapter three.

Table 5-2. Comparison with field data in the Burlington Ship Canal

Data Sources	Measurement Runs	g' (m/s^2)	q_1 (m^2/s)	q_2 (m^2/s)	R	q_m (m^2/s)	q_p (m^2/s)
Greco (1998)	Drift B	0.0204	1.03	-0.73	5.9	0.73	0.74
	Drift D	0.0202	0.67	-0.97	5.5	0.67	0.73
	Drift E	0.0217	1.07	-0.81	7.2	0.81	0.76
Spigel (1988)	9-June-1988	0.0088	0.63	-0.51	9.4	0.51	0.48
	15-June-1988	0.0180	0.72	-0.67	31.0	0.67	0.69
	21-June-1988	0.0092	0.58	-0.96	4.1	0.58	0.49
	6-July-1988	0.0035	0.50	-0.32	4.6	0.32	0.31
Dick & Marsalek (1973)	1	0.0162	0.53	-0.49	29.3	0.49	0.66
	6	0.0175	0.50	-0.61	10.3	0.50	0.68
	7	0.0165	0.50	-0.39	34.3	0.39	0.66
	8	0.0189	0.47	-0.58	42.2	0.47	0.71

A bottom frictional coefficient $f_b = 0.0026$ and an interfacial frictional coefficient $f_i = 0.001$, as recommended by Dick & Marsalek (1973), were used in the theoretical predictions. These frictional coefficients were also used by Hamblin & Lawrence (1990) with considerable success. Given the total depth $H = 9.5\,\text{m}$ and the total length $L = 836\,\text{m}$, the frictional parameter $\alpha = f_b L/H$ for the Burlington Ship Canal is calculated to be about 0.23.

It should be noted that the bottom frictional coefficient used in the one-dimensional steady exchange flow analysis is an effective one. It usually includes the combined effects of bottom friction as well as, for example, the irregularity in geometry, unsteadiness, three dimensionality, and wall frictions to a lesser extend under the field conditions. Therefore, it is not surprising to see a wide range of scattering for the quoted bottom frictional coefficients, which typically range from $O(10^{-3})$ to $O(10^{-2})$. Bowden & Fairbairn (1952), for example, indicated that typical bottom friction coefficients should be in the order of 10^{-3} for tidal current calculations. Oguz *et al.* (1990) found that a bottom frictional coefficient of $f_b = 0.0046$ was supported by numerical modelling results of exchange flow in the Bosphorus Strait. Direct measurements of bottom frictional coefficients along the California shelf (Grant *et al.*, 1984) show that f_b can be as large as 0.0088. Defant (1961), on the other hand, argued that due to the irregular bottom geometry the bottom frictional coefficient in natural straits should be similar to those used in rivers, i.e. about 0.03, which is about 10 times larger than the one used for smooth channels. Maderich & Efroimson (1986) maintained a bottom frictional coefficient of 0.012 for sea straits. Hence, a bottom frictional coefficient of $f_b = 0.0026$ for the Burlington Ship Canal is in the lower range of usually quoted values for f_b. This is largely due to the relatively regular geometry of the ship canal in comparison with many other natural channels or straits.

The comparison (also shown in Figure 5-5) is very good in general, except for the field measurements by Dick & Marsalek (1973), where the theoretical predictions by the analytical exchange flow solutions largely overestimate exchange flow rates by as much as 70% for measurement run 7. This is because the two-layer fluid structures in Lake Ontario and the Hamilton Harbour are such that the hydraulic controls at either end of the ship canal are flooded. In another word, the exchange flows observed by Dick & Marsalek (1973) are actually submaximal in nature, as indicated by the subcritical flow conditions near both ends of the ship canal with the composite Froude number G^2 ranging approximately from 0.31 to

0.40. For comparison purpose, solutions based on inviscid and linear frictional exchange flow theories are also plotted in Figure 5-5. The linear frictional exchange flow solution of Anati *et al.* (1977) is based on the assumptions that non-linear inertial effects are negligible in comparison with frictional effects for longer channel (i.e. $\alpha >> 1$) and the density interface is linear throughout the channel. The interfacial friction is also ignored in their theoretical formulation (i.e. $f_r = 0$). Both inviscid and linear exchange flow solutions are found to overestimate the exchange rates for all the field data. It is worth noting that although based on fundamentally different assumptions the predictions from the inviscid and the linear frictional exchange flow solutions are remarkably close. This is due to the fact that the inertial and the frictional forces are equally important in the Burlington Ship Canal and neither of them can be neglected in the exchange flow analysis in the canal.

The Burlington Ship Canal is rather short, as indicated by its relatively small value of the frictional parameter ($\alpha = 0.23$). To further validate the applicability of the analytical exchange flow solutions for longer channels, the theoretical predictions are also compared with the field flow measurements in several famous sea straits. These are summarized in Table 5-3, in which L, H, and b are average length, total depth, and width of the sea strait respectively.

Table 5-3. Comparison with field data in several famous sea straits

Sea Strait	L (km)	H (m)	b (km)	g' (m/s^2)	R	f_l	f_b	α	q_m (m^2/s)	q_p (m^2/s)
Gibraltar (Defant, 1961)	60	300	20.0	0.019	32.2	0.0024	0.012	2.4	82.3	76.5
Gibraltar (Maderich & Efroimson, 1986)	60	300	20.0	0.013	50.7	0.0024	0.012	2.4	60.9	63.1
Bosphorus (Defant, 1961)	30	60	0.8	0.137	4.8	0.0024	0.0046	2.3	15.3	15.2
Dardanelles (Defant, 1961)	60	70	4.0	0.103	2.9	0.0024	0.012	10.3	1.5	11.3
Bab-el-Mandeb (Defant, 1961)	160	172	18.5	0.029	8.0	0.0024	0.012	11.2	21.9	22.5

Except for the Bosphorus Strait, a bottom frictional coefficient $f_b = 0.012$ (as recommended by Maderich & Efroimson, 1986) was used. A bottom frictional coefficient of $f_b = 0.012$ is in the same order of magnitude as values used for natural straits, as discussed early in this section. For the Bosphorus Strait, however, a bottom frictional coefficient $f_b = 0.0046$ (as recommended by Oguz *et al.*, 1990) was used. An interfacial frictional coefficient $f_I = 0.0024$ was applied to all of the sea straits considered. This value of interfacial friction coefficient is close to the values generally employed in the numerical studies of strait exchange flows (e.g. Assaf & Hecht, 1974). The above adopted bottom frictional coefficients lead to frictional parameters of 2.3, 2.4, 10.3, and 11.2 for Bosphorus Strait, Strait of Gibraltar, Dardanelles Strait, and Bab-el-Mandeb Strait respectively.

The comparisons between the predictions of the analytical exchange flow solution and the field flow measurements are very good in general, as also shown in Figure 5-6. Except for Dardanelles Strait, the relative errors between the predictions and the measurements are all within 7%. In the past, exchange flow predictions for natural straits largely rely on numerical simulations. Considering the very irregular geometry of natural straits, the predictions by the one-dimensional analytical exchange flow solution are remarkably close to the field measurements. This is largely due to the facts that the interfacial friction may play an importance role in the two-way exchange and the effects of irregular channel geometry have been somehow incorporated into the effective bottom friction factors. The large prediction error for Dardanelles is due to the relatively strong barotropic flow component, as indicated by the small R value.

As expected, the linear frictional exchange flow solutions of Anati *et al.* (1977) compared well with the analytical exchange flow solutions for longer straits (i.e. Dardanelles Strait and Bab-el-Mandeb), since the non-linear inertial effects tend to be negligible in these long straits. For shorter straits (i.e. Bosphorus Strait and Strait of Gibraltar), on the other hand, the

linear frictional solutions tend to overestimete the exchange rate, since inertial effects became more important in these straits.

5.3 DISCUSSION

5.3.1 The Analytical Solution versus the Numerical Integration

The analytical exchange flow theory developed in this study successfully solved the fully non-linear frictional exchange flow problems. Traditionally, solutions to such problems have been heavily dependent on either numerical integration or field studies on a site-specific basis. Besides the obvious advantages of being more instructive and easy to apply, the analytical exchange flow solution has some other merits over the numerical integration approach.

For maximal exchange flows, the analytical exchange flow solution uniquely defines a longitudinal density profile along the channel, $\eta(\chi)$ or $y_2(x)$, in the form of a interface equation for any given frictional parameters (i.e. α and f_r) and a pre-specified exchange rate (G_o^2) - depth (η) relationship (i.e. critical condition of $G^2 = 1$) at hydraulic control locations. Since the integration of the equation of motion is direct by the analytical solution, the successive values of y_2 are independent of each other in the interface equation. Therefore, the calculation of interface profile may be proceeded in independent steps as shown schematically in Figure 5-7a.

The numerical integration, on the other hand, usually starts at a control location and proceeds step by step in the direction in which the control is being exercised (e.g. Assaf & Hecht, 1974). Therefore, each step of the stepwise numerical integration is dependent on the proceeding one, as illustrated in Figure 5-7b. As a result, the numerical error tends to accumulate during the numerical integration process, especially near the hydraulic control

regions where interface slopes are relatively large. This would require very small grid space to be used in the numerical integration. In fact, the numerical integration procedure of Assaf & Hecht (1974) stopped slightly short of the critical condition at the right end of the channel ($x = L$) to avoid the singularity there.

5.3.2 Non-linear Effects and the Shape of the Density Interface

The analytical exchange flow solution developed in this study is based on the fully non-linear one-dimensional shallow water equation of a two-layer fluid system. Therefore, both inertial and frictional effects are included in the theoretical formulation. As a result, the solution is applicable to a wide range of flow conditions, as demonstrated in the comparisons with laboratory and field flow measurements. The linear frictional exchange flow solutions (e.g. Anati *et al.* 1977), on the other hand, neglect the non-linear inertial terms. Therefore, these solutions are only applicable to longer channels, where frictional effects tend to dominate over inertial effects. Furthermore, the interfacial friction is completely neglected in their theoretical formulation.

For the first time, precise interface equations for two-layer frictional exchange flows were solved analytically. Previous field and laboratory studies on exchange flows (e.g. Dick & Marsalek, 1972; Anati *et al.*, 1977) indicate two characteristics of interface profiles. They are nearly linear throughout most of the channel length, and are curved at each end of the channel. Since no precise interface equation was derived before, the linear density interface profile has been widely used as the first approximation in the previous theoretical formulations of analytical solutions on frictional exchange flows (e.g. Maderich & Efroimson, 1986, 1990; Anati *et al.*, 1977). The linear density interface profile assumes that the density interface follows a straight line linking two hydraulic controls. Given the pronounced non-linear nature of exchange flow problems, however, this assumption may not be appropriate. This is confirmed by the interface profile equation developed in this study. It

is noted that for open channel exchange flows the interface profile is not only non-linear, but also non-symmetric due to the fact that bottom friction is included, but surface friction is assumed to be absent. The non-symmetrical nature of the density interface is indicated by the two logarithmic terms in the interface equation (see 3-37). As a result, it is more curved near the exit on the left end of the channel ($x = 0$), as shown in Figure 5-8.

5.3.3 Effects of Friction on Exchange Rates

One way to examine the equation of motion is that it defines the relationship between the energy loss and the exchange flow rate through a channel for specified frictional parameters. Lengthening the channel or increasing the frictional factors would increase the energy loss and hence reduce the exchange rate. On the other hand, if the energy loss were reduced to zero, then the maximum possible exchange flow rate would be achieved. The scenario of zero energy loss could be considered as the limiting case of zero channel length or zero frictional resistance. In this case, the flow is critical and the two layers are of equal thickness ($y_1 = y_2 = \frac{1}{2}H$) throughout the channel, i.e.

$$G^2 = \frac{q^2}{g'y_1^3} + \frac{q^2}{g'y_2^3} = \frac{16q^2}{g'H^3} = G_o^2 = 1. \qquad (5\text{-}14)$$

Therefore, $\frac{1}{4}\sqrt{g'H^3}$ is the maximum possible exchange flow rate for given reduced gravity g' and total depth H (for inviscid exchange flows), and hence $G_o = 4q/\sqrt{g'H^3}$ conveniently defines the ratio of frictional exchange rate to inviscid exchange rate.

To demonstrate the frictional effects on exchange flow rate, analytical exchange flow solutions, expressed in terms of G_o, are plotted against the frictional parameter α for four different friction ratios of f_r in Figure 5-9. The frictional parameter α is used as an indicator of frictional effects and f_r is the frictional ratio indicating the relative importance of interfacial friction. The laboratory experiment data as well as field flow measurements in the Burlington Ship Canal and several famous sea straits are also shown in the Figure 5-9.

The linear frictional exchange flow solution of Anati *et al.* (1977) is plotted as well for comparison. The frictional ratio f_r ranges roughly from 0.7 to 1 for laboratory experiments and from 0.2 to 0.4 for field data respectively. Zero interfacial friction (i.e. $f_r = 0$) is assumed in Anati *et al.*'s linear frictional exchange flow solution.

It is noted that G_o reduces significantly with the increasing of α, indicating that frictional effects usually can not be ignored in natural channels. The exchange flow rate would reduce, for example, by almost 19% from its inviscid solution (i.e. $G_o = 1$) at $\alpha = 0.2$ for $f_r = 0.1$. The reduction in flow rate would be further increased to as much as 39% with increasing interfacial friction for $f_r = 1.0$ at $\alpha = 0.2$. A channel with a frictional parameter of $\alpha = 0.2$ is considered fairly short, and a frictional ratio f_r between 0.1 and 1.0 is very typical for natural exchange flows. In the case of the Burlington Ship Canal, given $\alpha = 0.23$ ($H = 9.5\,\text{m}$, $L = 836\,\text{m}$, and $f_b = 0.0026$) and $f_r = 0.38$, this give a solution of $G_o = 0.71$. This would indicate about a 29% drop in exchange rate from its inviscid solution, even though a channel with $\alpha = 0.23$ might otherwise be considered short enough to ignore frictional effects.

It is rather difficult to make direct comparison between the linear and the analytical frictional exchange flow solutions, since different assumptions have been used in their theoretical formulations. However, general examination of Figure 5-9 do indicate that the linear frictional exchange flow solution tends to significantly overestimate the exchange flow rate in shorter channels, where the non-linear inertial effects are generally not negligible. As expected, the differences between the analytical exchange solutions (say for $f_r = 0.1$) and the linear frictional exchange solutions are narrowed for longer channels, since the frictional effects would dominant in longer channels.

The $G_o - \alpha$ curves in Figure 5-9 indicate that the frictional parameter α is a fairly good indication of frictional effects in general sense. However, it is found that the frictional

parameter α alone is not enough to provide an accurate measure on the dynamic channel length, since exchange rates can be substantially reduced from their inviscid values even in those channels with very small α values. This is largely due to the fact that the interfacial friction is not accounted for in the channel classification scheme of Anati *et al.* (1977). The relative importance of the interfacial friction will be discussed in the next section.

5.3.4 Relative Importance of Interfacial and Bottom Friction

It is noted that the interfacial friction, as expressed by the friction ratio $f_r = f_I / f_b$, is important in determining the exchange rate. In fact, the interfacial friction factor f_I can be the same order as the bottom friction factor f_b (e.g. Dermissis & Partheniades, 1984). More importantly, the interfacial friction is subject to larger velocity shear at the density interface, as upper and lower layers move in the opposite direction for two-layer exchange flows.

To further examine the relative importance of interfacial and bottom friction, it is useful to separate the interfacial friction and bottom friction slopes from the total friction slope S_f. For wide channels, the total friction slope can be expressed as the sum of the interfacial and the bottom friction slopes in the following non-dimensional form:

$$S_f = S_{f_I} + S_{f_b} = \frac{f_I G_o^2}{32 y_1^3 y_2^3} + \frac{f_b G_o^2}{32 y_2^3}.$$

The relative importance of interfacial and bottom frictions can be determined by the ratio between their corresponding friction slopes, S_r,

$$S_r = \frac{S_{f_I}}{S_{f_b}} = \frac{(f_I G_o^2)/(32 y_1^3 y_2^3)}{(f_b G_o^2)/(32 y_2^3)} = f_r \left(1 + \frac{y_2}{y_1}\right)^3 = 8 f_r \left(\frac{1}{1-2\eta}\right)^3 \qquad (5\text{-}15)$$

Therefore, the friction slope ratio, S_r, would vary with the layer thickness ratio, y_2/y_1, throughout the channel. At the left end of the channel (i.e. $x=0$), for example, the friction slope ratio would be at its minimum with reduced lower layer thickness. The reduced lower layer thickness means intensified lower layer flow, and hence increased bottom frictional effect. While at the right end of the channel (i.e. $x=L$), the friction slope ratio would reach its maximum value. For densimentric exchange flows, the over-all layer thickness ratio is approximately unity when averaged over the whole length of the channel. This would indicate an average interfacial to bottom friction slope ratio of about eight for $f_r=1$. In another words, the interfacial friction would be equally important as the bottom friction even with a frictional ratio $f_r=0.125$.

Take the Burlington Ship Canal for example, the average friction slope ratio, S_r, is estimated to be about 3, given the frictional ratio of $f_r=0.38$ ($f_i=0.001$ and $f_b=0.0026$). This indicates that, even though $f_b>f_i$, the interfacial friction is actually more important than the bottom friction for exchange flows in the ship canal. The average friction slope ratio for all eight laboratory experiments is estimated to be about 2.9, given the range of frictional ratio $f_r=0.24\sim0.52$ ($f_i=0.0031\sim0.0041$ and $f_b=0.007\sim0.013$). The range of interfacial frictional factors $f_i=0.0031\sim0.0041$ are comparable with $f_i=0.0021\sim0.0054$ reported by Sargent & Jirka (1987) for similar flow conditions (Re= 4100~9800 and K= 620~2340). It is noted that much larger interfacial frictional factors ($f_i=0.007\sim0.019$) have been reported by Zhu & Lawrence (2000) for exchange flows through an experimental channel with an underwater sill. Presumably, the difference is due to interfacial instabilities observed in their laboratory experiments.

5.3.5 Effects of Moderate Barotropic Forcing

Although this study is mainly concerned with pure densimetric exchange flows, limited laboratory experiments on two-way exchange with a moderate barotropic flow component

were also carried out. Some preliminary experimental findings as well as their practical implications are discussed in this section. The barotropic forcing is moderate in the sense that both layers move in opposite directions, or is strong, such that the flow is unidirectional (Armi & Farmer, 1986). The strength of the barotopic forcing can be measured by a non-dimensional parameter, $q_b^* = q_b / \sqrt{g' H^3}$, where g', H and q_b are the reduced gravity, the total fluid depth, and the unit barotropic flow rate respectively. $q_b^* = 1$ corresponds to the lower limit of frictionless plug flow, under this condition the barotropic forcing overwhelms the two-way exchange flow to yield a unidirectional flow. Therefore, in the absence of friction, the imposed barotropic flow is considered to be strong, if $q_b^* \geq 1$, and the imposed barotropic flow is considered to be moderate, if $0 < q_b^* < 1$.

Conventional two-layer hydraulics assumes the coincidence of density and velocity interfaces. However, preliminary laboratory experiments conducted in this study indicate that this assumption is questionable for two-layer exchange flows with moderate barotropic flow components. The displacement of the density interface from the velocity interface has been commonly referred to as "one-sidedness" in salt-wedge type of flows (Keulegan, 1966; Sargent & Jirka, 1987; Yonemitsu *et al.*, 1996). Other experimental studies showing the shift of the density interface from the velocity interface include, for example, Lock (1951), Koop & Browand (1979) and Lawrence *et al.* (1991), all dealing with two-layer shear flows with both layers moving in the same direction. The experimental observation of the shifting between density and velocity interfaces in a two-layer exchange flow, where both layers are moving in the opposite directions, is unique and interesting.

Figure 5-10 shows the measured density and velocity profiles at the center of the channel ($x = 0.5L$) for E9, in which a barotropic flow is applied from left to right in the upper layer. The barotropic flow strength parameter q_b^* is estimated to be about 0.27, given a barotropic flow of $q_b = 28.5\,\text{cm}^2/\text{s}$, the reduced gravity $g' = 0.49\,\text{cm/s}^2$, and total fluid depth of $H = 28.0\,\text{cm}$. The density interface is displaced upward from the zero velocity line by about

2.2 cm. As a result of this shifting, the mixed lower layer water is carried back to the right reservoir with the upper layer flow. The shift of the density interface from the velocity or shear interface could be explained by the net entrainment between the two adjacent layers. Although the entrainment is essentially a two-way transport process, it is commonly defined as the buoyancy flux associated with the net volume transport from less energetic to more energetic entraining fluid layer. As a result, the density interface is displaced towards the fast moving layer, as shown schematically in Figure 5-11.

The density interface shifting has significant practical implications for the water exchange through the Burlington Ship Canal. The exchange flows are beneficial only if the exchanged water mixes completely with the receiving water bodies. For the Hamilton Harbour, if inflows from the Lake Ontario are "short-circuited" to the outflows without effectively mixing with the main body of harbour water, the lake inflows will have less benefit in flushing the harbour.

Two short-circuiting mechanisms in the Burlington Ship Canal were identified in the previous studies (Spigel, 1989; Barica *et al.*, 1987; Kholi, 1984). The first short-circuiting mechanism involves with sewerage effluents from the Hamilton and Burlington Sewage Treatment Plants. The effluent flumes could advect along the eastern shoreline and directly reach the outlet of the harbour without extensive mixing with the main water body of the harbour. This is obviously beneficial to the water quality of the harbour. The second short-circuiting mechanism is associated with the frequent flow reversals of exchange flows in the Burlington Ship Canal. If the flow reversals occur before effective mixing and circulation in the harbour or in the coastal region of Lake Ontario could happen, then the lake water may be short-circuited out of the harbour before effective exchange with harbour water could take place, and vice versa.

The "one-sidedness" phenomenon observed in the laboratory experiment indicates that there could be a third short-circuiting mechanism in exchange flows through the Burlington Ship Canal. This will mainly be associated with exchange flows with a moderate barotopic flow component. The short-circuiting occurs when the slow-moving layer being entrained into the fast-moving layer to create a secondary reversing middle layer flow.

CHAPTER 6

CONCLUSIONS AND RECOMMENDATIONS

The steady gravitational exchange of two fluids of differing density between two reservoirs connected by a rectangular channel of horizontal bottom and constant width was studied both theoretically and experimentally. The rectangular channel was selected as it removes the unnecessary complexities associated with variable channel geometry and essentially isolates the most important features of the frictional exchange process. This flow configuration also closely resembles the field flow conditions in the Burlington Ship Canal.

Prior to this study, there were two distinct analytical approaches to the two-layer exchange flow problems, namely, the inviscid and the linear frictional exchange flow theories. The inviscid exchange flow theory completely ignores the frictional effects. Consequently, it is only applicable to very short channels. Many well-known sea straits, however, can not be considered short even based on conservative values of bottom frictional factors. The linear frictional exchange flow theory, on the other hand, completely ignores the non-linear inertial effects. As a result, the linear frictional exchange flow theory is only applicable to very long channels, where frictional effects tend to be dominant over non-linear inertial effects.

Under many circumstances, however, both frictional and inertial effects are important and hence neither of them should be neglected in the theoretical formulation of exchange flow problems. To this end, the fully non-linear one-dimensional shallow-water equation must be used to describe frictional exchange flow problems. So far, solutions to such problems have been exclusively obtained through numerical integration.

By solving the fully non-linear hydraulic equation through direct integration as a boundary value problem, an analytical solution has been found for the two-layer densimetric frictional

exchange flow through a wide rectangular channel. Given the frictional parameter $\alpha = f_b L/H$ and the frictional ratio $f_r = f_l/f_b$, the analytical frictional exchange flow solution enables the prediction of a precise density interface profile along the channel $\eta(\chi)$ and a non-dimensional exchange flow rate $G_o = 4q/\sqrt{g'H^3}$. The resulting theoretical predictions compared well with both laboratory experiments and field measurements in the Burlington Ship Canal as well as several famous sea straits.

A constant width channel with sudden expansions at each end has two internal hydraulic controls at both ends. Between these two control locations, the frictional effects act to modify the slope of the density interface of a subcritical exchange flow. The resulting analytical exchange flow solution indicates that frictional effects significantly increase the overall interface slope, and hence reduce the exchange flow rate. The interfacial friction, in particular, plays an important role in determining the exchange flow rate. This is largely due to the fact that the interfacial friction is subject to larger velocity shear at the density interface, as upper and lower layers move in the opposite direction for two-way exchange flows. Hence, the frictional parameter α alone tends to underestimate the dynamic channel length, since interfacial friction is not included in this parameterisation scheme. Take the Burlington Ship Canal ($\alpha = 0.23$ and $f_r = 0.39$) for example, the frictional exchange flow solution predicts an exchange flow rate of $G_o = 0.70$. This corresponds to a 30% drop in the exchange flow rate from the inviscid exchange flow solution, even though a channel with $\alpha = 0.23$ might otherwise be considered short enough to ignore frictional effects.

Previous field and laboratory studies on exchange flows indicated that density interfaces are nearly linear throughout most of the channel length, and are curved at each end of the channel. The assumption, that the density interface follows a straight line linking two hydraulic controls, has been widely used in previous frictional exchange flow analysis. Given the pronounced non-linear nature of exchange flow problems, however, this assumption may not be appropriate. The resulting interface profile equation exhibits little

linearity in the strict mathematical sense. The interface profile is not only non-linear, but also non-symmetric in nature due to the fact that bottom friction is included, but surface friction is assumed to be absent. As a result, the density interface tends to be more curved near the exit on the left end of the channel.

Several areas covered in this thesis deserve further investigation. First, an improvement in evaluation of the interfacial frictional factor is needed. This would require a more comprehensive understanding of the dynamics of stratified shear flows. Second, the influence of barotropic forcing needs to be incorporated into the theoretical analysis of a more general exchange flow problem. Ultimately, the exchange between two water bodies is a combined result of two forces, the internal pressure gradient due to density contrasts (baroclinic) and the surface pressure difference due to water level difference (barotropic). More detailed studies on each subject are recommended for future research.

APPENDIX A

GENERAL SOLUTIONS FOR MAXIMAL TWO-LAYER EXCHANGE FLOWS

A.1 MAXIMAL EXCHANGE FLOW THROUGH A WIDE CHANNEL

A.1.1 Interface Profile

The equation of motion for two-layer open channel exchange flows, as derived in Chapter 3, is as following:

$$\frac{dy_2}{d\chi} = \frac{\alpha G_o^2 (y_1^3 + f_r)}{32 y_1^3 y_2^3 - 2G_o^2 (y_1^3 + y_2^3)}. \tag{3-34}$$

Re-arranging terms in (3-34) and applying integration to both sides of the equation yield:

$$\int \alpha G_o^2 d\chi = \int \frac{32 y_1^3 y_2^3 - 2G_o^2 (y_1^3 + y_2^3)}{(y_1^3 + f_r)} dy_2. \tag{3-35}$$

It is obvious that using y_1 as the independent variable in (3-35) would lead to a much simpler form in the denominator, and hence easier integration procedure. Hence, the rigid lid condition (i.e. $y_2 = 1 - y_1$) is substituted into (3-35), which, and after some manipulations, eventually yields to the following equation:

$$\int \alpha G_o^2 d\chi = \int \frac{32 y_1^6 - 96 y_1^5 + 96 y_1^4 - 32 y_1^3 + 6G_o^2 y_1^2 - 6G_o^2 y_1 + 2G_o^2}{(f_r + y_1^3)} dy_1 = \sum_{i=1}^{7} \phi_i, \tag{A-1}$$

where $\phi_1 = -32(f_r + 1)\int dy_1$,

$\phi_2 = 96\int y_1 dy_1$,

$\phi_3 = -96\int y_1^2 dy_1$,

$$\phi_4 = 32\int y_1^3 dy_1,$$

$$\phi_5 = \left[2\left(G_o^2 + f_r\right)\left(1 + f_r^{-1/3} + \tfrac{1}{3} f_r^{-2/3}\right) + \tfrac{2}{3} f_r^{4/3}\right]\int \frac{1}{\left(y_1 + f_r^{1/3}\right)} dy_1,$$

$$\phi_6 = -\left[2\left(G_o^2 + f_r\right)\left(f_r^{1/3} + 1 - \tfrac{2}{3} f_r^{-1/3}\right) - \tfrac{4}{3} f_r^{5/3}\right]\int \frac{1}{\left(y_1^2 - f_r^{1/3} y_1 + f_r^{2/3}\right)} dy_1,$$

$$\phi_7 = \left[2\left(G_o^2 + f_r\right)\left(2 - f_r^{-1/3} - \tfrac{1}{3} f_r^{-2/3}\right) - \tfrac{2}{3} f_r^{4/3}\right]\int \frac{y_1}{\left(y_1^2 - f_r^{1/3} y_1 + f_r^{2/3}\right)} dy_1.$$

Integrating (A-1) and subsequently substituting $y_1 = \frac{1}{2} - \eta$ into the resulting equation lead to the following density interface profile equation:

$$\alpha G_o^2 \chi = a_1\eta + a_2\eta^2 + a_3\eta^3 + a_4\eta^4 + a_5 \ln\left(-\eta + f_r^{1/3} + \tfrac{1}{2}\right) + a_6 \ln\left[\eta^2 + \left(f_r^{2/3} - 1\right)\eta + \tfrac{1}{2} f_r^{2/3} + \tfrac{1}{4}\right] +$$
$$+ a_7 \tan^{-1}\left[\frac{-2\eta - f_r^{1/3} + 1}{f_r^{1/3}\sqrt{3}}\right] + a_o, \qquad \text{(A-2)}$$

where $a_1 = 4\left(8 f_r + 1\right)$,

$a_2 = 12$,

$a_3 = 16$,

$a_4 = 8$,

$a_5 = \left[G_o^2\left(1 + f_r^{-1/3} + \tfrac{1}{3} f_r^{-2/3}\right) + \tfrac{16}{3} f_r^{1/3}\left(f_r^{1/3} + 1\right)^3\right]$,

$a_6 = \left[G_o^2\left(2 - f_r^{-1/3} - \tfrac{1}{3} f_r^{-2/3}\right) - 16 f_r^{1/3}\left(\tfrac{1}{3} f_r - 2 f_r^{2/3} + f_r^{1/3} + \tfrac{1}{3}\right)\right]$,

$a_7 = \frac{2}{\sqrt{3}}\left[G_o^2\left(-3 f_r^{-1/3} + f_r^{-2/3}\right) + 16 f_r^{1/3}\left(f_r - 3 f_r^{1/3} + 1\right)\right]$,

a_o is the constant of integration.

A.1.2 Solutions Curves of f_o and f_1

To obtain the two solution curves, substituting $\eta = \eta_o$ at $\chi = 0$ and $\eta = \eta_1$ at $\chi = 1$ into the interface equation of (A-2) respectively, and then subtracting the two resulting equations to eliminate the integration constant a_o lead to:

$$\begin{aligned}\alpha G_o^2 = {} & a_1(\eta_1 - \eta_o) + a_2(\eta_1^2 - \eta_o^2) + a_3(\eta_1^3 - \eta_o^3) + a_4(\eta_1^4 - \eta_o^4) + a_5\left[\ln\left(-\eta_1 + f_r^{1/3} + \tfrac{1}{2}\right) - \ln\left(-\eta_o + f_r^{1/3} + \tfrac{1}{2}\right)\right] \\ & + a_6\left\{\ln\left[\eta_1^2 + \left(f_r^{2/3} - 1\right)\eta_1 + \tfrac{1}{2} f_r^{2/3} + \tfrac{1}{4}\right] - \ln\left[\eta_o^2 + \left(f_r^{2/3} - 1\right)\eta_o + \tfrac{1}{2} f_r^{2/3} + \tfrac{1}{4}\right]\right\} + \\ & + a_7\left\{\tan^{-1}\left[\frac{-2\eta_1 - f_r^{1/3} + 1}{f_r^{1/3}\sqrt{3}}\right] - \tan^{-1}\left[\frac{-2\eta_o - f_r^{1/3} + 1}{f_r^{1/3}\sqrt{3}}\right]\right\}. \end{aligned} \qquad \text{(A-3)}$$

Finally, substituting η_1 with $-\eta_o$ in (A-3) and rearranging terms lead to the solution curve at $\chi = 0$, i.e. $f_o\left(G_o^2, \eta_o, \alpha, f_r\right)$:

$$G_o^2 = \frac{-8(8f_r + 1)\eta_o - 32\eta_o^3 + \frac{32}{3} f_r^{1/3}\left(1 + f_r^{1/3}\right)^3 \phi_1 - 16 f_r^{1/3}\left(\frac{1}{3} f_r - 2 f_r^{2/3} + f_r^{1/3} + \frac{1}{3}\right)\phi_2 + \frac{32}{\sqrt{3}} f_r^{1/3}\left(f_r - 3 f_r^{1/3} + 1\right)\phi_3}{\alpha - 2\left(1 + f_r^{-1/3} + \frac{1}{3} f_r^{-2/3}\right)\phi_1 - \left(2 - f_r^{-1/3} - \frac{1}{3} f_r^{-2/3}\right)\phi_2 + \frac{2}{\sqrt{3}}\left(3 f_r^{-1/3} - f_r^{-2/3}\right)\phi_3}, \qquad \text{(A-4a)}$$

where $\phi_1 = \ln\left[\dfrac{\eta_o + f_r^{1/3} + \frac{1}{2}}{-\eta_o + f_r^{1/3} + \frac{1}{2}}\right]$,

$$\phi_2 = \ln\left[\frac{\eta_o^2 - \left(f_r^{1/3} - 1\right)\eta_o + \frac{1}{2} f_r^{1/3} + \frac{1}{4}}{\eta_o^2 + \left(f_r^{1/3} - 1\right)\eta_o + \frac{1}{2} f_r^{1/3} + \frac{1}{4}}\right],$$

$$\phi_3 = \tan^{-1}\left[\frac{4\sqrt{3} f_r^{1/3}\eta_o}{-4\eta_o^2 + 4 f_r^{2/3} - 2 f_r^{1/3} + 1}\right].$$

Similarly, substituting η_o with $-\eta_1$ in (A-3) and rearranging terms lead to the solution curve at $\chi = 1$, i.e. $f_1\left(G_o^2, \eta_1, \alpha, f_r\right)$:

$$G_o^2 = \frac{8(8f_r + 1)\eta_1 + 32\eta_1^3 + \frac{32}{3} f_r^{1/3}\left(1 + f_r^{1/3}\right)^3 \phi_1 - 16 f_r^{1/3}\left(\frac{1}{3} f_r - 2 f_r^{2/3} + f_r^{1/3} + \frac{1}{3}\right)\phi_2 + \frac{32}{\sqrt{3}} f_r^{1/3}\left(f_r - 3 f_r^{1/3} + 1\right)\phi_3}{\alpha - 2\left(1 + f_r^{-1/3} + \frac{1}{3} f_r^{-2/3}\right)\phi_1 - \left(2 - f_r^{-1/3} - \frac{1}{3} f_r^{-2/3}\right)\phi_2 - \frac{2}{\sqrt{3}}\left(3 f_r^{-1/3} - f_r^{-2/3}\right)\phi_3}, \qquad \text{(A-4b)}$$

where $\phi_1 = \ln\left[\dfrac{-\eta_1 + f_r^{1/3} + \frac{1}{2}}{\eta_1 + f_r^{1/3} + \frac{1}{2}}\right]$,

$$\phi_2 = \ln\left[\frac{\eta_1^2 + \left(f_r^{1/3} - 1\right)\eta_1 + \frac{1}{2} f_r^{1/3} + \frac{1}{4}}{\eta_1^2 - \left(f_r^{1/3} - 1\right)\eta_1 + \frac{1}{2} f_r^{1/3} + \frac{1}{4}}\right],$$

$$\phi_3 = \tan^{-1}\left[\frac{-4\sqrt{3} f_r^{1/3}\eta_1}{-4\eta_1^2 + 4 f_r^{2/3} - 2 f_r^{1/3} + 1}\right].$$

A.2 MAXIMAL EXCHANGE FLOW THROUGH A WIDE CULVERT

A.2.1 Interface Profile

The equation of motion for two-layer exchange flow through a wide culvert:

$$\frac{dy_2}{d\chi} = \frac{\alpha G_o^2 (f_r + y_1^3 + y_2^3)}{32 y_1^3 y_2^3 - 2G_o^2 (y_1^3 + y_2^3)}. \tag{3-42}$$

Re-arranging terms and applying integration to both sides of (3-42) yield:

$$\int \alpha G_o^2 d\chi = \int \frac{32 y_1^2 y_2^3 - 2G_o^2\left(y_1^3 + y_2^3\right)}{\left(y_1^3 + y_2^3 + f_r\right)} dy_2 \tag{3-43}$$

Manipulating the right hand side of (3-43) leads to:

$$\int \alpha G_o^2 d\chi = \int \frac{32 y_1^2 y_2^3 - 2G_o^2\left(y_1^3 + y_2^3\right)}{\left(y_1^3 + y_2^3 + f_r\right)} dy_2 = \sum_{i=1}^{4} \phi_i, \tag{A-5}$$

where $\phi_1 = -2\left[G_o^2 + \dfrac{16\left(f_r + 1\right)^2}{27}\right]\int dy_2$

$$\phi_2 = -\frac{32\left(f_r + 1\right)}{9}\int \left(y_1 y_2\right) dy_2 = -\frac{32\left(f_r + 1\right)}{9}\int y_2\left(1 - y_2\right) dy_2$$

$$\phi_3 = -\frac{32}{3}\int y_1^2 y_2^2 dy_2 = -\frac{32}{3}\int \left(1 - y_2\right)^2 y_2^2 dy_2 ,$$

$$\phi_4 = 2\left[f_r G_o^2 + \frac{16(f_r+1)^3}{27}\right]\int \frac{1}{-3y_1 y_2 + f_r + 1} dy_2$$

$$= 2\left[f_r G_o^2 + \frac{16(f_r+1)^3}{27}\right]\int \frac{1}{-3y_2(1-y_2) + f_r + 1} dy_2 \,.$$

Integrating (A-5) and substituting $y_2 = \frac{1}{2} + \eta$ into the resulting equation then lead to the expression of lower layer depth or the density interface profile equation:

$$\alpha G_o^2 \chi = a_1\eta + a_2\eta^3 + a_3\eta^5 + a_4 \tan^{-1}\left[\frac{6\eta}{\sqrt{12f_r+3}}\right] + a_o, \qquad \text{(A-6)}$$

where $a_1 = -\frac{2}{27}\left(27G_o^2 + 16f_r^2 + 44f_r + 37\right)$,

$$a_2 = \frac{16}{27}(2f_r + 5),$$

$$a_3 = -\frac{32}{15},$$

$$a_4 = \frac{4\left[27f_r G_o^2 + 16(f_r+1)^3\right]}{27\sqrt{12f_r+3}},$$

a_o is the constant of integration.

The symmetric nature of culvert exchange flow leads to $\eta_\chi = -\eta_{1-\chi}$. Hence, $\eta_{\chi=0.5} = 0$. Substituting $\eta = 0$ at $\chi = 0.5$ into the interface profile equation of (A-6) and solving for the constant of integration a_o yield:

$$a_o = \tfrac{1}{2}\alpha G_o^2 \,. \qquad \text{(A-7)}$$

A.2.2 Solution Curves of f_o and f_1

Substituting $\eta = \eta_o$ at $\chi = 0$ into the interface profile equation of (A-6) and rearranging terms leads to solution curve at $\chi = 0$, i.e. $f_o\left(G_o^2, \eta_o, \alpha, f_r\right)$:

$$G_o^2 = \frac{-\frac{2}{27}\left(16f_r^2+44f_r+37\right)\eta_o+\frac{16}{27}\left(2f_r+5\right)\eta_o^3-\frac{32}{15}\eta_o^5+\frac{64\left(f_r+1\right)^3}{27\sqrt{12f_r+3}}\tan^{-1}\left[\frac{6\eta_o}{\sqrt{12f_r+3}}\right]}{-\frac{\alpha}{2}+2\eta_o-\frac{4f_r}{\sqrt{12f_r+3}}\tan^{-1}\left[\frac{6\eta_o}{\sqrt{12f_r+3}}\right]}. \qquad \text{(A-8a)}$$

Similarly, substituting $\eta=\eta_1$ at $\chi=1$ into the interface profile equation of (A-6) and rearranging terms leads to solution curve at $\chi=1$, i.e. $f_1\left(G_o^2,\eta_1,\alpha,f_r\right)$:

$$G_o^2 = \frac{-\frac{2}{27}\left(16f_r^2+44f_r+37\right)\eta_1+\frac{16}{27}\left(2f_r+5\right)\eta_1^3-\frac{32}{15}\eta_1^5+\frac{64\left(f_r+1\right)^3}{27\sqrt{12f_r+3}}\tan^{-1}\left[\frac{6\eta_1}{\sqrt{12f_r+3}}\right]}{\frac{\alpha}{2}+2\eta_1-\frac{4f_r}{\sqrt{12f_r+3}}\tan^{-1}\left[\frac{6\eta_1}{\sqrt{12f_r+3}}\right]}. \qquad \text{(A-8b)}$$

The above two solution curves and the hydraulic control equation are solved for each of the three unknowns (η_o, η_1 and G_o^2) for any given frictional parameters α and f_r. The solutions to the maximal exchange flow problem can be obtained graphically, as presented on the $G_o^2-\eta$ plane. Alternatively, the solutions can be obtained using the iteration process described in Appendix B.

APPENDIX B

NUMERICAL PROCEDURES

The hydraulic control condition and the two solution curves are solved for each of the three unknowns (i.e. η_o, η_1 and G_o^2) in maximal exchange flow problems for any given frictional parameters α and f_r. As discussed previously in Chapter 3, solutions to maximal exchange flows can be conveniently displayed on the $G_o^2 - \eta$ plane. The presentation of maximal exchange solutions on the $G_o^2 - \eta$ plane provides a method to solve the problem graphically. Alternatively, the solutions can also be sought through the iteration procedure described below.

Re-write the critical conditions at either end of the channel for the maximal exchange flow in the following non-dimensional form:

$$G^2 = \frac{G_o^2}{16(\frac{1}{2} - \eta_j)^3} + \frac{G_o^2}{16\left(\frac{1}{2} + \eta_j\right)^3} = 1, \quad \text{at } \chi = 0, 1, \qquad (3\text{-}38)$$

where G_o^2 is the composite Froude number throughout the channel in the absence of friction, and η_j ($j = 0, 1$) is interface deflection at either end of the channel respectively. The left end ($\chi = 0$) and right end ($\chi = 1$) of the channel are identified by $j = 0$ and $j = 1$ respectively.

When solving maximal exchange problems in an iterative way, it is more preferred to express the interface deflection at both ends of the channel, η_o and η_1, as functions of G_o^2 in the hydraulic control condition of (3-38). Re-arranging terms in (3-38) yields:

$$\eta_j^6 - \frac{3}{4}\eta_j^4 + \frac{3}{16}\left(G_o^2 + 1\right)\eta_j^2 + \frac{1}{64}\left(G_o^2 - 1\right) = 0. \qquad (B\text{-}1)$$

Substituting $\eta_j^2 = \omega + \frac{1}{4}$ into (B-1) leads to:

$$\omega^3 + \frac{3G_o^2}{16}\omega + \frac{G_o^2}{16} = 0. \qquad \text{(B-2)}$$

It is noted that equation (B-2) has one real root and two imaginary roots. The only real root to the equation is solved as following:

$$\omega = \frac{1}{2}\left[\sqrt{\left(\frac{G_o^2}{4}\right)^3 + \left(\frac{G_o^2}{4}\right)^2} - \frac{G_o^2}{4}\right]^{1/3} - \frac{1}{2}\left[\sqrt{\left(\frac{G_o^2}{4}\right)^3 + \left(\frac{G_o^2}{4}\right)^2} + \frac{G_o^2}{4}\right]^{1/3}. \qquad \text{(B-3)}$$

By definition,

$$\eta_j = \pm\sqrt{\omega + \tfrac{1}{4}},$$

where $j = 0, 1$.

By convention, the more dense water moves from right to left in the lower layer and the less dense water moves from left to right in the upper layer. Therefore, $\eta_1 \geq \eta_o$. Hence:

$$\begin{matrix}\eta_1 \\ \eta_o\end{matrix} = \pm\sqrt{\omega + \tfrac{1}{4}} = \pm\left(\frac{1}{2}\left[\sqrt{\left(\frac{G_o^2}{4}\right)^3 + \left(\frac{G_o^2}{4}\right)^2} - \frac{G_o^2}{4}\right]^{1/3} - \frac{1}{2}\left[\sqrt{\left(\frac{G_o^2}{4}\right)^3 + \left(\frac{G_o^2}{4}\right)^2} + \frac{G_o^2}{4}\right]^{1/3} + \frac{1}{4}\right)^{1/2}. \qquad \text{(B-4)}$$

The hydraulic control equation of (B-4) and the two solution curves, as defined in (A-4) and (A-8) for open channel and culvert exchange flows respectively, are solved for each of the three unknowns (G_o^2, η_o and η_1) through the following simple iteration steps:

(1) For any given frictional parameters of a and f_r, the iteration process starts with an initial guessing value of G_o^2 ($0 \leq G_o^2 \leq 1$).

(2) Solve for η_0 or η_1 from the hydraulic control condition of (B-4), using the previously obtained G_o^2 value.

(3) Solve for a new value of G_o^2 from solution curves of $f_o\left(G_o^2, \eta_o, \alpha, f_r\right)$ or $f_1\left(G_o^2, \eta_1, \alpha, f_r\right)$, using η_0 or η_1 value calculated in step (2). This finishes one round of iteration process.

(4) Repeat steps (2) and (3). The iteration process continues until $\left(\eta_j^{i+1} - \eta_j^i\right)$ or $\left(G_o^{2^{i+1}} - G_o^{2^i}\right) < \theta$, where η_j^i ($j = 0, 1$) and $G_o^{2^i}$ are intermediate iteration values of η_j and G_o^2 at the i^{th} iteration respectively, and θ is a predetermined error tolerant criteria.

For maximal open channel exchange flows, the obtained solutions for η_0, η_1 and G_o^2 are substituted into the density interface equation of (A-2) to solve for the integration constant a_0. This will lead to a uniquely defined interface profile for the maximal exchange flow under any given frictional parameters of a and f_r.

BIBLIOGRAPHY

Abraham, G. & Eysink, W. D. (1971). "Magnitude of interfacial shear in exchange flow." *J. of Hydr. Res.*, **9(2)**, 125-151.

Abraham, G., Karelse, M. & Van Os, A.G. (1979). "On the magnitude of interfacial shear of subcritical stratified flows in relation with internal stability." *J. of Hydr. Res.*, **17(4)**, 273-287.

Anati, D. A. Assaf, G. & Thompson, R. (1977). "Laboratory models of sea straits." *J. Fluid Mech.*, **81**, 341-351.

Arita, M. & Jirka, G. H. (1987). "Two-layer model of saline wedge. I: Entrainment and interfacial friction." *J. of Hydr. Engrg.*, ASCE, **113(10)**, 1229-1247.

Armi, L. (1986). "The hydraulics of two flowing layers of different densities." *J. Fluid Mech.*, **163**, 27-58.

Armi, L. & Farmer, D. M. (1987). "A generalization of the concept of maximal exchange in a strait." *J. Geophysical Res.*, **92(13)**, 14679-14680.

Armi, L. & Farmer, D. M. (1986). "Maximal two-layer exchange through a contraction with barotropic net flow." *J. Fluid Mech.*, **164**, 27-51.

Armi, L. & Farmer, D. M. (1988) "The flow of Mediterranean water through the Strait of Gibraltar", *Progress in Oceanography*, **21**, 1-105.

Assaf, G. & Hecht, A. (1974). "Sea strait: a dynamic model." *Deep-Sea Res.*, **21**, 947-958.

Baines, P. G. (1984). "A unified description of two-layer flow over topography." *J. Fluid Mech.*, **146**, 127-167.

Barica, J., Charlton, M.N., Poulton, D.J., and Kholi, B. (1987). "Water exchange between Lake Ontario and Hamilton Harbour: water quality implications." *Proc. of Int'l Symposium on Functional and Structural Properties of Large Lakes,* Konstanz, Germany, Sept., 1987, 13-18.

Bormans, M. & Garrett, C. (1989a). "The effect of rotation on the surface inflow through the Strait of Gibraltar." *J. of Physical Oceanography*, **19(10)**, 1535-1542.

Bormans, M. & Garrett, C. (1989b). "The effects of nonrectangular cross section, friction, and barotropic fluctuations on the exchange through the Strait of Gibraltar." *J. of Physical Oceanography*, **19(10)**, 1543-1557.

Bowden, K.F. & Fairbairn, L.A. (1952) "A determination of the frictional forces in a tidal current." *Proceedings of the Royal Society*, **A(214)**, 371-392.

Browand, F.K. & Winant, C.D. (1973). "Laboratory observations of shear-layer instability in stratified fluid." *Boundary-Layer Meterology*, **5**, 67-77.

Chow, V. T. (1959). "Open channel hydraulics." McGRAW-Hill Book Company, 1959.

Cheung, E.A. & Lawrence, G. A. (1991) "Frictional exchange through a contraction." *Proc. 1991 Annu Conf. of CSCE.*

Dalziel, S. B. (1988). "Two-layer hydraulics: Maximal exchange flows." *Ph.D. thesis,* University of Cambridge, Cambridge, England.

Dalziel, S. B. (1991). "Two-layer hydraulics: a functional approach." *J. Fluid Mech.,* **223**, 135-163.

Defant, A. (1961). "Physical Oceanography." **1**, Pergamon Press.

Dermissis, V. & Partheniades, E. (1984). "Interfacial resistance in stratified flows." *J. wtrwy., Port, Coast. and Oc. Engrg.,* ASCE, **110(2)**, 231-250.

Dermissis, V. & Partheniades, E. (1985). "Dominant shear stresses in arrested saline wedges." *J. wtrwy., Port, Coast. and Ocean Engrg.,* ASCE, **111(4)**, 733-752.

Dick, T. M. & Marsalek, J. (1972). "Thermal wedge between Lake Ontario and Hamilton Harbour." *Proc. 15th Conf. Great Lakes Res.*, 536-543.

Dick, T. M. & Marsalek, J. (1973a). "Interfacial shear stress in density wedges." *Proc. 1st Canadian Hydraulic Conf.,* 176-189.

Dick, T. M. & Marsalek, J. (1973b). "Exchange flow between Lake Ontario and Hamilton Harbour." *Environment Canada Scientific Series No. 36.* Inland Waters Directorate, Canada Center for Inland Waters, Burlington, Ontario.

Farmer, D. & Armi, L. (1986). "Maximal two-layer exchange over a sill and through the combination of a sill and contraction with barotropic flow." *J. Fluid Mech.,* **164**, 53-76.

Freeman, N. G., Hamblin, P. F., and Murthy, T. S. (1974). "Helmholz resonance in harbours of great lakes." *Proc. 17th Conf. Great Lakes Res.*, 399-411.

Georgiev, B. V. (1972). "Some experimental investigation on turbulent characteristics of stratified flows." *Proc. 1st Int. Symp. on Stratified Flows,* Novosibirsk, U.S.S.R., 507-515.

Georgiev, B. V. (1990). "On the interface phenomena in two-layer stratified flow." *Proc. Int. Conf. on Physical Modeling of Transport and Dispersion,* MIT, 4B.7-12.

Gorrie, P. (1987). "Cleaning up Hamilton Harbour." *Canadian Geographic*, **107**, 34-45.

Goldstein, S. (1931). "On the stability of superposed streams of fluids of different densities." *Proc. of the Royal Society of London*, **A132**, 524-548.

Grant, W.D., Williams, A.J. & Glenn, S.M. (1984) " Bottom stress estimates and their prediction on the northern California continental shelf during CODE-1: The importance of wave–current interaction." *J. Physical Oceanography*, **16**, 489-648.

Greco, S.L. (1998) "Two-layer exchange flow through the Burliington Ship Canal." *M.A.Sc. Thesis*, Univ. of British Columbia.

Gregg, M. & Ö zsoy, E. (2000) "Mixing and hydraulics in the Bosphorus exchange flow." *Proc. 5th Int. Symp. on Stratified Flows,* Vancouver, Canada, 537-542.

Hamblin, P. F. (1996). "Exchange flows in lakes." Coastal and estuarine studies: Physical processes in lakes and oceans, **54**, 187-198.

Hamblin, P. F. & Lawrence, G. A. (1990). "Exchange flows between Hamilton Harbour and Lake Ontario." *Proc. 1990 Annu Conf. of CSCE*, V, 140-148.

Harleman, D. R. F. & Stolzenbach, K. D. (1972). "Fluid mechanics of heat disposal from power generation." *Annu Rev. of Fluid Mech.*, **4**, 7-32.

Harris, G. P., Piccinin, B.B., Haffner, G.D., Snodgrass, W., and Polak, J. (1980). "Physical variability and phytoplankton communities: the descriptive limnology of Hamlton Harbour." *Arch Hrdrobiol.*, **88**, 303-327.

Head, M. J. (1983). "The use of miniture four-electrode conductivity probes for high resolution mesurement of turbulent density or temperature variation in salt-stratified flows", *PhD Thesis*, Univ. of Calif., San Diego.

Helfrich, K. R. (1995). "Time-dependent two-layer hydraulic exchange flows", *J. of Physical Oceanography*, **25(3)** 359-373.

Henderson, F.M. (1966). "Open channel flow." MacMillan.

Hino, M. (1980). "Entrainment and friction at the interface of salt wedge." *Proc. 2nd Int. Symp. on Stratified Flows,* Trondheim, Norway, 763-782.

Holley, E. R. & Waddell, K. M. (1976). "Stratified flow in Great Salt Lake culvert", *J. Great Lake Res.*, **11**, 43-52.

Ippen, A. T. & Harleman, D. R. F. (1952). "Steady state characteristics of subsurface flows." Circular No. 521, *U.S. Dept. of Commerce National Bureau of Standards*, 79-93.

Iwasaki, T. (1964). "On the shear stress at the interface and its effects in the stratified flow." *Coastal Engineering, Proc. 9th Coastal Engineering Conf.*, Lisbon, Portgal, 879-892.

Keulegan, G. (1966). "The mechanism of an arrested saline wedge." *Estuary and Coastal Hydrodynamics*, Chapter. 11, A.T. Ippen, Ed., McGraw Hill Book Co., New York, N.Y., 546-574.

Klapwijk, A. & Snodgrass, W. J. (1985). "Model for lake-bay exchange flow." *J. Great Lakes Res.*, **11(1)**, 43-52.

Kohli, B. (1979). "Mass exchange between Hamilton Harbour and Lake Ontario." *J. Great Lakes Res.*, **5(1)**, 36-44.

Kohli, B. (1984). "Hamilton Harbour physical characteristics." *Great Lake Section, Water Resources Branch, Ontario Ministry of the Environment, Toronto, Ontario.*

Koop, C.G. & Browand, F.K. (1979). "Instability and turbulence in a stratified fluid with shear." *J. Fluid Mech.*, **93**, 135-159.

Kraus, N. C., Lohrmann, A. & Cabrera, R. (1994). "New acoustic meter for measuring 3D laboratory flows." *J. of hydraulic engineering*, **120(3)**, 406-412.

Lawrence, G. A. (1990). "On the hydraulics of Boussinesq and non-Boussinesq two-layer flows." *J. Fluid Mech.*, **215**, 457-480.

Lawrence, G. A. (1993). "The hydraulics of steady two-layer flow over a fixed obstacle." *J. Fluid Mech.*, **254**, 605-633.

Lawrence, G.A., Haigh, S.P. and Zhu, Z. (1998). "In search of Holmboe instabilities." *Physical Processes in Lakes and Oceans. Coastal and Estuarine Studies*, **54**, 295-304.

Lock, R.C. (1951). "The velocity distribution in the laminar boundary layer between parallel streams." *Quart. J. Appl. Math.*, **4**, 42-63.

Lofquist, K. (1960). "Flow and stress near an interface between stratified liquids." *Phys. of Fluid*, **3(2)**, 158-174.

Lohrmann, A., Cabrera, R. & Kraus, N. C. (1994) "Acoustic-Doppler velocimeter for laboratory use." *Proc. on Fundamentals and Advancements in Hydraulic Measurements and Exprimentation*, ASCE, Buffalo, New York.

Long, R. R. (1954). "Some aspects of the flow of stratified fluids II: Experiments with two-fluids." *Tellus*, **6**, 97-115.

Long, R. R. (1956). "Long waves in a two-fluid system." *J. of Met.*, **13**, 70.

Long, R. R. (1974). "Some experimental observations of upstream disturbances in a two-fluid system." *Tellus*, **26**, 313-317.

Macagno, E. O. & Rouse, H. (1962) "Interfacial mixing in stratified flow." *Trans. of ASCE*, **127(1)**, 102-128.

Maderich, V. S. & Efroimson, V. O. (1990). "Theory for water exchange across a strait." *Oceanology*, **30(4)**, 415-420.

Maderich, V. S. & Efroimson, V. O. (1990). "A simple model of a sea with a strait." *Oceanology*, **26(3)**, 300-304.

Maderich, V.S. & Oleksiuk, V.V. (1994). "Laboratory experiments on two-layer exchange through long straits." *Proc. of 4th Int. Conf. on Stratified Flow,* Grenoble, France.

Oguz, T., Ö zsoy, E., Latif, M. A. Sur, H.I. and Unluata, U. (1990). "Modeling of hydraulically controlled exchange flow in the Bosphorus strait." *J. of Physical Oceanography*, **20(7)** 945-965.

Ottesen-Hansen, N. E. & Moller, J. S. (1990). "Zero blocking solution for the Great Belt Link." *The Physical Oceanography of Sea Straits*. Pratt, L. J. (editor), Kluwer Academic Publishers. 153-170.

Palmer, M. D. & Poulton, D. J. (1976). "Hamilton Harbour: Periodicities of the physicochemical process." *Limnol. Oceanog.*, **21**, 118-127.

Partheniades, E. & Dermissis, V. (1993) "Laboratory experimental study on the interfacial shear stresses and velocity distribution in arrested saline wedges." *Modeling, measuring and prediction, Int. Conf. on Water Pollution II*, 417-424.

Pederson, B. (1980). "A monograph on turbulent entrainment and friction in the two-layer stratified flow." *Tech. Report, Tech. Univ. Denmark*, **25**.

Polak, J. & Haffner, G. D. (1978). "Oxygen depletion of Hamilton Harbour." *Water Research*, **12**, 205-215.

Pond, S. (1968). "Some effects of buoy motion on measurements of wind speed and stress." *J. Geophys. Res.*, **73**, 507-512.

Pratt, L. J. (1986). "Hydraulic control of sill flow with bottom friction." *J. Physical Oceanography*, **16(11)**, 1970-1980.

Sargent, F. E. & Jirka, G. H. (1987). "Experiments on saline wedge." *J. of Hydr. Engrg.*, ASCE, **113(10)**, 1307-1324.

Schijf, J. B. & Schönfeld, J. C. (1953). "Theoretical considerations on the motion of salt and fresh water." *Proc. of the Minn. Int. Hyd. Conv.*, 321-333.

Schwartz, R. A. & Imberger, J. (1988). "Flushing behaviour of a coastal marina", *Proc. 21 International Conf. on Coastal Engineering*, Torremolinas, Spain, 2626-2640.

Shi-Igai, H. (1965). "On the resistance Coefficient at the interface between salt and fresh water." *Trans. JSCE*, **123**, 27-31.

Spigel, R. H. (1989). "Some aspects on the physical limnology of Hamilton harbour." *Environ. Can. NWRI Contribution* No. 89-08.

Stevens, C. & Coates, M. J. (1994). "Applications of a maximized cross-correlation technique for resolving velocity fields in laboratory experiments." *J. of Hydr. Res.*, **32(2)**, 195-212.

Stigebrandt, A. (1977). "On the effects of barotropic current fluctuations on the two-layer transport capacity of a constriction." *J. of Physical Oceanography,* **7(1)**, 118-122.

Stommel, H. & Farmer, H. G. (1952). "Control of salinity in an estuary by a transition." *J. Mar. Res.* **11(2)**, 205-214.

"Standard method for examination of water and waste water", 18th edition, *APHA, AWWA, WEF*, APHA Washington D.C., 1992, Greenberg, A. E., Clesceri, L. S. & Eaton, A. D. (editor).

Tamai, N. (1976). "Friction at the interface of two-layered flows." *Coastal Engineering*, 3169-3189.

Tedford, E.W. (1999) "Exchange flow through the Burliington Ship Canal." *M.A.Sc. Thesis*, Univ. of British Columbia.

Taylor, G.I. (1931). "Effect of variation in density on stability of superposed streams of fluids." *Proc. of the Royal Society of London*, **A132**, 499-523.

Turner, J. S. (1973). "Buoyancy effects in fluids." Cambridge Univ. Press.

Watson, G. (1994). "Internal waves in a stratified shear flow: the Strait of Gibraltar." *J. of Physical Oceanography,* **24**, 509-517.

Webster, C.A.G. (1964). "An experimental study of turbulence in a density stratified shear flow." *J. Fluid Mech.,* **19**, 221-226.

White, F.M. (1991). "Viscous fluid flow." McGraw-Hill, Inc.

Wood, I. R. (1970). "A lock exchange flow." *J. Fluid Mech.,* **42**, 671-687.

Wood, I. R. & Lai, K. K. (1972). "Flow of layered fluid over broad crest weir." *J. of Hydr. Engrg.*, ASCE, **98,** 87-104.

Yonemitsu, N., Swaters, G.E., Rajaratnam, N. & Lawrence, G.A. (1996). "Shear instabilities in arrested salt-wedge flows." *Dynamics Atmospheres. and Ocean,* **24**, 173-182.

Zhu, Z. (1996). "Exchange flow through a channel with an underwater sill", *PhD Thesis*, Univ. of British Columbia.

Zhu. Z. & Lawrence, G. A. (1996). "Exchange flow through a channel with an underwater sill." *Dynamics Atmospheres. and Ocean,* **24**, 153-161.

Zhu. D. Z. & Lawrence, G. A. (1998). "Non-hydrostatic effects in layered shallow water flows." *J. Fluid Mech.,* **355**, 1-16.

Zhu, D. Z. & Lawrence, G. A. (2000). "Hydraulics of exchange flows." *J. of Hydr. Engrg.*, ASCE, **126(12)**, 921-928.

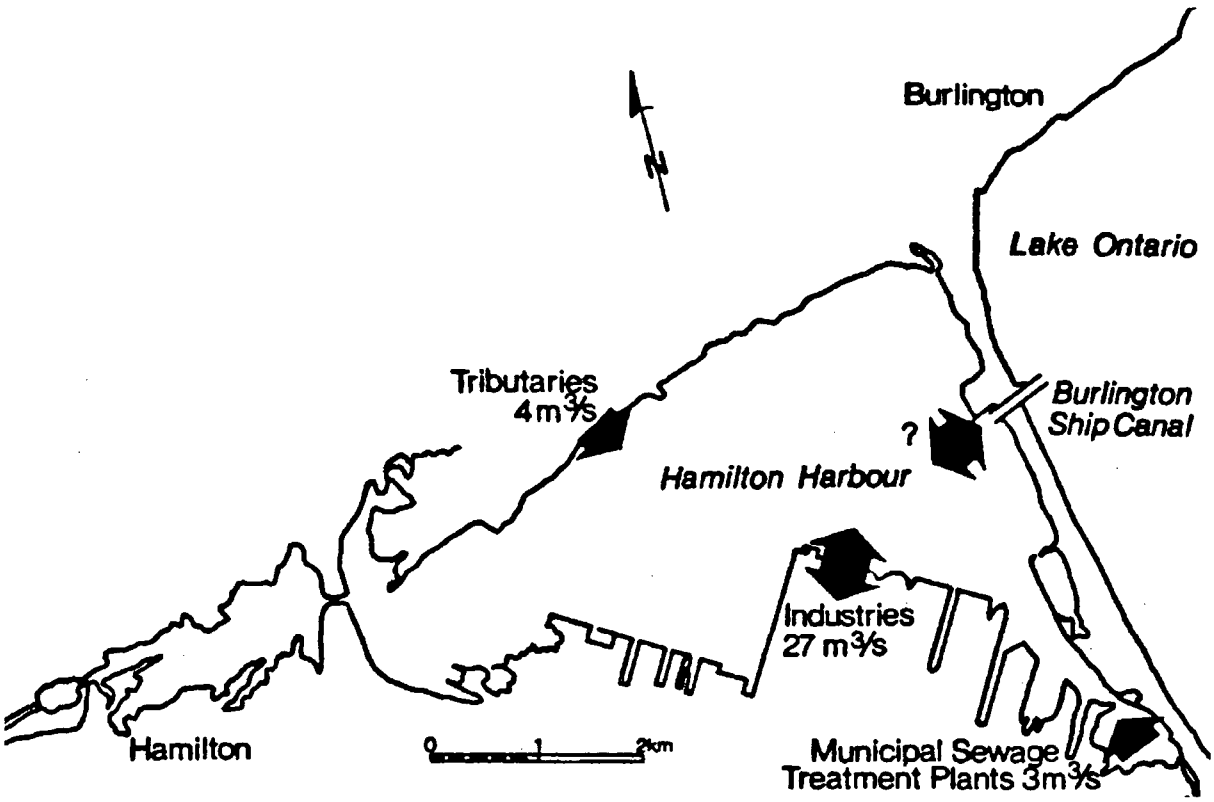

Figure 1-1. Plan view of Hamilton Harbour, Burlington Ship Canal and Lake Ontario (Adapted from Figure 1 of Hamblin & Lawrence, 1990).

(a)

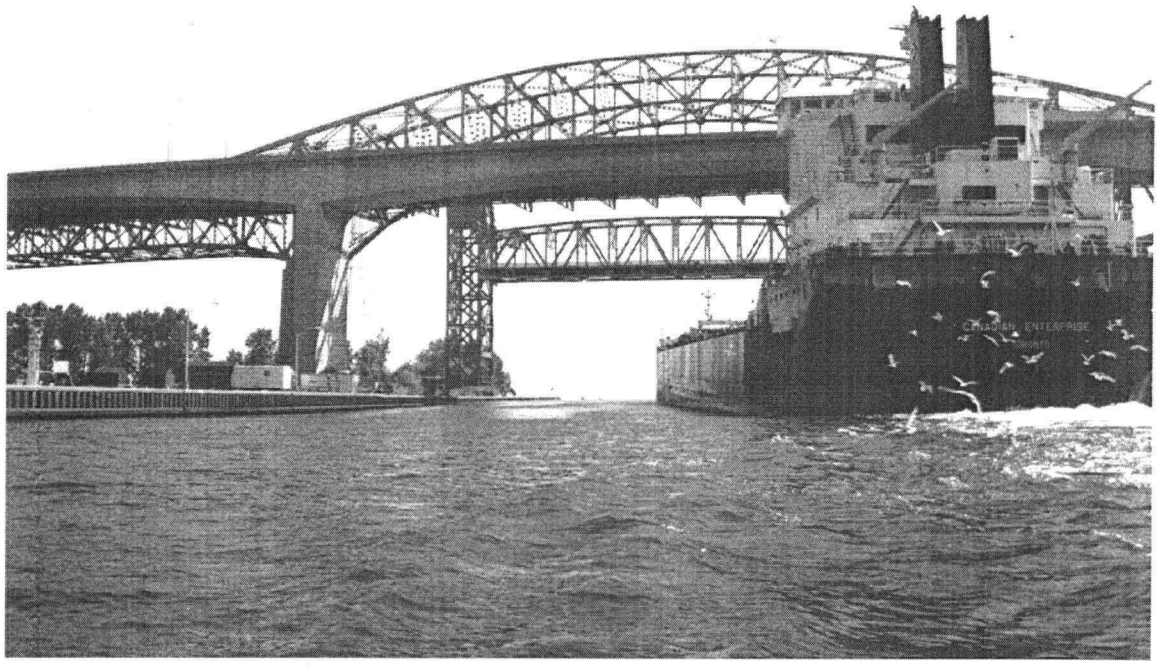

(b)

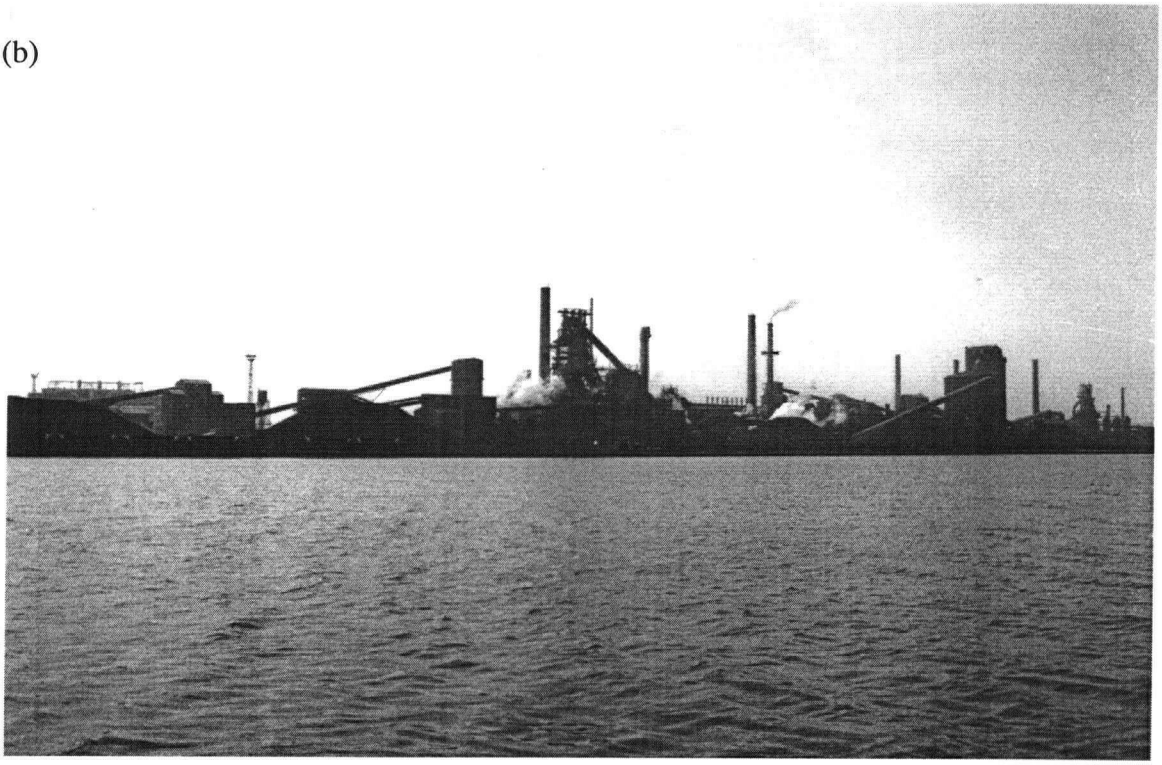

Figure 1-2. (a) Burlington Ship Canal looking towards Lake Ontario, (b) Hamilton Harbour.

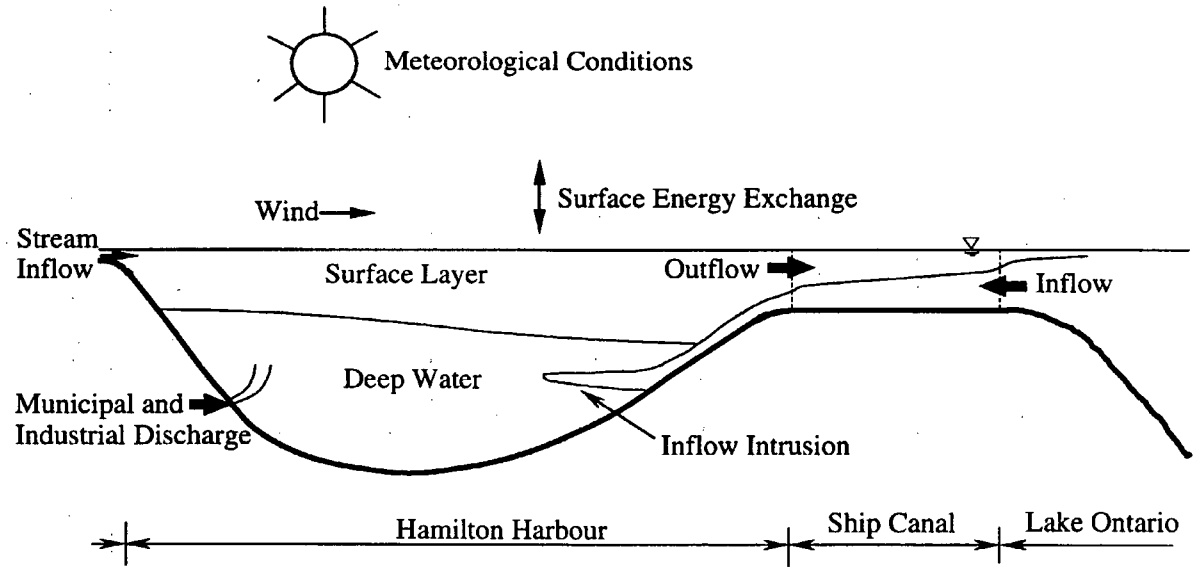

Figure 1-3. Schematic of the two-layer densimetric exchange flow through the Burlington Ship Canal during summer (Redrawn from Figure 2 of Hamblin & Lawrence, 1990).

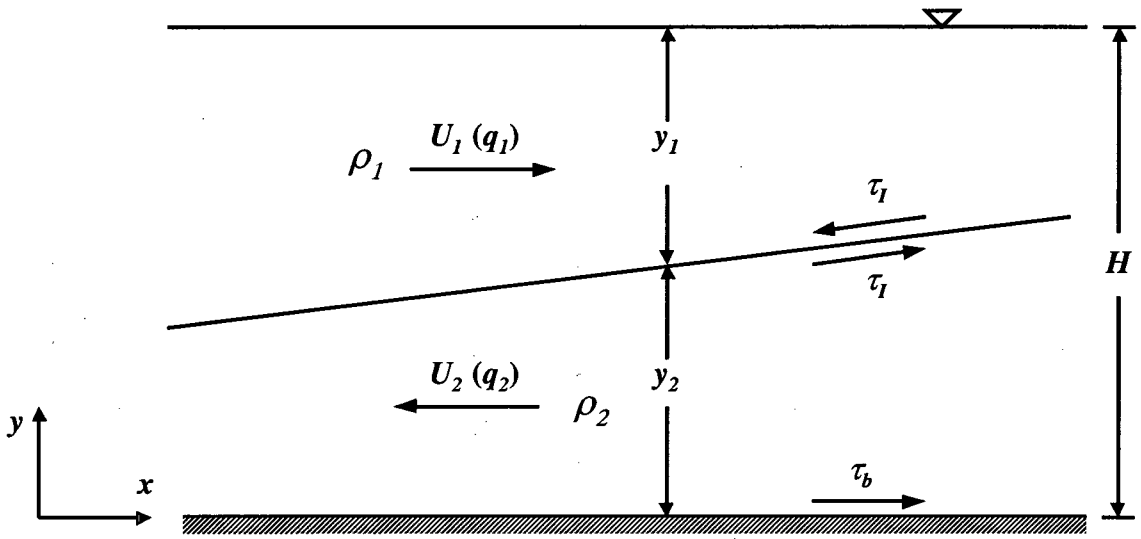

Figure 2-1. Notation sketch for a two-layer exchange flow system.

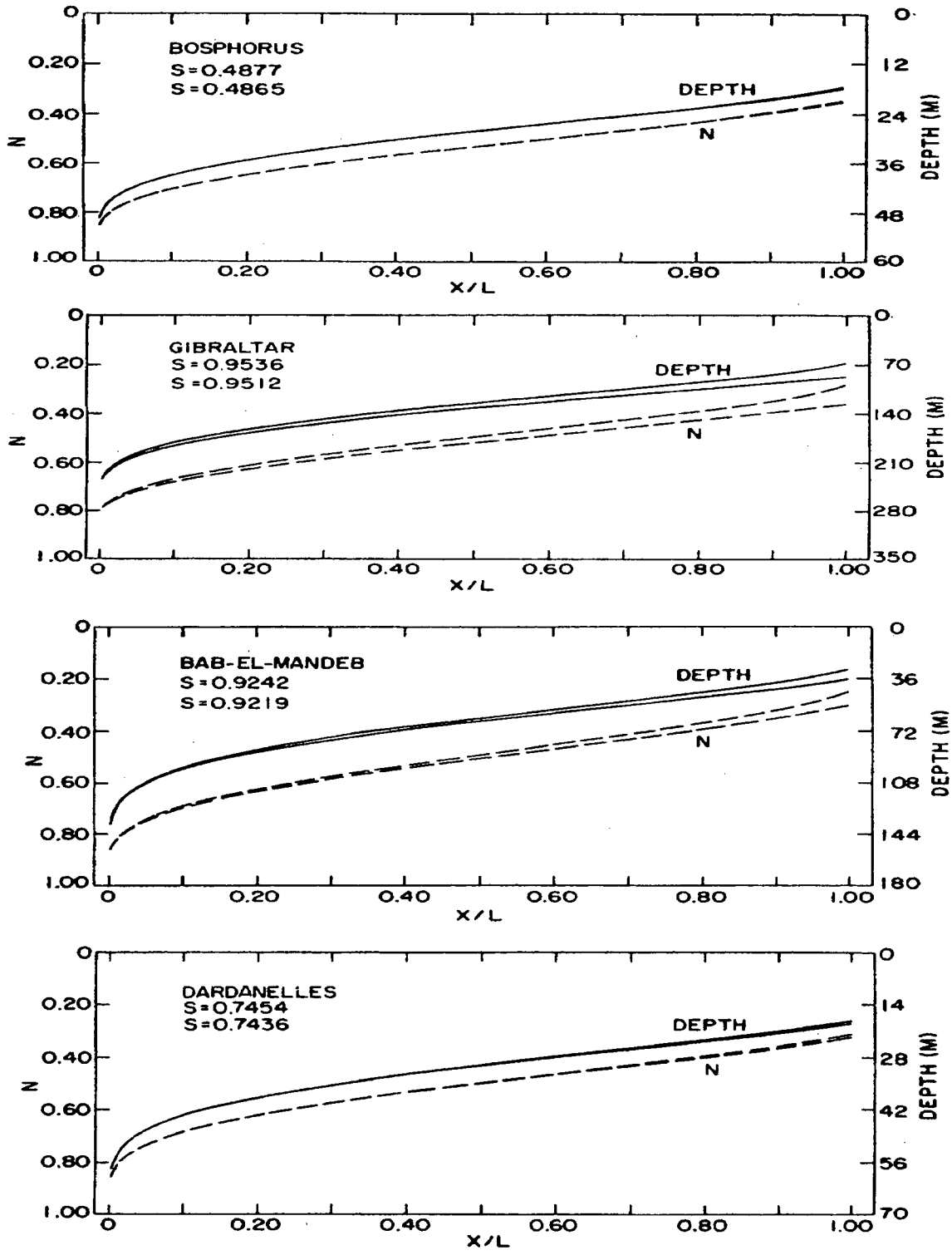

Figure 2-2. Depth of the interface as a function of position along the strait. The upper curves are for the largest S values, where S is the salinity ratio of two exchanging water bodies and N is upper layer area fraction of the total cross section area (Adapted from Figure 2 of Assaf & Hecht, 1974).

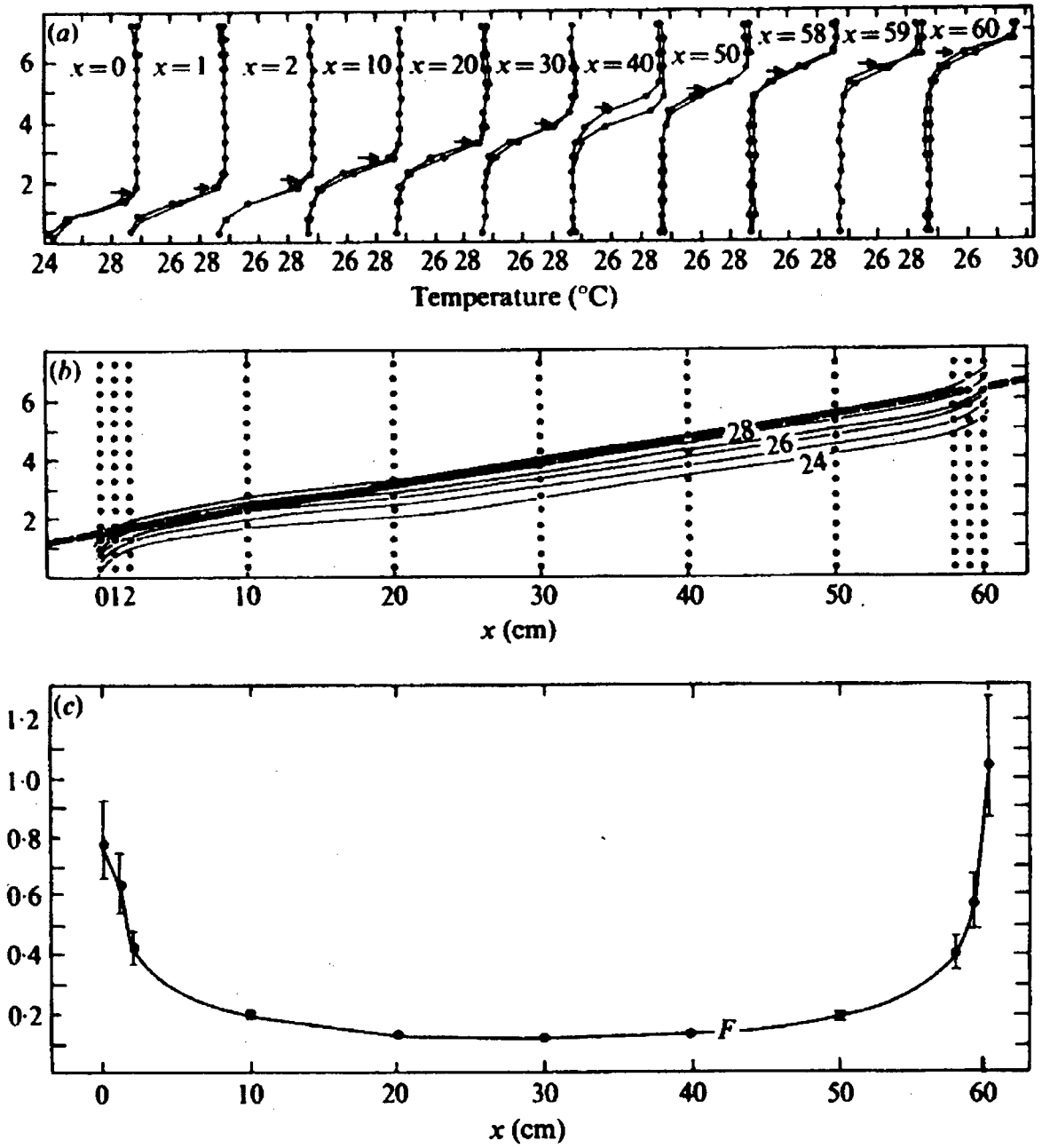

Figure 2-3. Measurements in the long strait experiments of Anati, et al. (1974). (a) Temperature profiles at 11 stations along the length of the strait. Arrows denote the height of zero velocity. (b) A longitudinal temperature section along the strait. The heavy dashed line, with slope $\beta = 0.615$, is the solution of (2-2). (c) The measured composite Froude number at 11 stations along the length of the strait (Adapted from Figure 10 of Anati, et al., 1977).

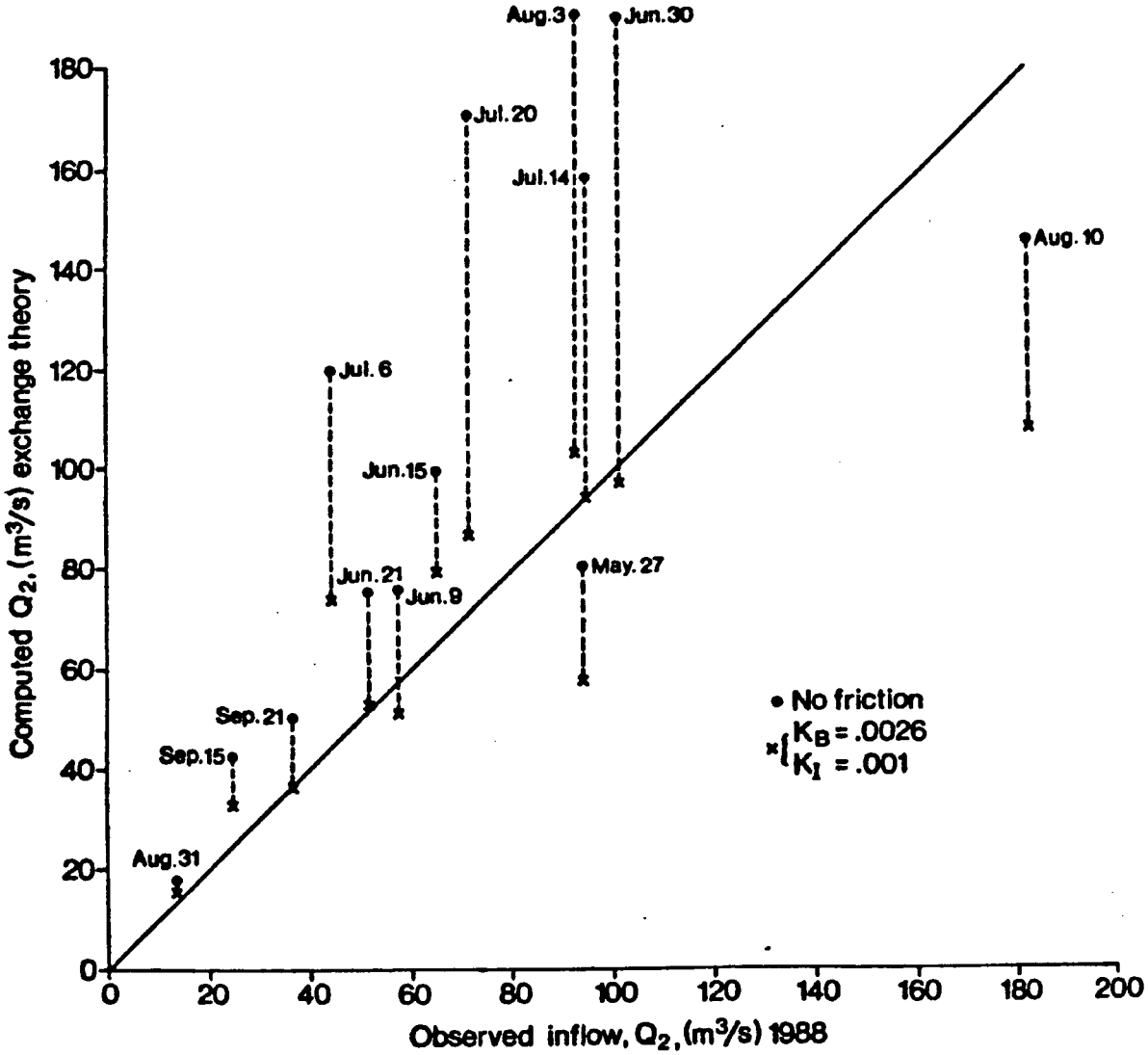

Figure 2-4. Computed Lake Ontario inflow, Q_2 (m^3/s), based on extreme density difference from the data of Spigel (1989), versus observed inflow (Adapted from Figure 3 of Hamblin & Lawrence, 1990).

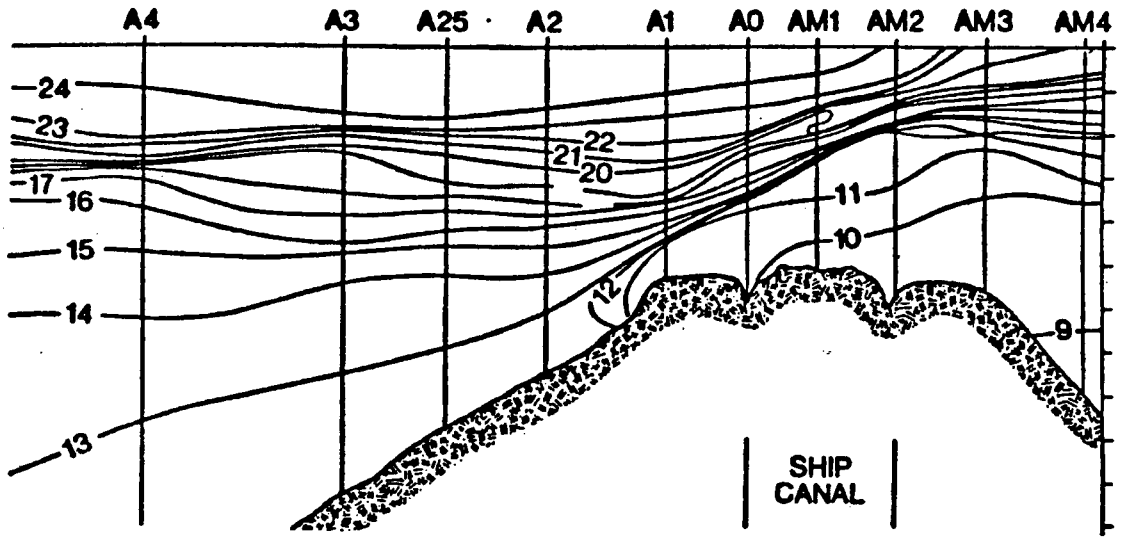

Figure 2-5. Temperature contours for the Hamlilton Harbour on August 3, 1988, indicating overturning event at station *AM*1 (Adapted from Spigel, 1988).

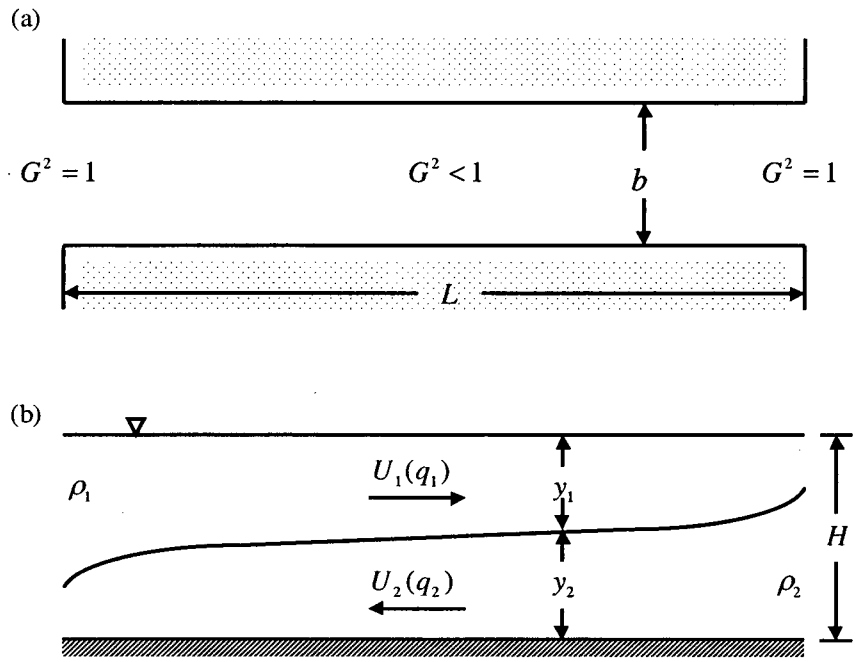

Figure 3-1. Plan (a) and side (b) views of the flow configuration for the maximal two-layer exchange flows. U_i, y_i and ρ_i are the average velocity, depth, and density of each layer respectively. L, H and b are channel length, depth and width respectively. Subscripts $i = 1, 2$ denote upper and lower layers respectively.

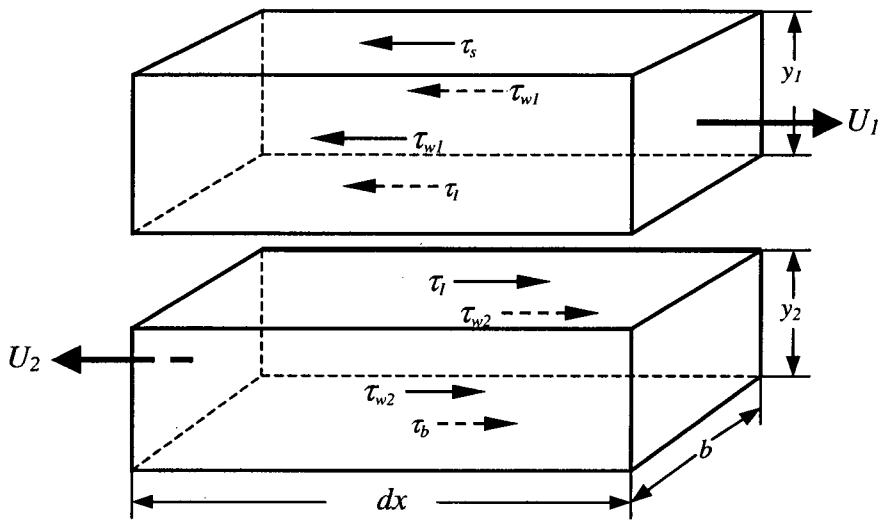

Figure 3-2. Definition sketch of the shear stresses acting on a control volume of a two-layer flow system, where τ_s, τ_w, τ_b and τ_l are surface, wall, bottom, and interfacial shear stresses respectively.

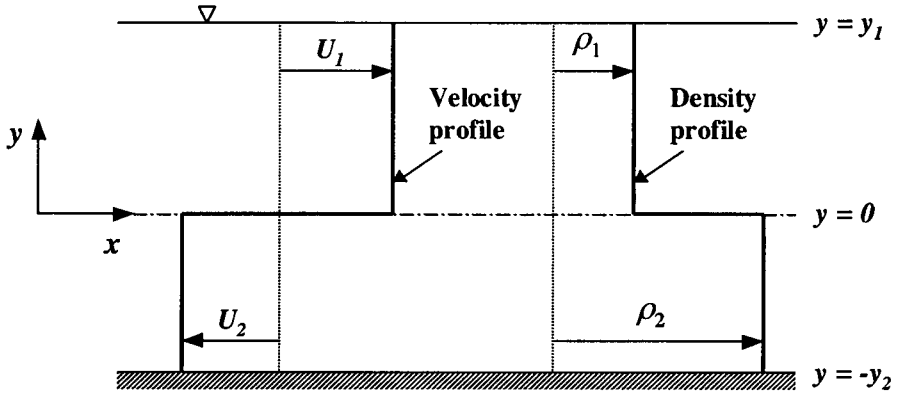

Figure 3-3. Definition diagram for velocity and density structures of a two-layer flow system separated by a vortex sheet at $y = 0$.

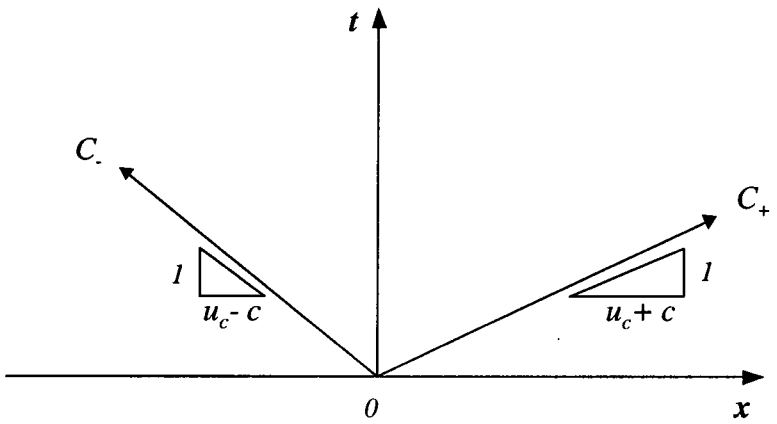

Figure 3-4. Characteristic curves on the $x-t$ plane, where u_c and c are convective velocity and phase speed of two-layer flows respectively, C_+ and C_- are positive and negative characteristics respectively.

(a)

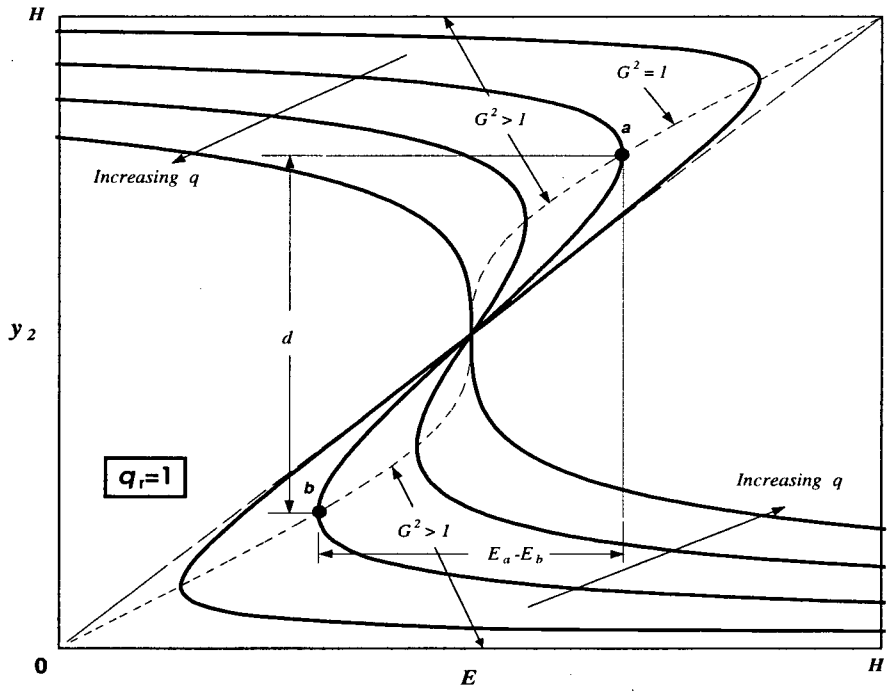

(b)

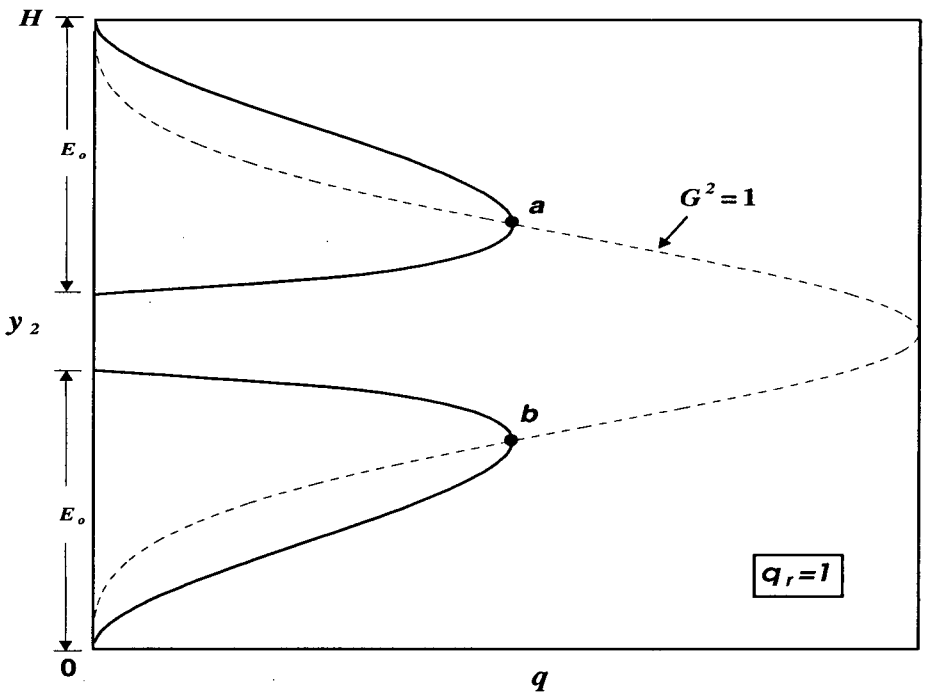

Figure 3-5. (a) $E - y_2$ curves for given exchange flow rate q. (b) $q - y_2$ curves for given internal energy E. Points a and b represent locations at left and right ends of the channel for maximal exchange flows.

(a)

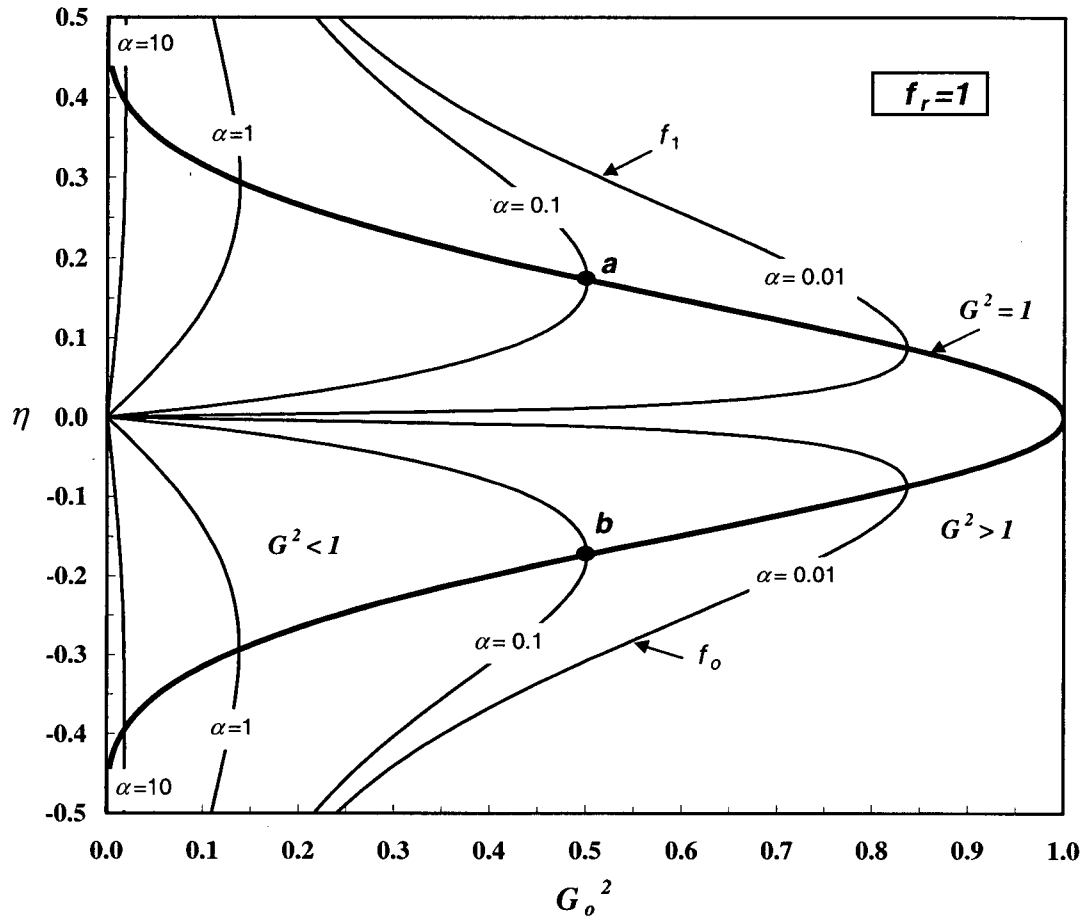
f_r=1
α=10
α=1
α= 0.1
α= 0.01
f_1
f_o
a
b
G^2 = 1
G^2 < 1
G^2 > 1
η
G_o^2

(b)

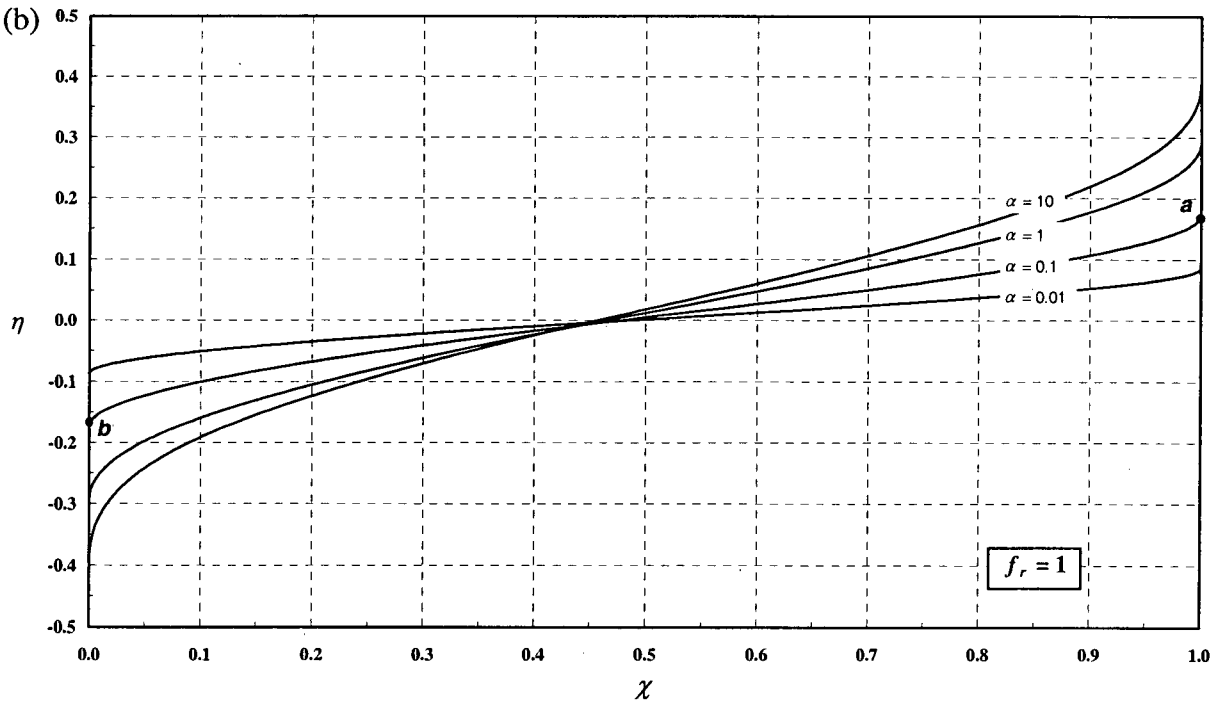
α = 10
α = 1
α = 0.1
α = 0.01
a
b
f_r = 1
η
χ

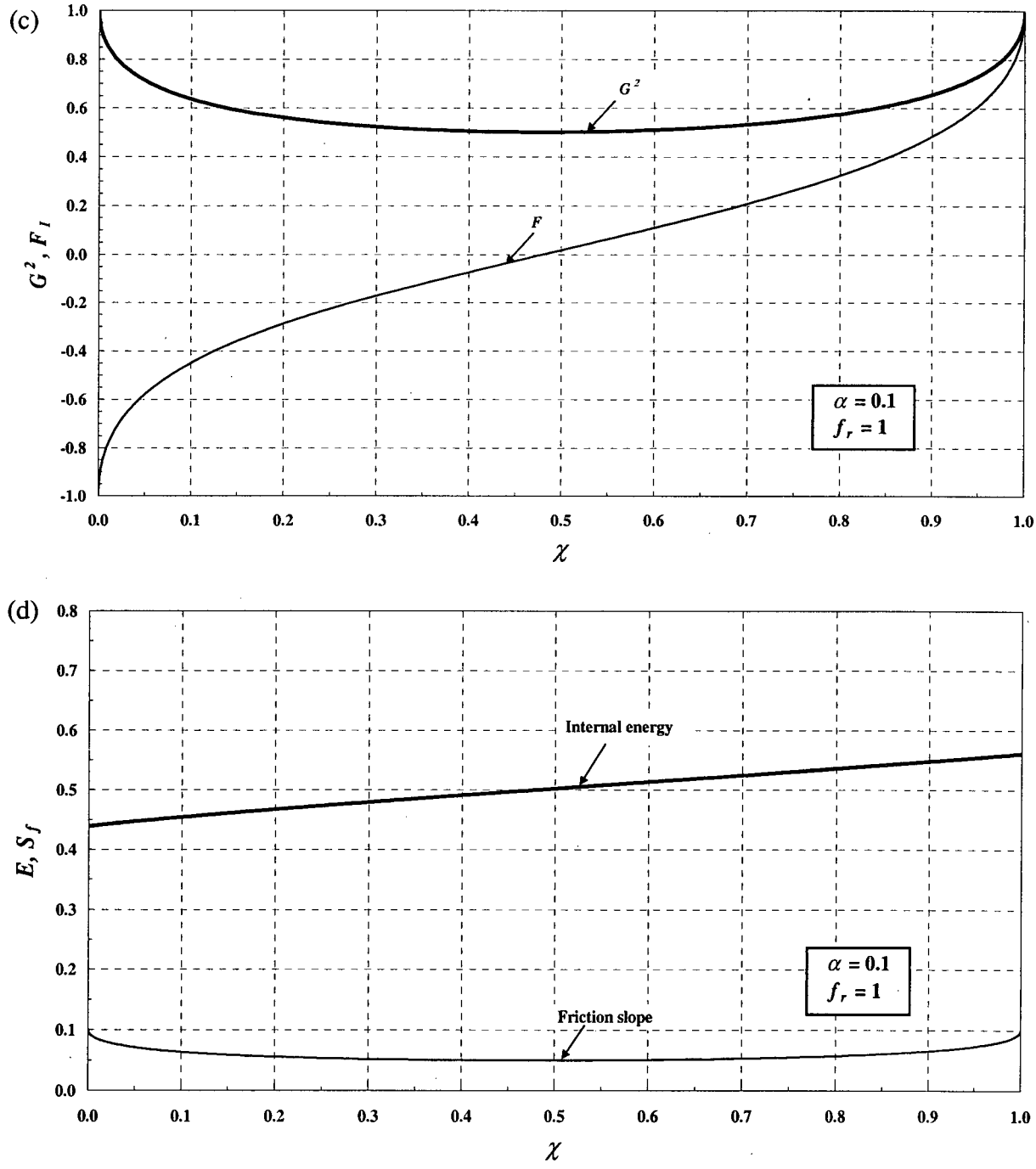

Figure 3-6. Analytical solutions for densimetric two-layer exchange flows through a wide channel. (a) Presentation of solutions on the $G_o^2 - \eta$ plane, where thinner lines are solution curves of varying frictional parameter α ($f_r = 1$), and thicker line represents the critical boundary condition at each end of the channel. (b) Variation of density interface along the channel, where points a and b correspond to locations shown in (a). (c) Variations of the composite Froude number G^2 and the internal Froude number F_I along the channel. (d) Variations of the friction slope S_f and the internal energy E along the channel.

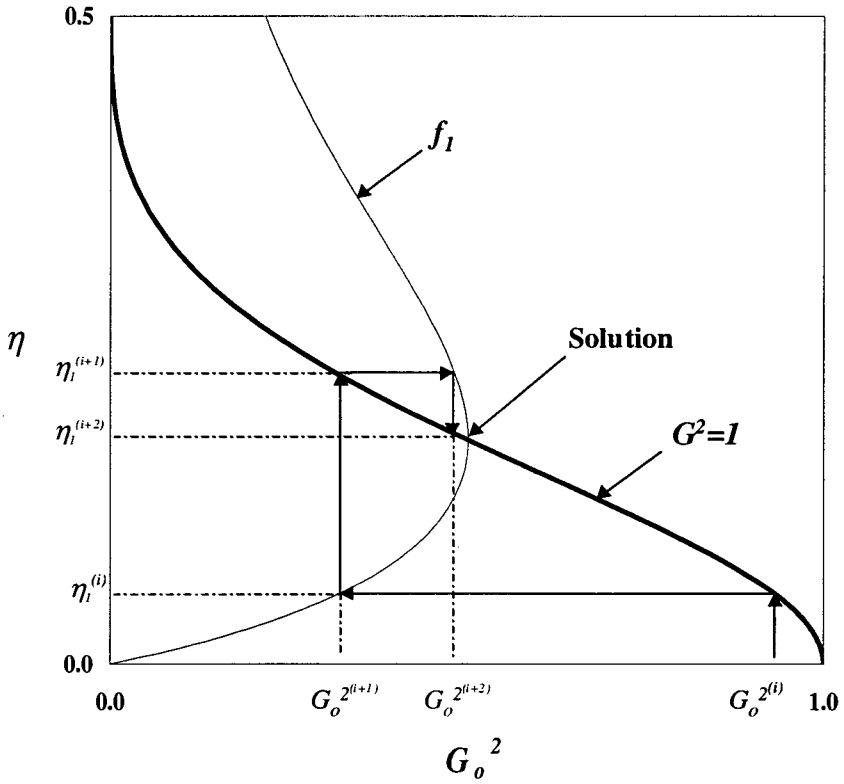

Figure 3-7. Schematic showing the iteration procedure used to solve the maximal two-layer exchange flows as a boundary value problem, where f_1 and $G^2 = 1$ are solution curve and hydraulic control condition at either channel end respectively. $G_o^{2(i)}$ and $\eta_1^{(i)}$ are intermediate iteration values of G_o^2 and η_1 at the i^{th} iteration respectively.

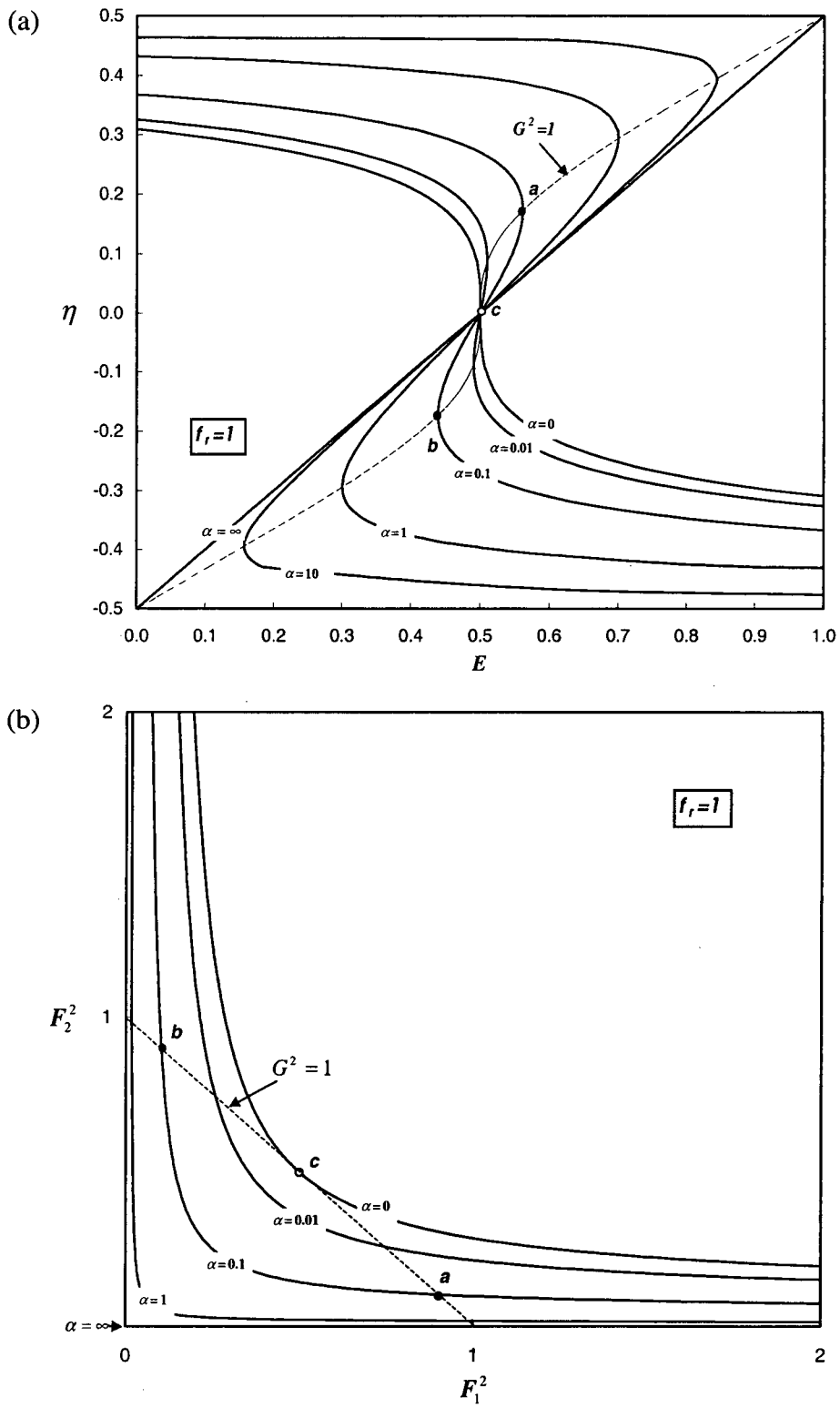

Figure 3-8. Maximal two-layer exchange flow solutions represented on the $E-\eta$ plane (a) and on the Froude-number plane (b). Points a and b correspond to locations shown in Figure 3-6b. Point c represents the solution for $\alpha=0$.

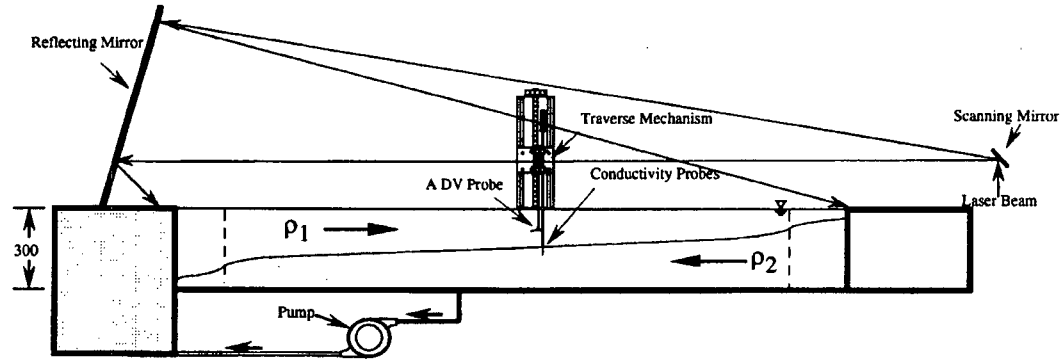

Elevation View

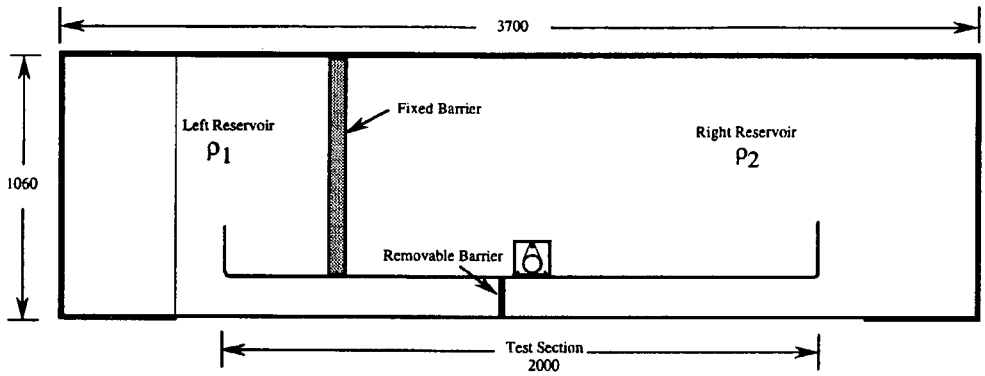

Plan View

Figure 4-1. Overview of laboratory experiment set-up. All dimensions shown are in millimeters.

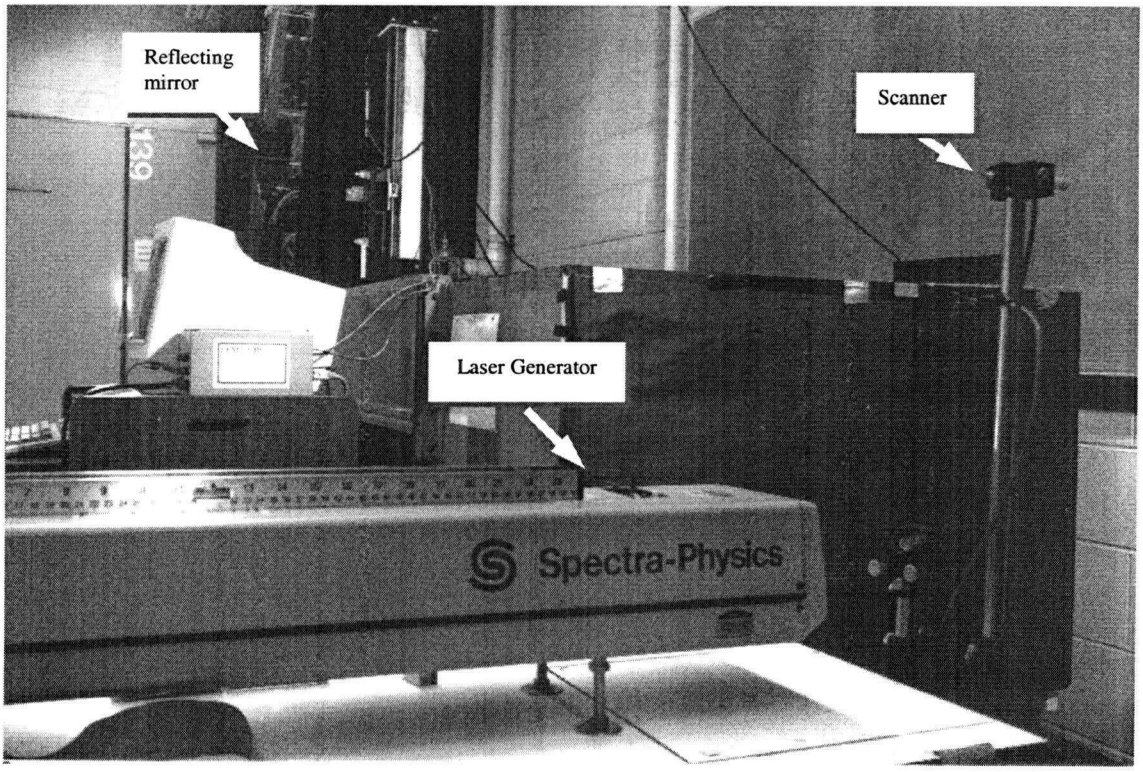

Figure 4-2. Laser optical set-up showing the laser generator as well as scanner and reflecting mirrors.

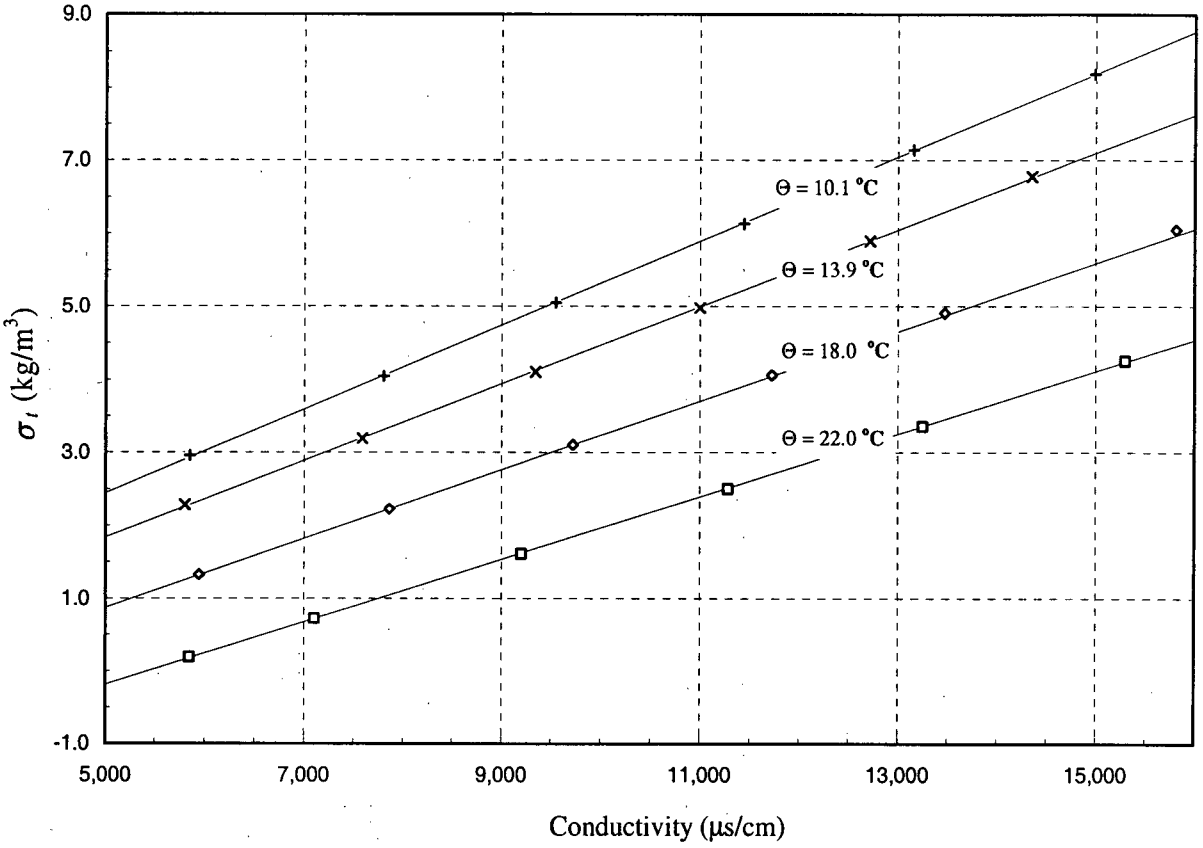

Figure 4-3. The relationship between density as $\sigma_t = \rho - 1000$ and conductivity for NaCl salt solutions used in the experiment at four different sampling temperatures. The symbols are direct calibration points and the solid lines are linear regression curves.

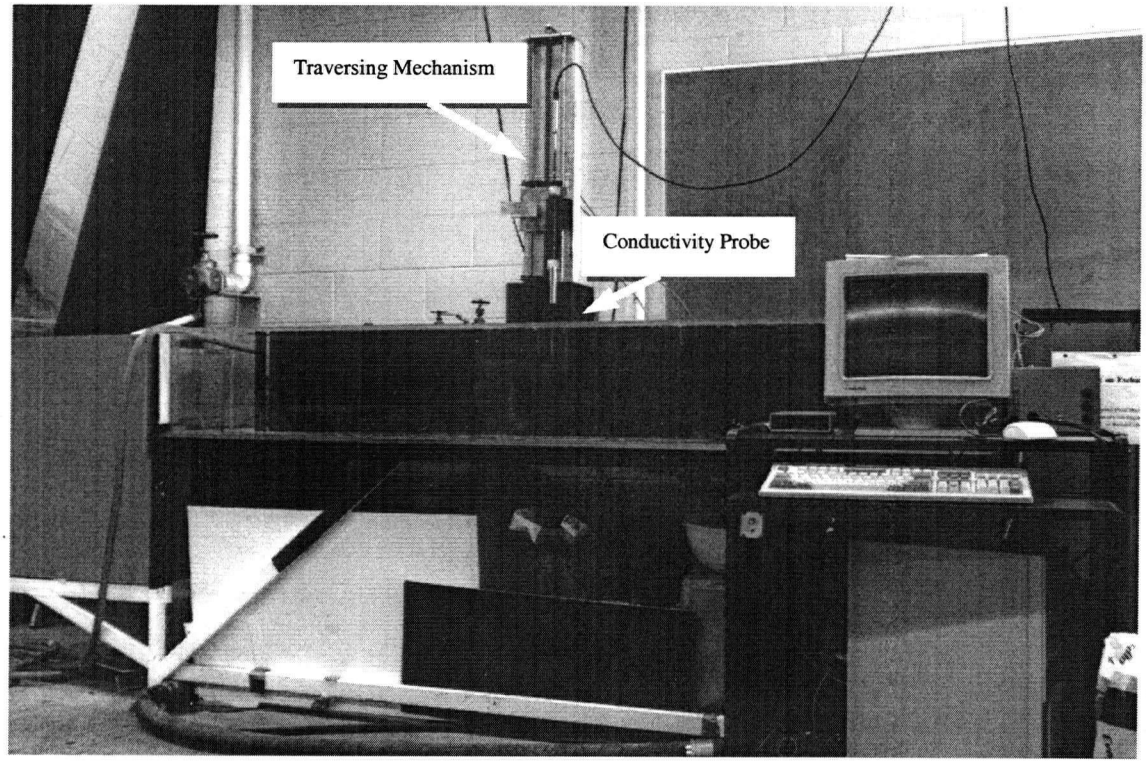

Figure 4-4. Automated traversing mechanism and conductivity probe.

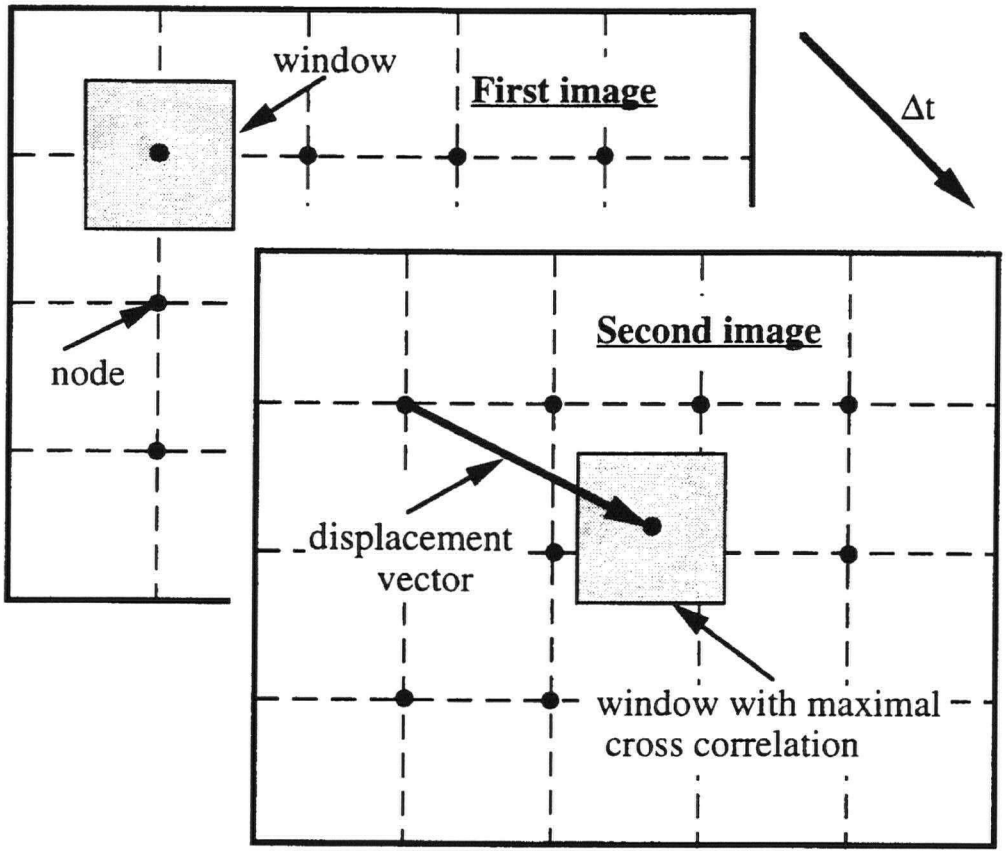

Figure 4-5. Schematic diagram of particle image velocimetry technique. Two images are captured at Δt apart. The velocity is calculated at each node by search a widow with maximum cross correlation (Adopted from Figure 1 of Stevens & Coates, 1994).

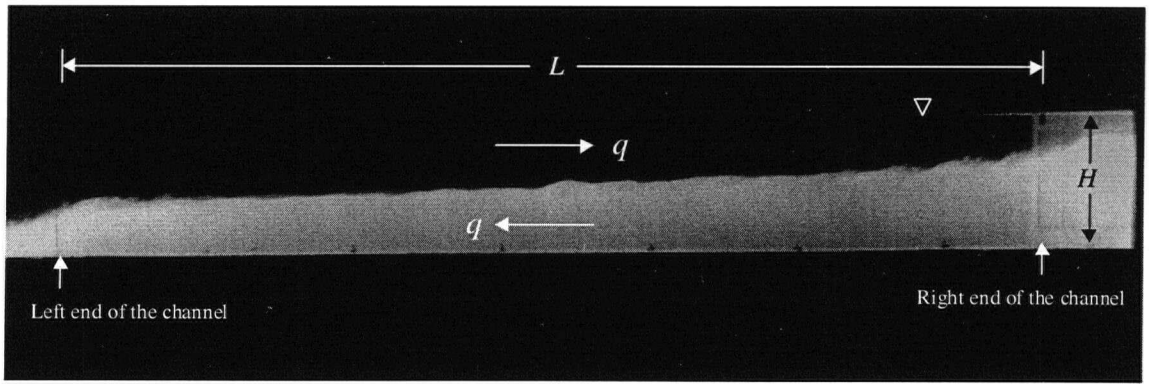

Figure 4-6. Laser induced florescence image showing two-way maximal exchange flow.

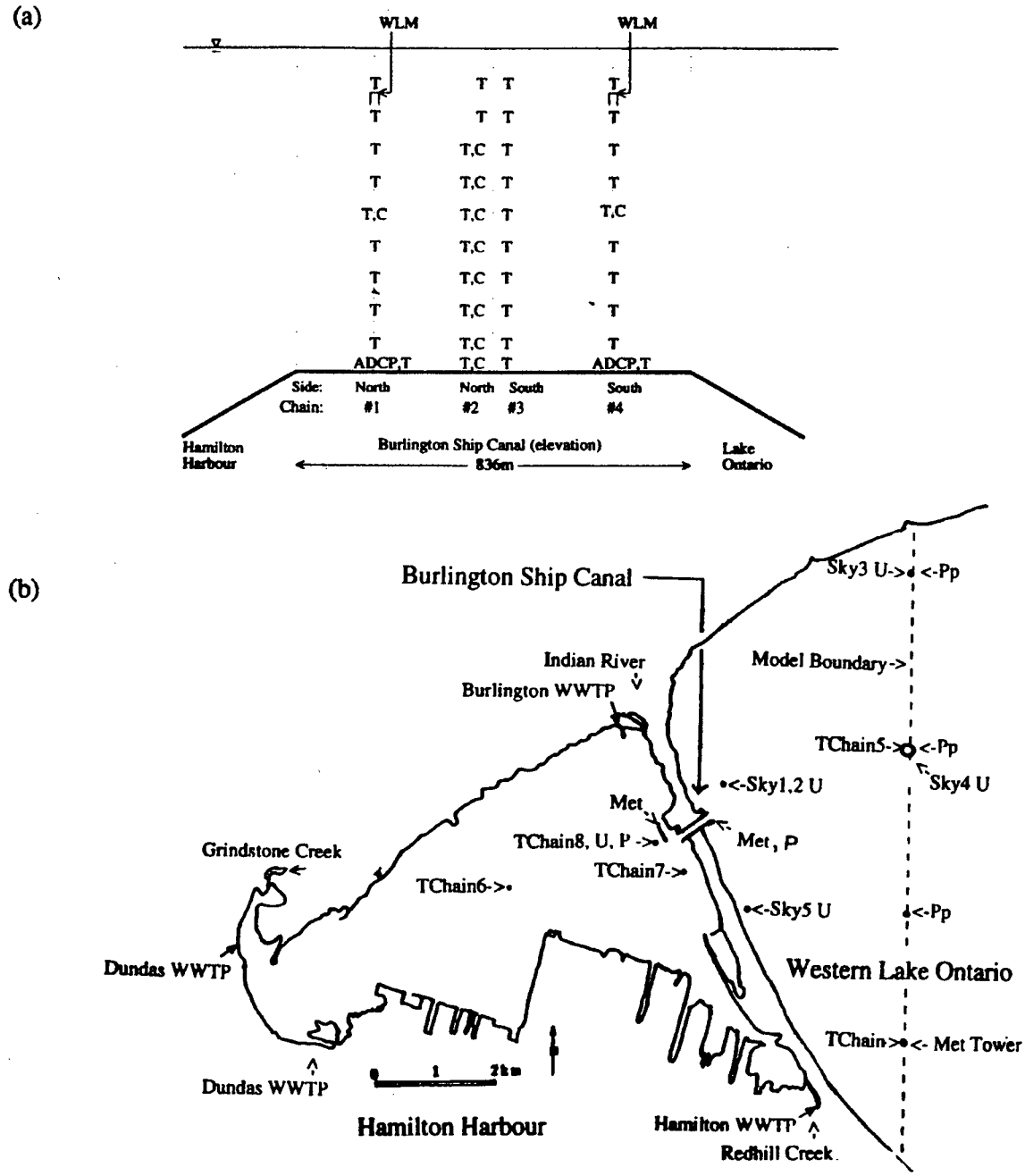

Figure 4-7. Location and set-up of moored instrumentation for summer 1996 field experiment. (a) Side view of the ship canal. (b) Plan view of the Hamilton Harbour (Adopted from Figure 3.1 of Tedford, 1999).

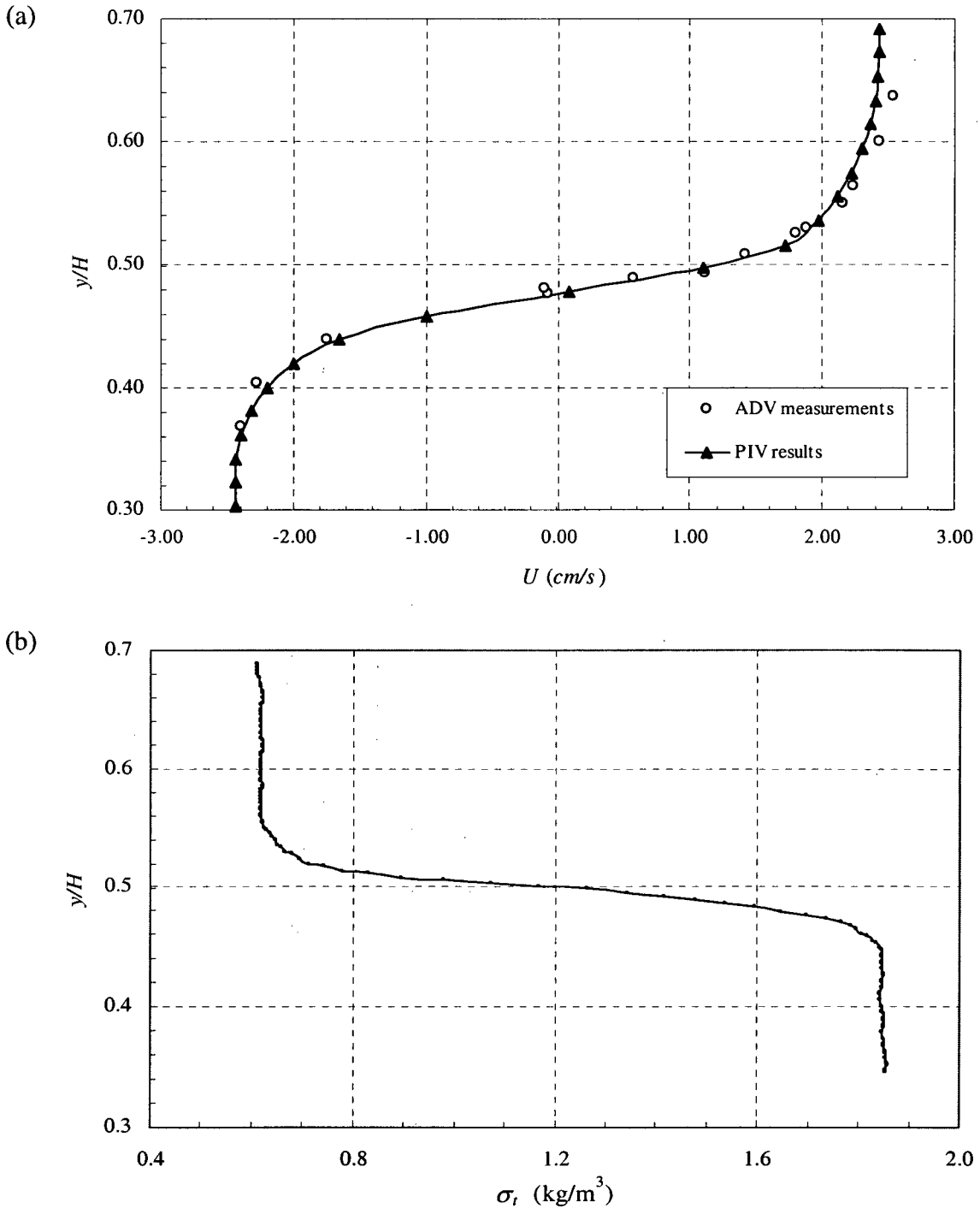

Figure 5-1. Measured velocity and density profiles for E5 at $x = 0.5L$. (a) Velocity profile measured by PIV technique and ADV probe. (b) Density profile measured by a traversing conductivity probe.

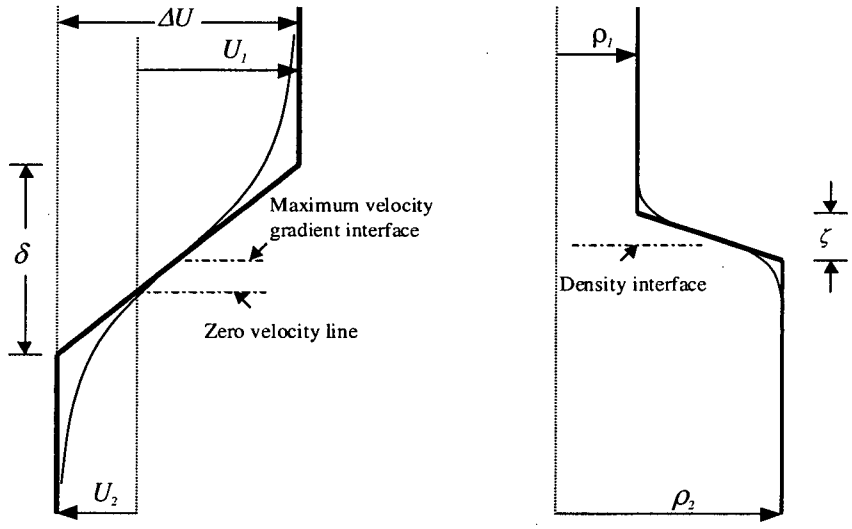

Figure 5-2. Definition diagram for three different interfaces of exchange flows, where δ and ς are the shear layer thickness and the density interface thickness respectively.

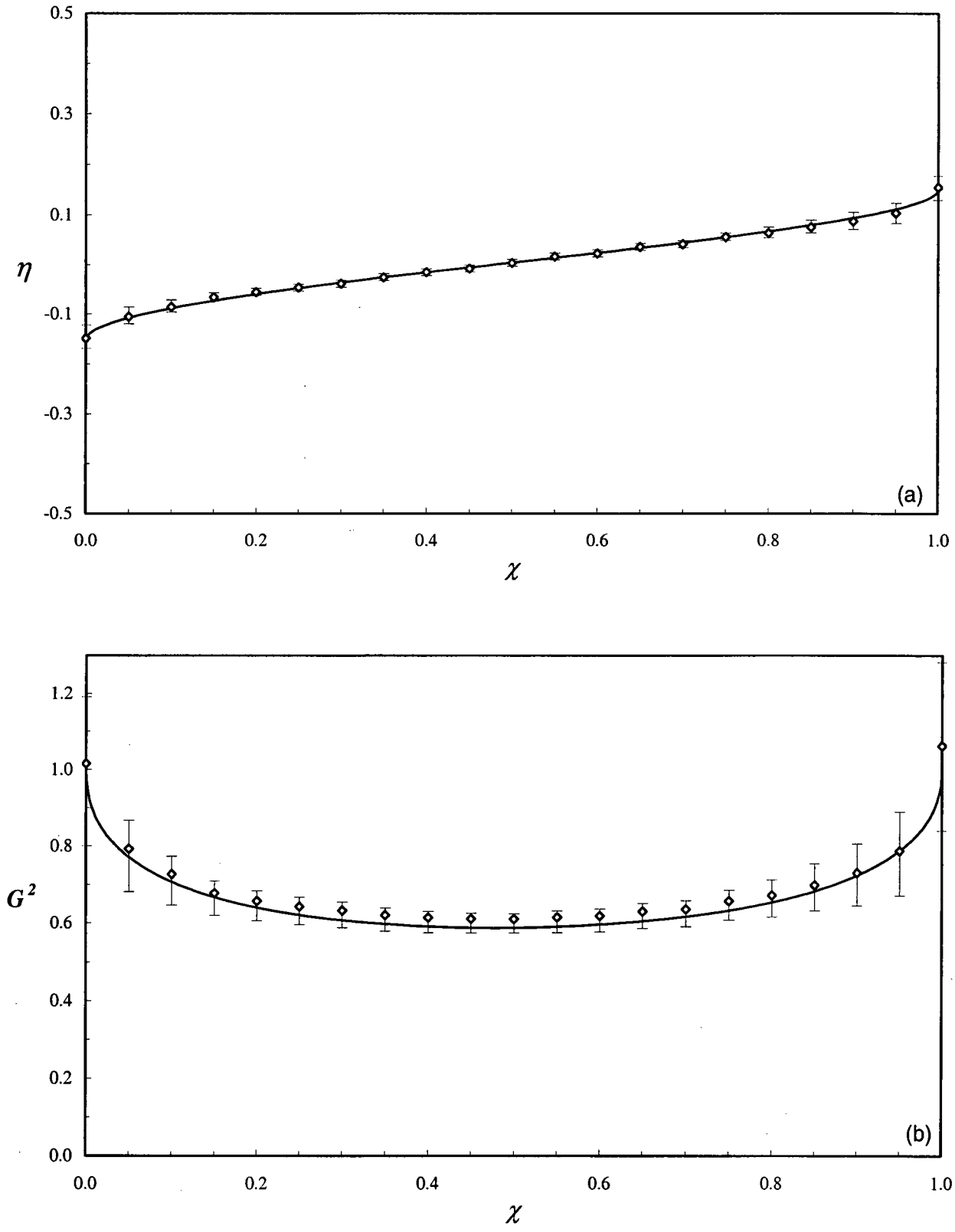

Figure 5-3. See next page for captions.

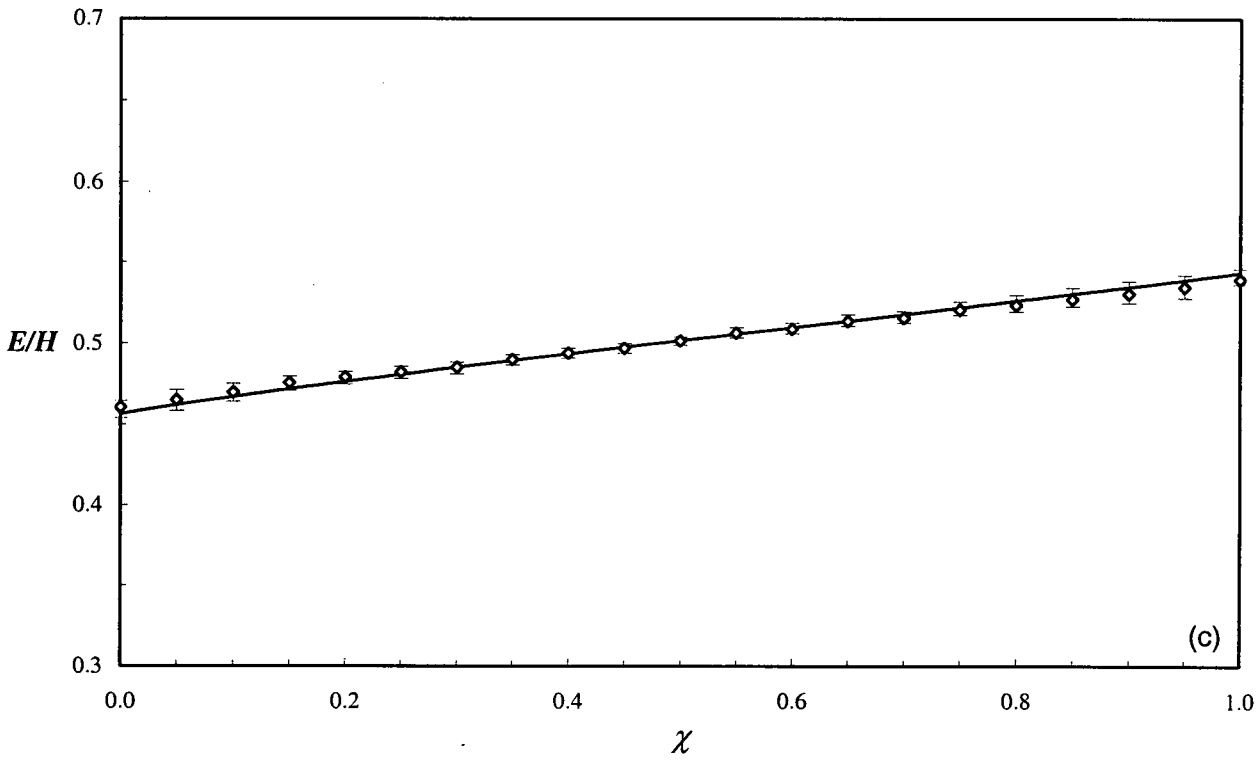

Figure 5-3. Comparison of the theoretical predictions with laboratory experiment E5. (a) Density interface profile along the channel. (b) The variation of composite Froude number, G^2, along the channel. (c) The variation of internal energy, E/H, along the channel. Solid lines are theoretical predictions based on analytical exchange flow solutions. The symbols with error bars represent laboratory measurements.

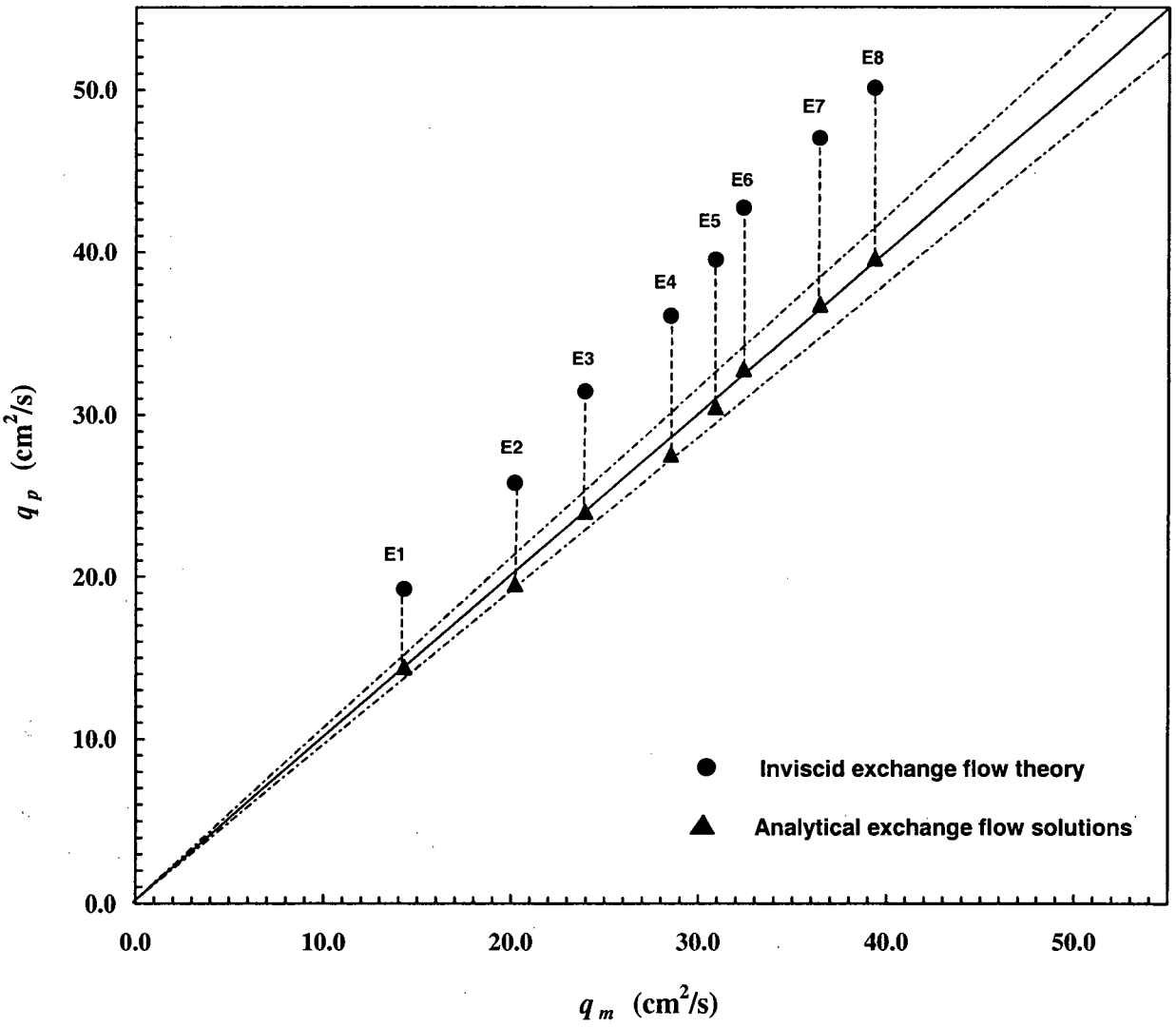

Figure 5-4. Comparisons on exchange flow rates between laboratory measurements (q_m) and theoretical predictions (q_p) for eight experimental runs (E1 – E8). The solid triangles and the circles are the predictions of frictional analytical solution and inviscid exchange flow theory respectively. The two dotted lines represent $\pm 5\%$ error from the perfect match. The bottom friction factor f_b ranges from 0.007 to 0.013, and the interfacial friction factor f_i ranges from 0.0031 to 0.0041.

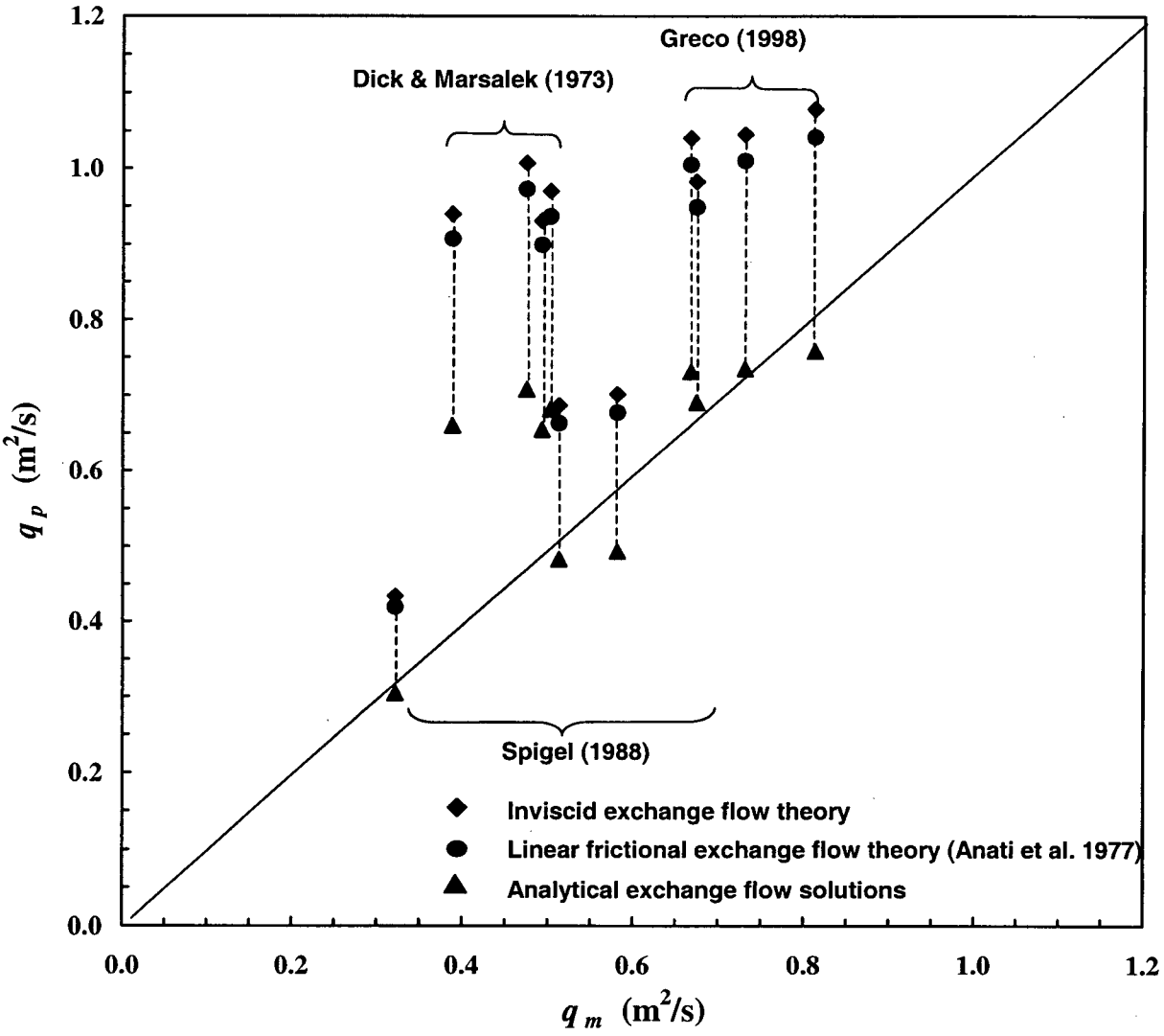

Figure 5-5. Comparisons of field measurements of exchange flow rates through the Burlington Ship Canal (q_m) with theoretical predictions (q_p). The solid triangles, the circles, and diamonds represent predictions based on the analytical exchange flow solution, the linear exchange flow theory and the inviscid exchange flow theory respectively. The bottom friction factor $f_b = 0.0026$ and the interfacial friction factor $f_i = 0.001$.

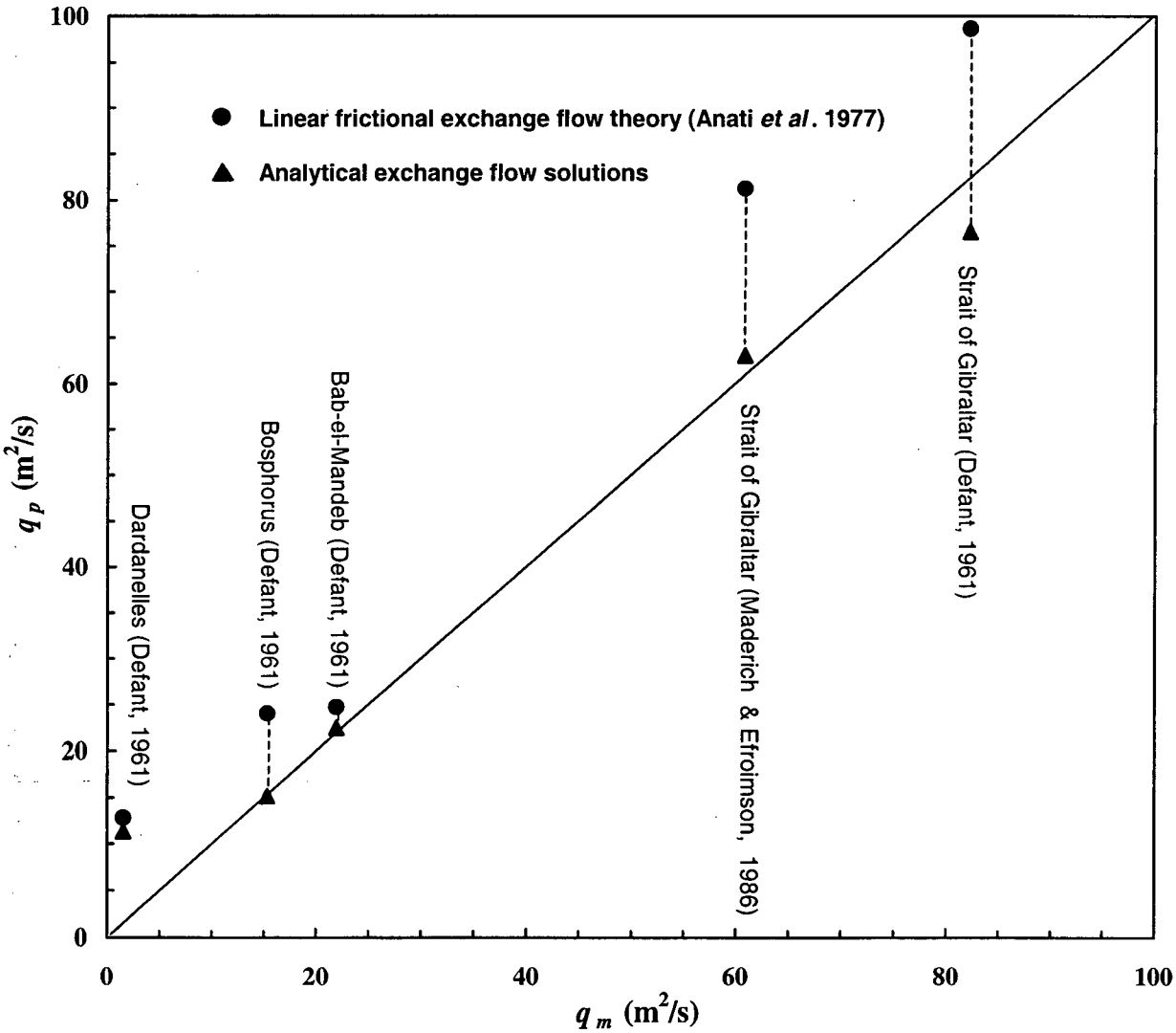

Figure 5-6. Comparison of field measurements of exchange flow rates through several famous sea straits (q_m) with theoretical predictions (q_p). The solid triangles and the circles are predictions of the frictional analytical solution and the linear exchange flow theory respectively. The bottom friction factor $f_b = 0.012$, except for the Bosphorus Strait where $f_b = 0.0046$. The interfacial friction factor $f_i = 0.0024$ for all the straits.

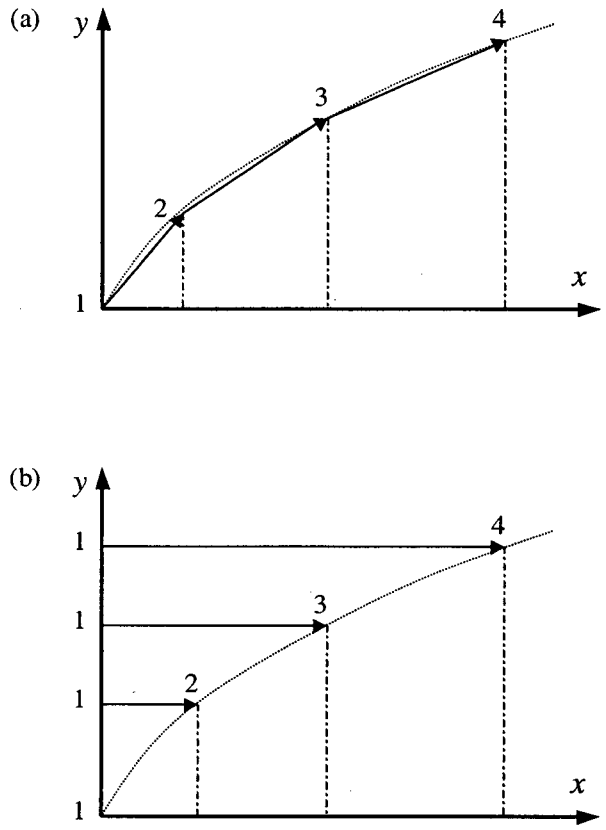

Figure 5-7. Comparison of computational schemes used for calculation of longitudinal density interface profiles. (a) Numerical integration or step method. (b) Direct integration method. Points *1*, *2*, *3*, and *4* represent order of computational procedure.

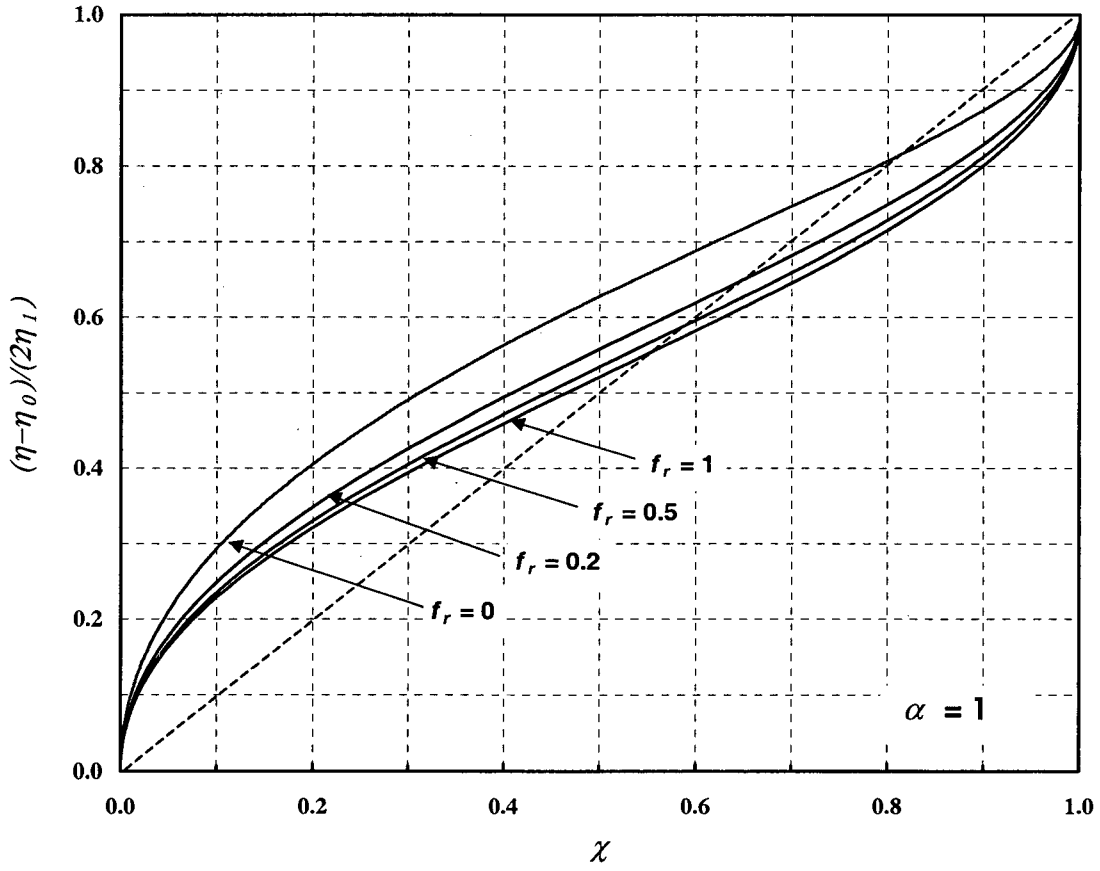

Figure 5-8. Normalized interface shapes for two-layer exchange flows with varying frictional ratio f_r. The frictional parameter α is constant at unity.

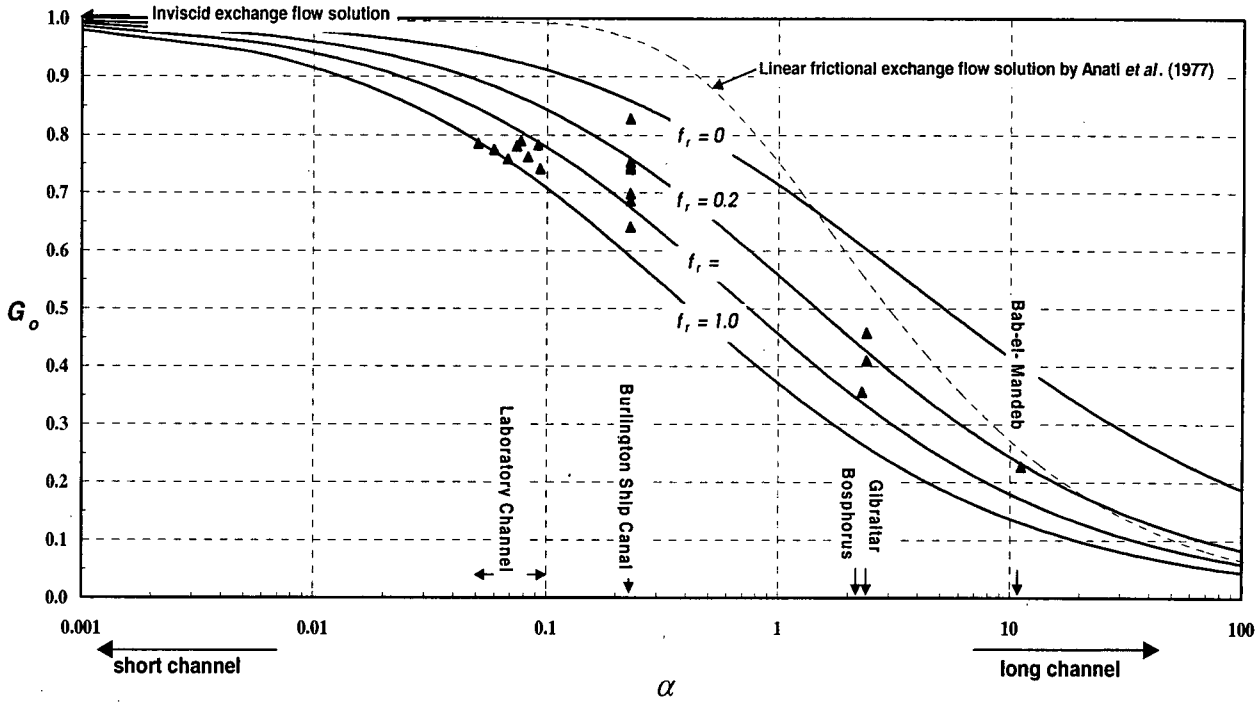

Figure 5-9. Effects of friction on the exchange flow rates. The solid lines represent the analytical frictional exchange flow solutions developed in this study. The doted line represents the linear exchange flow solutions of Anati, *et al.* (1977). The friction ratio of f_r ranges from 0.7 to 1.0 for laboratory experiments and from 0.2 to 0.4 for field data respectively.

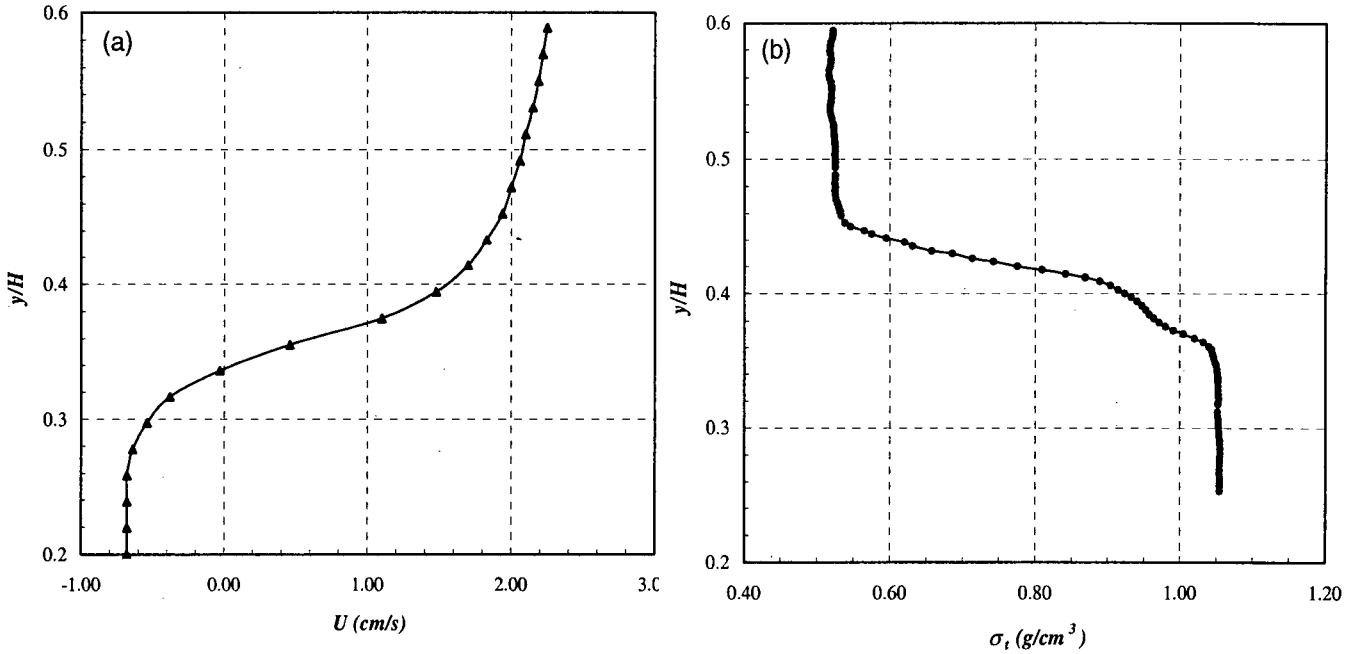

Figure 5-10. The measured velocity and density profiles for E9 at $x = 0.5L$. (a) Velocity profile measured using PIV technique, and (b) density profile measured by a traversing conductivity probe.

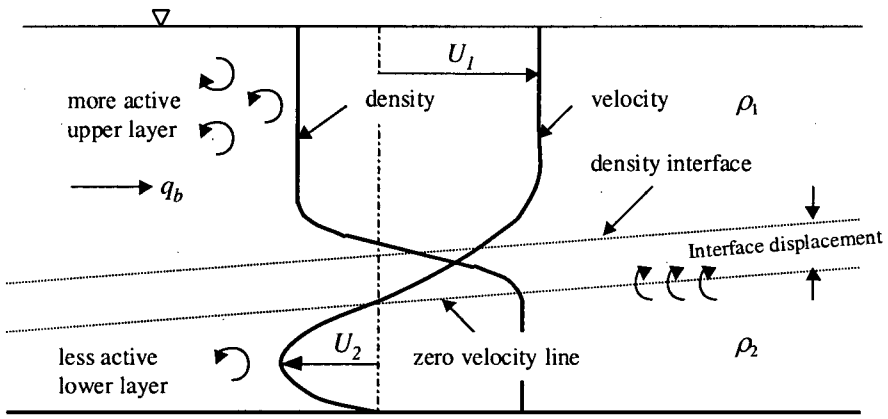

Figure 5-11. Schematics of internal flow structure of a two-layer exchange flow with a barotropic flow component.